POLITECNICO DI TORINO

Master's Degree in Civil Engineering

Curriculum: Structures

Innovative Geomatics Techniques in Structural Monitoring: Application in Large-Scale Experimental Test

Academic Supervisors
Dr.Eng. Vincenzo Di Pietra
Dr.Eng. Pierclaudio Savino

Candidate
S301481 Ziwei Hou

A.Y. 2022/2023

November 2023

Content

List of Figures

List of Tables

Abstract

This study offers a detailed description of the application of innovative geomatics techniques in the structural monitoring of a large-scale experimental test. A full-scale prestressed concrete (PC) box girder specimen is retrieved from an existing 50-year-old viaduct in Turin, Italy and is subjected to cyclic loading in a four-point bending test (FPBT). During the loading phases, an aerial photogrammetric survey has been conducted to produce static multitemporal data of the beam, exploiting commercial professional Unmanned Aerial Vehicle (UAV) instrumented with high-resolution optical sensor. After a set of strategic photogrammetric procedures in Metashape, numerous metrical and radiometrical accurate results are obtained and post-processed in software Microsoft Excel, QGIS and MATLAB. The measurements extracted are under deeper discussion and further analysis, evaluated and validated against the measurements provided by traditional linear variable displacement transducers (LVDTs). The findings demonstrate the feasibility of the proposed techniques by showing good agreement with the transducer-based measurements and numerical analysis in the assessment of deflection and strains. The promising results support that in the future, UAV photogrammetry, equipped with other geomatics techniques, could become a standard monitoring method for the large-scale experimental test considering its rapid deployment, affordable cost and superior accuracy when compared with other conventional methods.

Keywords: geomatics techniques; structural monitoring; large-scale experimental test; aerial photogrammetric survey; UAV; photogrammetric procedures

1. Introduction

Many civil structures and infrastructures are designed and constructed to act as the backbone of a community, delivering necessary services and facilitating economic activities[1]. They are subject to numerous challenges and issues in both normal use and extreme conditions[2-3], being faced up with diverse types of structural damages. Besides the structural health monitoring (SHM) which reports the health status of structures with integrated sensors and advanced algorithms[4-6], various and rigorous tests are also required to describe structural behavior, which are critical for the maintenance and decision making in management. Full-scale load testing is preferred to develop more realistic and reliable estimation of global structural behavior, compared with the small-scale tests and computer simulation. For example, full-scale destructive tests are conducted on various structures to perform a reliable life-cycle structural assessment and evaluation of residual service life of existing bridges[7].

However, given the significant consumption of resources—human, financial, and material—destructive testing on such large components is challenging. For instance, relatively few studies have been carried out with full-scale model tests on the flexural behavior of PC box girders from decommissioned bridges around the world[8-15]. Under these circumstances, an accurate and thorough structural monitoring approach of such tests is therefore of great necessity since the data gathered during tests are of extreme interest to understand the global behavior.

Monitoring techniques can be used to measure and analyze the structural reaction to the applied loads. Based on how they interact with the structure being assessed, different monitoring methods fall into two basic categories: contact and non-contact methods. To quantify the dynamic response, such as stresses and strains, traditional contact sensing techniques apply sensors or transducers to specified positions on the structure and a wide range of devices are embraced in such sensors[16-20]. Up to now, it has been found that sensors excel in supplying precise and specific parameter measurements, making them suitable for critical monitoring tasks. But it should also be highlighted that they pose some economic and practical challenges. As an illustration, the contact-based sensors involve time and labor-intensive installation process and seek substantial maintenance to achieve long-term monitoring[21]. Additionally, the sparse and discontinuous nature of the data collected by these sensors could restrict both the accuracy and the efficacy of structural health monitoring, especially for large-scale structures.

With the development and advancement of robotic technology, there has been a paradigm shift of sensing techniques that outperform the traditional contact sensors. The representative one is UAV photogrammetry, which captures data without physical contact, providing visual information about structural behavior. This revolutionary technology enables cost-effective and rapid data collection with high spatial and temporal resolution, making it invaluable for applications ranging from precise mapping and 3D modeling to environmental monitoring and disaster response[22]. By eliminating the need for human presence in hazardous or inaccessible locations, UAV photogrammetry enhances safety while delivering real-time data and adjustable solutions tailored to specific project requirements[23]. Its flexibility, precision, and reduced environmental impact have contributed to its adoption as an essential tool in industries such as construction and conservation. In this situation, photogrammetry with the aid of UAVs, also known as drones, has been introduced and applied extensively in civil engineering, particularly in terms of both spatial resolution and flexibility in temporally repeating the survey.

To have a more comprehensive understanding of the advantages and disadvantages of different monitoring systems, the comparison between the contact and the non-contact methods will be conducted with reference to some physical parameters, for instance displacement and deformation. For this reason, a set of photogrammetric products will be introduced and applied as input for post-processing analysis of specific physical phenomenon, in particular:

A. Numerical analysis in Excel.
B. Morphology multi-temporal variation with DEM of Difference (DoD) in QGIS.
C. Digital image correlation (DIC) on orthomosaic in MATLAB.

Previous research related to these topics is detailed and summarized as follows.

1.1 Related research

The development of UAV photogrammetry is a progressive journey, under significant influence of several factors, including drone technology, imaging tool, processing capability and so on. This study has recalled the whole development of UAV photogrammetry and related research on it, especially its application in civil engineering in different working scenarios and under various task requirements.

Gordan, Meisam, et al covered the recent advances, applications, and future perspective of Unmanned Aerial Systems (UAS). Equipped with an array of sensors and cameras making them ideal for checking the health condition of the structures[24].

Darragh, et al proposed a low-cost approach based on a commercial action camera. It was changed to make it easier to employ telescopic lenses and combine with the development of robust displacement identification algorithms based on pattern matching. The efficiency and preciseness of this system were then proven after its performance in a series of controlled laboratory tests and the field experiment was assessed[25]. In the research of Ekinci, Abdullah and associates, the strategic measures taken to monitor the deflection of a basic pile retaining wall during basement excavation and construction were provided. The monitoring is done using a commercial UAV and the viability of the proposed method can be proven by the monitoring results that show good agreement with the traditional measurement and analysis[26]. Additionally, more meaningful outcomes could be found if successive 3D reconstructions of the objects of interest is generated and compared. In the study of Zhao, Sizeng, et al, model reconstruction is presented for dam emergency monitoring and inspection via UAV images. The structure from motion (SfM) method is used to generate a 3D dam model with scene geometry, which is employed to calculate the cloud point coordinates and camera pose. Satisfactory result in a significant improvement in the dam monitoring and inspection efficiency is proved[27]. B. Suhovilov and colleagues developed a photogrammetric method to figure out the spatial coordinates of control points of large-size constructions to build a 3D geometrical model of the structure and estimate the parameters of interest[28].

Once georeferenced correctly and properly, the derived 3D photogrammetric models can be utilized to produce digital elevation model (DEM), to investigate volume changes and profile variation via the computation of DEM of Differences (DoDs). In the survey of Blasone, G., et al, three areas vulnerable to debris-flow dynamics were studied using multi-temporal terrestrial laser scanning (TLS) surveys and DoDs with a 0.2 m spatial resolution. This allowed the measurement of elevation uncertainty as a spatially variable. The analysis of DEM and uncertainty indexes correlation help to refine methods for spatializing elevation errors and improving the reliability of the models[29]. According to the research of Milan, D. J., a novel approach that allows assessment of spatially distributed error across a DEM was applied, evaluated on a sequence of field surveys of the gravel-bed River Nent, Cumbria, UK. This study demonstrated that estimation of morphological change can be misleading in the absence of an error filter[30]. Taddia, Y. presented the results obtained through a long-term monitoring of a complex dune system with the use of UAVs. The final products of this approach were thus represented by DEMs of the sandy coastal section.

In addition, DoDs were also computed for the purpose of monitoring over time and detecting variations[31]. Furthermore, Digital image correlation (DIC) technology has already been applied to multi-temporal acquisitions[32-34] and orthomosaics[35-36] to obtain deformation maps. With the aim to conduct a remote structural evaluation of a rail tie, Kalaitzakis, Michail, et al. used an autonomous drone system. This work showed how precise DIC is at assessing 2D and 3D shape and deformation fields in structures[37]. Using multi-temporal orthomosaics at ultra-high resolution, Puniach, E. recommended a method for automatically determining the field of horizontal displacements generated by underground mining [38].

1.2 Research background and significance

A dearth of research focused on the application of UAV photogrammetry and other innovative geomatics techniques in the large-scale experimental test monitoring. Extracting accurate geometrical information from photogrammetric products and comparing them with traditional transducer-based monitoring techniques within a single research project is a cutting-edge research, which allows to evaluate the suitability of these different methods in various structural monitoring scenarios and offer suggestions on selecting the most appropriate technique based on specific monitoring requirements.

In the present situation, this comparative study of results obtained by various monitoring methods is elaborated in this thesis.

1.3 Structure of the thesis

This study is organized as follows: In section 2, a brief introduction of the experimental project will be reviewed. A brief introduction to the viaduct and the experimental project BRIDGE|50 will be introduced, and the corresponding transducer-based measurement part in the large-scale destructive test will be detailed. The data used as reference is taken from publications by Savino Pierclaudio, et al, being reported here for a more comprehensive view of the thesis.

Later on, the methodology of this study will be delivered in a systematic manner in section 3, starting from the principal mechanism of photogrammetry, the introduction of adopted instruments and the explanation of photogrammetric processing (shown in Figure 1), to the processing and post-processing of data and images. Thus, in section 4 the specific case study could be conducted with the aid of professional theoretical tools. Then in section 5, comparison and discussion of the monitoring results are detailed, compared, and evaluated against the proposed monitoring data from transducer-based assessment.

Finally, the conclusion of this study would be drawn in section 6.

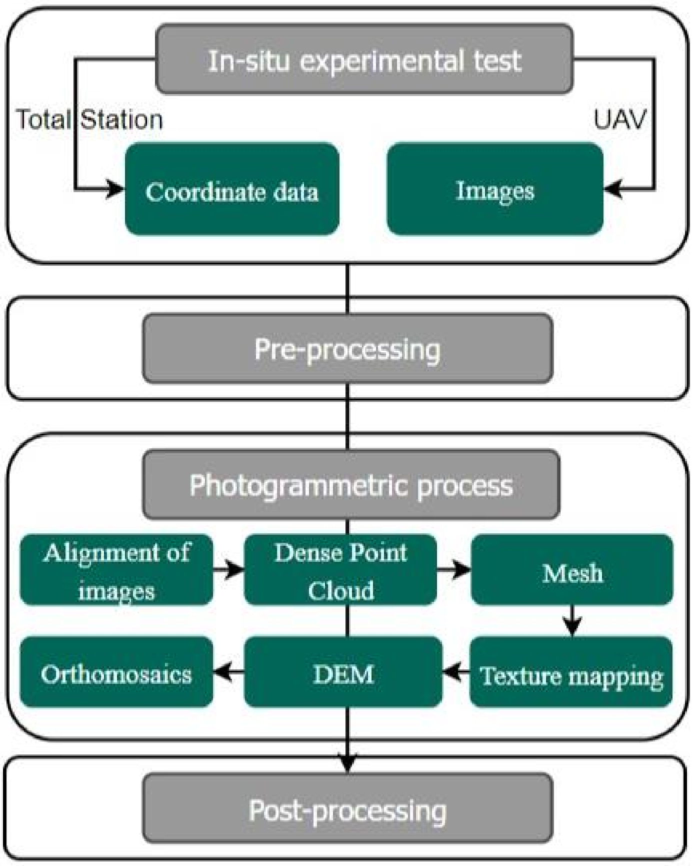

Figure 1 General photogrammetric processing.

2. Full-scale four-point bending test

This section reports the full-scale four-point bending test (FPBT) on a prestressed (PC) box girder, which is retrieved from the Corso Grosseto Viaduct in Turin (Italy) in 2018. This test is part of a research project on bridge beams named BRIDGE|50, taking place on 02/01/2023. In this section, the experimental test and the corresponding transducer-based monitoring work in this test performed by Savino Pierclaudio, et al will be introduced.

2.1 Description of Corso Grosseto Viaduct

Built in Turin (Italy) in 1970, the Corso Grosseto viaduct was a multilevel road interchange developed along two main lines, the Corso Grosseto West-Corso Grosseto East route and the Corso Potenza-Corso Grosseto East route, of a total length around 1.4 km (Figure 2)

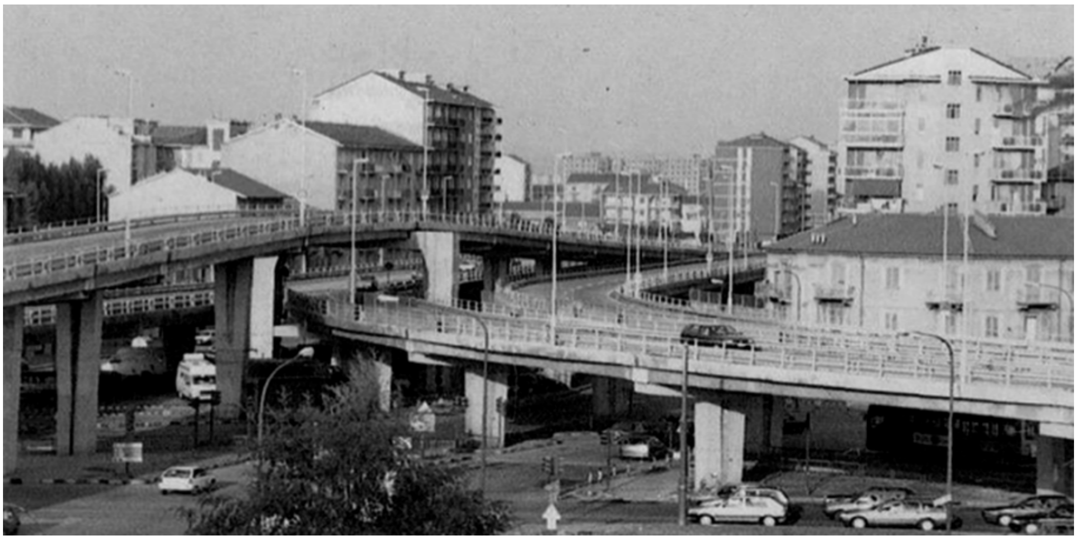

Figure 2 Historical view of Corso Grosseto Viaduct.

Each route was linked by two structurally separate decks, one for each carriage. The deck of every span was made up of 10 precast PC I-beams in the middle and 2 U beams at the edges, which were all joined by a cast-in-situ slab, with the length averaging from 16.0m to 24.0m. In July 2018, the complete closure to vehicular transit was settled to start the deconstruction process following new urban redevelopment and different mobility needs[39].

2.2 BRIDGE|50 Research Project

The BRIDGE|50 project, a collaboration between the Politecnico di Torino, Politecnico di Milano and other authorities, is one of the major research projects on bridge beams now being conducted in Europe and around the world.

The demolition of the Corso Grosseto viaduct (Figure 3) allowed for the installation of 29 prestressed reinforced concrete beams (25 with I-section and 4 with caisson) and 2 piers.

The test field, where the structures and contrast frame are located, is over 5000 m^2 and locates in the neighborhood of Torino Mirafiori[40].

Figure 3 The deconstruction of bridge: cutting.

The proposed experimental activities include a preliminary diagnostic phase, substantial load tests employing the frame from the SISCON center[40], as well as partial damage generated such as cracking, partial plastic deformations, fire, repairs, and following field and laboratory tests and analysis. The data gathered can be used to form a new knowledge base for road network management bodies and assess the safety and residual life of existing structures. The findings will help to develop a modern bridge life cycle design as well as the management, maintenance, and safety of existing infrastructure assets.

2.3 Details of the tested girder

According to the original design documentation[41], the edge beams are at the length of 19.5m and in the cross-section of box shape (U-beam with slab), consisting of 2 I-girders coupled together in terms of resisting section and reinforcement. As shown in Figure 4, it was pretensioned with a total reinforcement area of 184 cm^2, employing 34 strands along the bottom flange distributed over three rows and 6 strands on the top flange distributed over two rows.

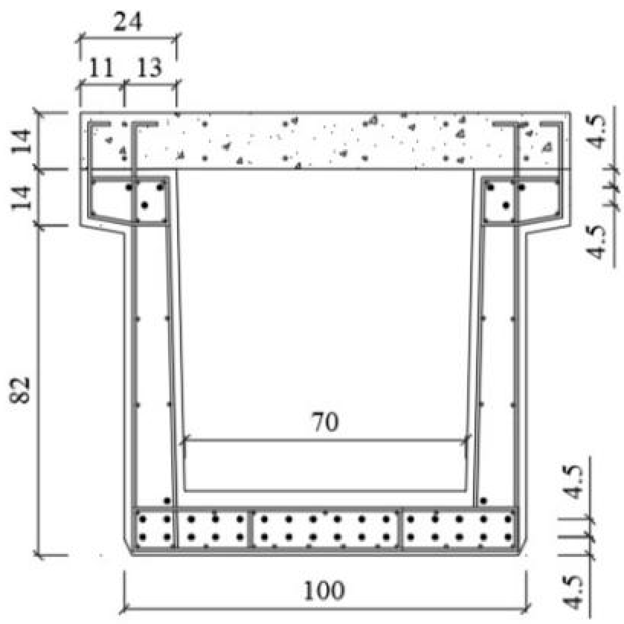

Figure 4 Cross-section of the PC box girder (in cm).

Stirrups measuring 8 mm in diameter and 250 mm apart made up the shear reinforcement. The precast beam and the cast-in-place top deck slab were also connected by stirrups. Based on the initial design data, the material properties were selected in accordance with the allowable stress design, assuming an acting bending moment of 824 kNm on the girders that were under the greatest stress since they were carrying live loads.

2.4 Experimental test

For the purpose of testing the PC box girder with variable load configurations, a proper reaction steel frame was used (SISCON), shown in Figure 5. This tested box girder was simply supported and loaded under a FPBT configuration adopting shear spans of 650 cm. The loading system consisted of two couple of hydraulic jacks which transfer the load to the specimen through transverse steel beams.

Figure 5 Four-point-bending-test configuration.

The loading process was carried out in 3 loading cycles. In the first and second stages, the load was increased until the opening of cracks, followed by the complete unloading of the girder. In the third loading phase, the specimen was loaded up to failure. The load tests were performed with a fixed loading rate by controlling the force and were stopped when the concrete in the compression zone crushed.

The overview of the loading cycles is shown as follows in Table 1. The external force shown in this table is from only one hydraulic jack, which means the loading force will be the sum F_1 and F_2.

To facilitate the recording of the experimental data, a special timeline with 12:00 noon on 02/01/2023 as the starting point of recording was used.

Experimental Stages	External forces (F1=F2) [KN]	Time	Time point [s]
Original	0.00	12:00	0
Instrumentation	0.50	13:35	1500
First loading	130.00	15:00	6500
First unloading	8.50	15:08	7000
Second loading	180.00	15:34	8500
Second unloading	0.20	15:49	10000
Third loading	250.00	18:02	17960
Third unloading	0.00	18:08	18300

Table 1 Overview of the experimental stages.

During the loading scenes, in correspondence with the static sections of the force application, different combined topographic and photogrammetric surveys have been conducted by the geomatics researchers of DIATI department at the same time.

2.5 Transducer-based measurement

Linear variable displacement transducers (LVDTs) are widely used in applications where accurate and repeatable linear displacement measurements are critical, such as structural monitoring and control. They operate by interacting a moving magnetic core with a set of coils, causing changes in induced voltages, and producing a differential voltage output that accurately represents linear displacement.

A suitable measurement plan has been created to measure a number of parameters involving displacements, stresses, loads, and other parameters with the aim to fully understand the structural reaction of this large-scale element.

2.5.1 Instrumentation of transducers

In this section, only the sensors and equipment used to measure the parameters reported in this work and detailed below are summarized. Arrangement of the monitoring system is shown in Figure 6.

The shear span and the bending span, two major zones, have been taken into consideration when designing the arrangement of monitoring system in accordance with the load test configuration. LVDTs with a 707 mm measurement base were mounted on aluminum frames with a 45° orientation along the shear span. These sensors were named by the code “SHxxA/B”, where “xx” denotes the progressive number, “A” denotes the frames with a negative slope, while “B” denotes the frames with a positive slope. In this configuration, 4 shearing LVDTs can be noted on each side of the box girder. As for the bending zone, the LVDTs were installed on horizontal frames with a measurement base of 500 mm. Those were denoted by “BxxT/C” where “xx” stands for the progressive number, “T” refers to the LVDTs installed on the lower flange undergoing tensile strains, and “C” refers to the LVDTs installed on the upper flange of compressive zone. There are 6 “C” and “T” transducers respectively, 3 of which in the loading surface and damage surface[42].

Additionally, the vertical deflection was measured by nine displacement transducers connected to the bottom of the girders, named from “FR01-FR09” (or “D01-D09” equivalently in technical drawing), among which D04-D06 are wire displacement transducers whilst the remaining others are displacement potentiometer transducers.

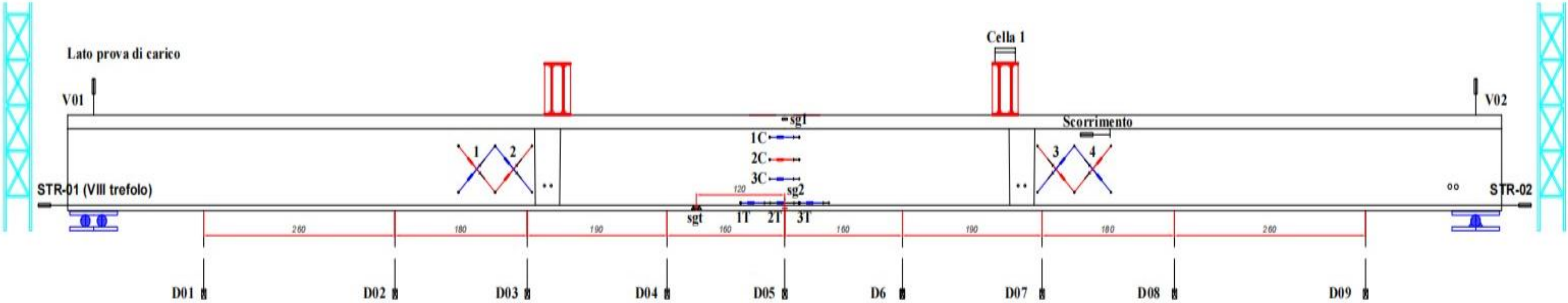

(a)

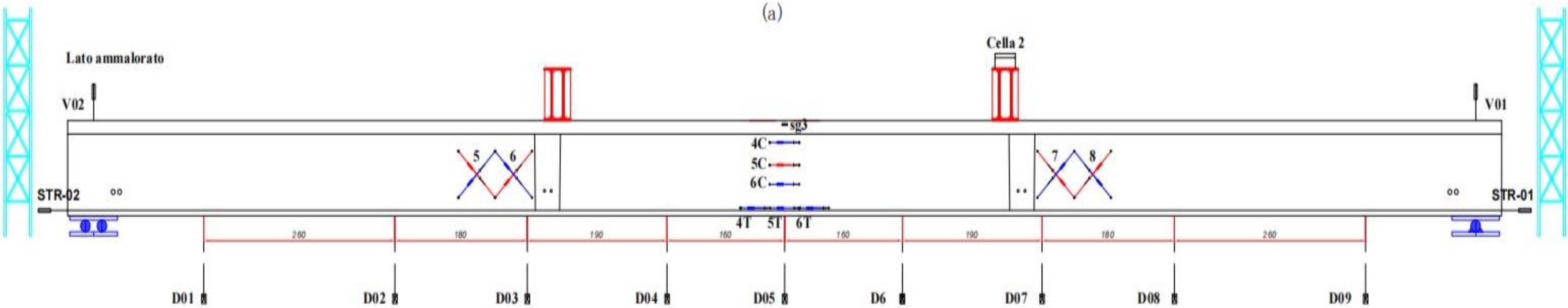

(b)

Figure 6 Layout of sensors
(a)on the loading side; (b)on the damage side.

2.5.2 Acquisition of data

The data could be gathered by the equipment to interface with the sensors and collected constantly throughout the described loading and unloading phases after the sensors have been installed and positioned in the desired positions.

2.5.3 Processing of data

With the help of Analog-to-Digital converters (ADCs), it's possible to process the raw data as needed to extract meaningful physical information. MATLAB code is used to conduct the work of calculations, filtering, statistical analysis and visualization. The diagrams recording the relationship of loading force-time, curves of displacement-time and loading force-displacement for 29 sensors are presented.

2.5.4 Export of results

The global structural response of the box girder to applied load is recorded and presented in this section, in function of time. With an aim of making the test results delivered in a more faithful way and the subsequent analysis in a more intuitive manner, the unit of measurement of displacement is millimeter and time is counted in seconds. The displacement-Time curves of transducer at the bottom of the girder are presented in Figure 7. In this figure, it should be noticed that the recording of transducer "FR7" (drawn in color purple) is uncontrolled, as the observed value is far larger than the effective range the transducer could measure. Hence this parameter is disregarded in the following interpretation.

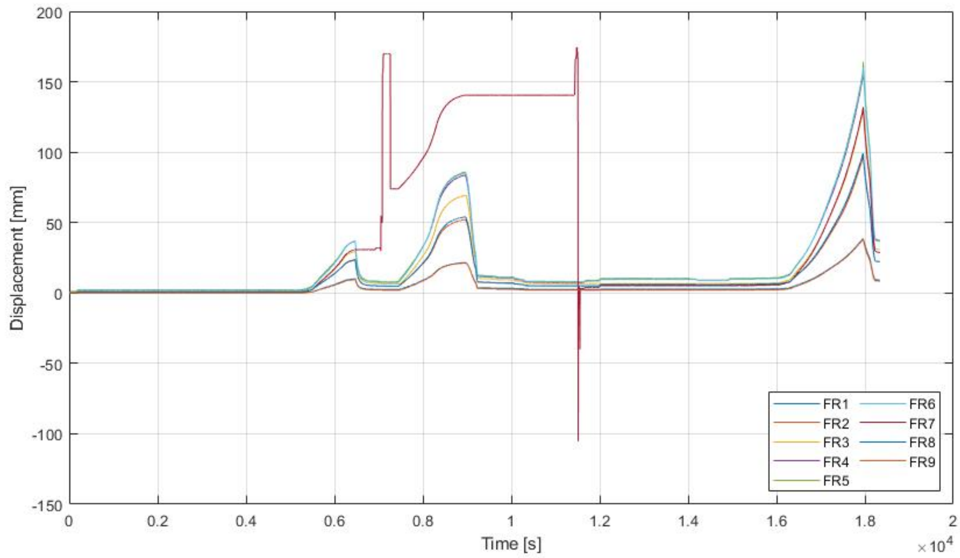

Figure 7 Displacement-Time diagram of transducers FR01-FR09.

The displacement-time curves of transducers in shearing zone are presented in Figure 8. As mentioned previously, both two sides of the box girder are equipped with sensors and are under survey. In this trial, only the sensors on the loading side (SH1-SH4) are of consideration. And due to some technical problems, the raw data from SH3 and SH4 is missing as shown in Figure 8(b), just SH1 and SH2 are deemed.

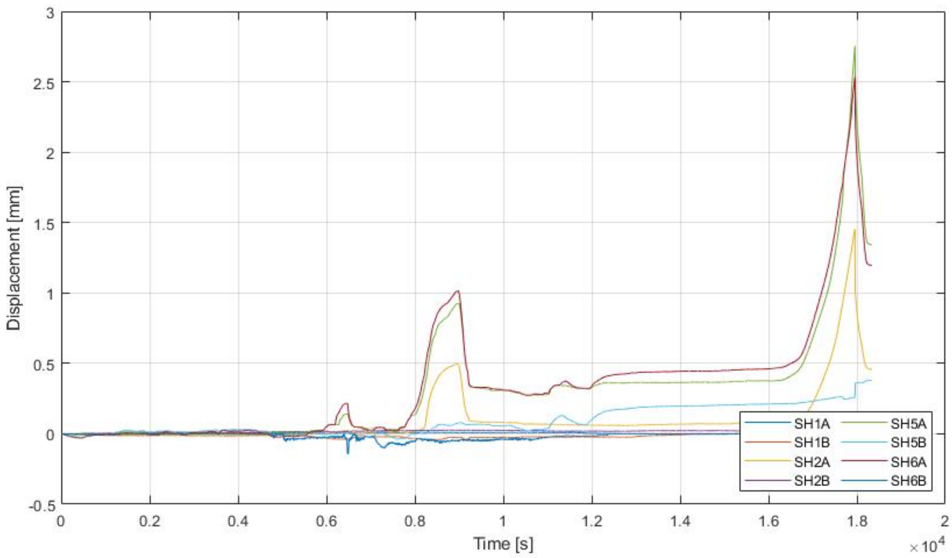

(a)

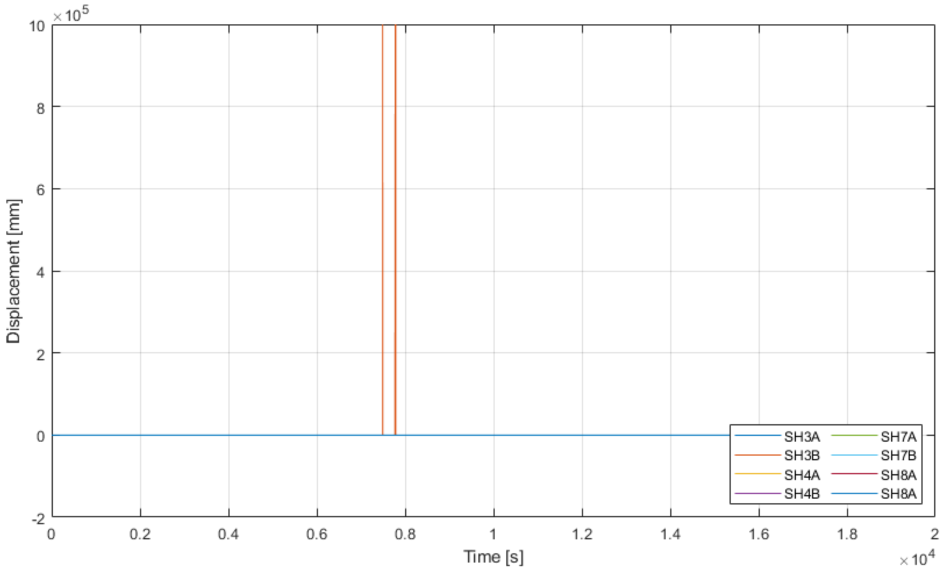

(b)

Figure 8 Displacement-Time diagram of shearing LVDTs
(a)SH1/2/5/6; (b)SH3/4/7/8.

The displacement-time curves of compressive transducers in bending zone are presented in Figure 9, where in the loading side of the girder, B01C, B02C, B03C are installed.

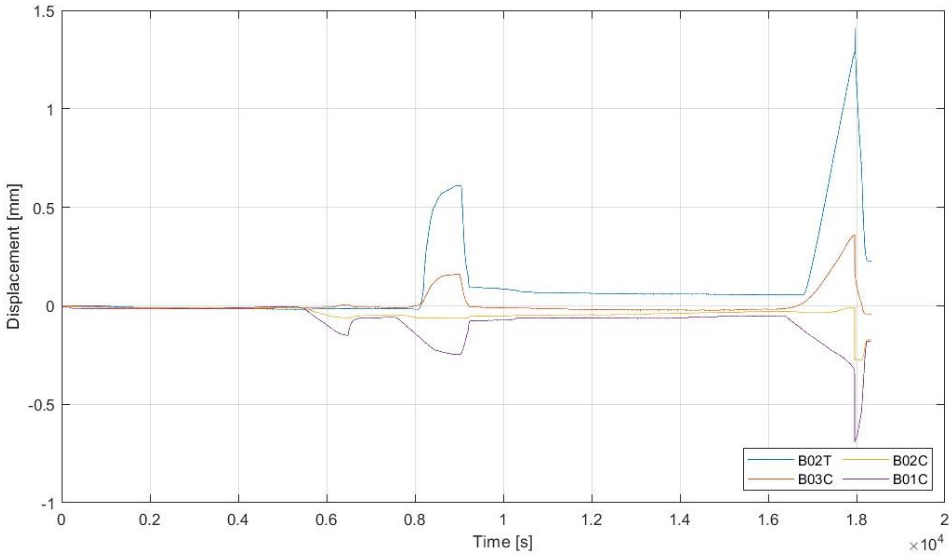

(a)

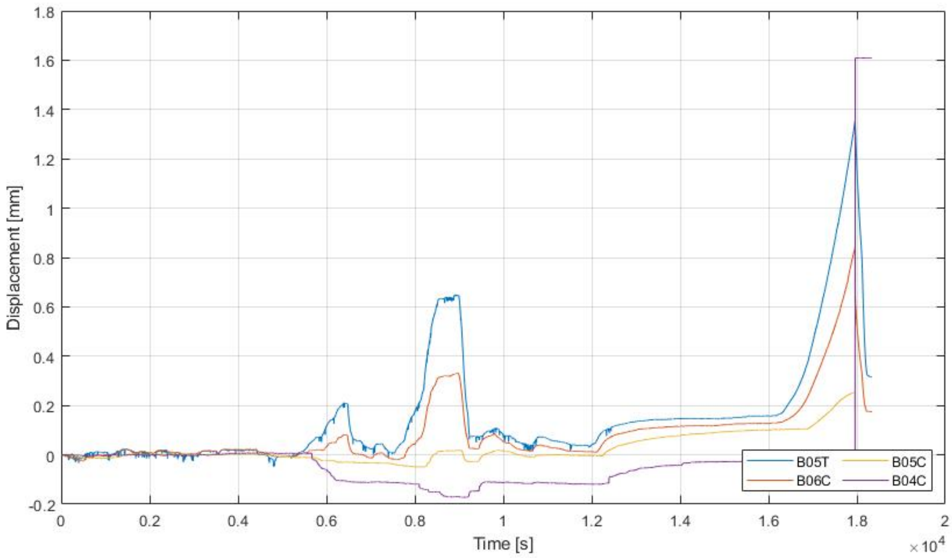

(b)

Figure 9 Displacement-Time diagram of compressive LVDTs
(a)B01/02/03C; (b)B04/05/06C.

The displacement-time curves of tensile transducers in bending zone are presented in Figure 10. In the loading side of the girder, B01T, B02T, B03T are installed.

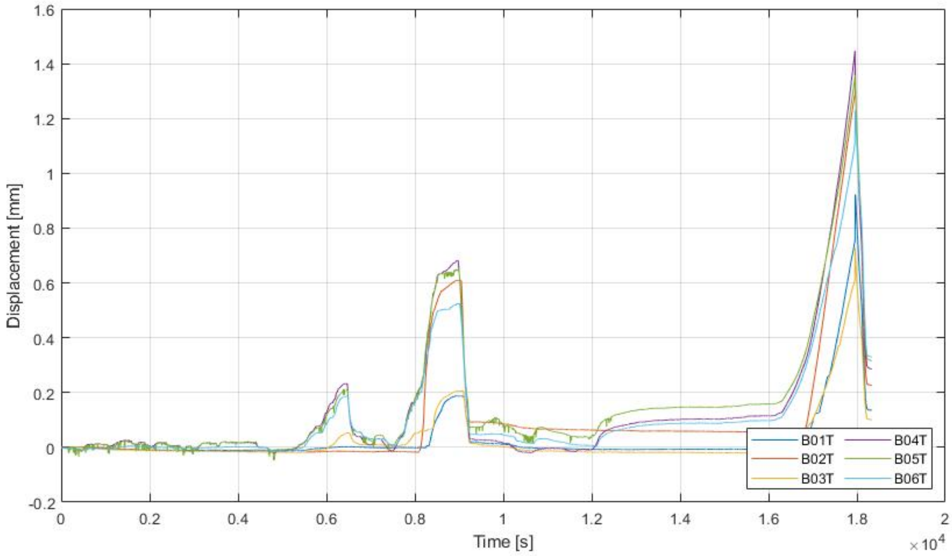

Figure 10 Displacement-Time diagram of tensile LVDTs.

The experimental results at appointed time from the sensors presented and explained above will be used as the standard value to describe the overall response of the box beam in the experiment and will be used as a reference for the results of the photogrammetric monitoring method and subsequent experimental analyses in following sections.

3. Methodology

As a non-contact measurement technique, UAV photogrammetry is used for the reconstruction of the 3D model of an observed object by taking advantages of pictures and images with the adoption of the unmanned reusable motorized aerial vehicles.

3.1 Principle of photogrammetry

Photogrammetry is a technique used for "obtaining reliable information of physical objects and environment through registration, measurement and interpretation processes of photographic and digital images formed by electromagnetic radiant energy and other physical phenomena"[43]. It involves extracting 3D information from 2D images, allowing for the creation of accurate models, maps, and measurements of real-world objects and scenes. The fundamental principle of photogrammetry would be explained in this part.

3.1.1 Image formation

The concepts of projective geometry, which define how 3D objects are projected onto a 2D image plane, are used in photogrammetry. A central projection is used to geometrically represent this process (Figure 11), where collinearity plays an important and fundamental role.

Assumed the location of camera C as (X_0,Y_0,Z_0), any 3D object point P as (X, Y, Z) and its corresponding prospective image p (ξ,η) is formed by the intersection between the collinearity ray CP and the image plane:

$$\xi = \xi_0 - c\frac{r_{11}(X - X_0) + r_{21}(Y - Y_0) + r_{31}(Z - Z_0)}{r_{13}(X - X_0) + r_{23}(Y - Y_0) + r_{33}(Z - Z_0)}$$

$$\eta = \eta_0 - c\frac{r_{11}(X - X_0) + r_{21}(Y - Y_0) + r_{31}(Z - Z_0)}{r_{13}(X - X_0) + r_{23}(Y - Y_0) + r_{33}(Z - Z_0)}$$

where:

ξ_0, η_0 are the principal point.

c is the focal length.

$R = \begin{pmatrix} r_{11} & r_{21} & r_{31} \\ r_{12} & r_{22} & r_{32} \\ r_{13} & r_{23} & r_{33} \end{pmatrix}$, is the rotation matrix expressing the rotation of camera with respect to the reference system, in function of the orientation (ω, ϕ, k) of the camera at the moment of acquisition.

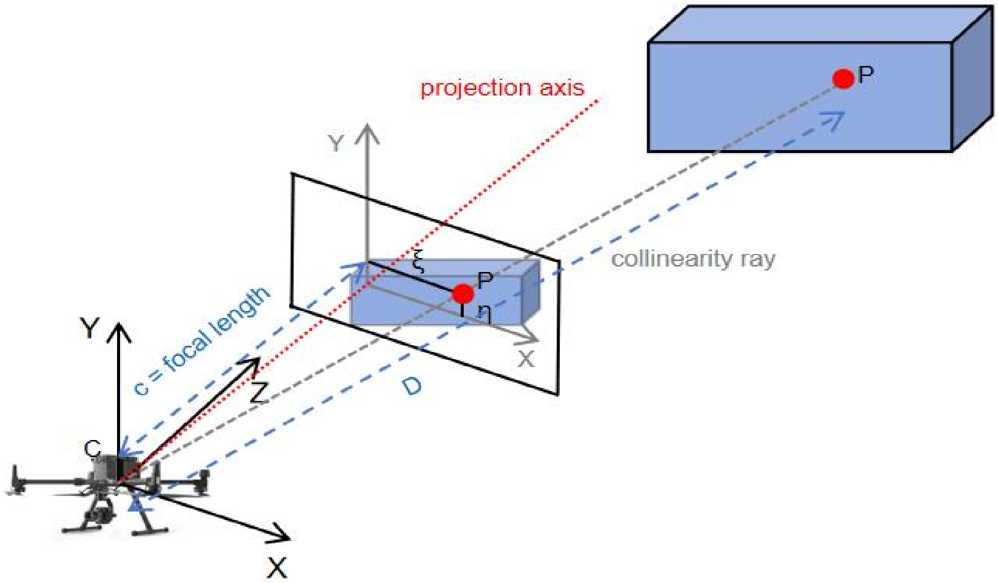

Figure 11 Central projection in single-view geometry.

$$S_f = \frac{c}{D}$$

The image scale S_f is the ratio between the focal length c and the camera distance to the object D. The larger the scale, the greater the precision.

In this case, the estimation of the position C (X_0, Y_0, Z_0) and the orientation (ω, ϕ, k) is required. This system is found to be over-determined as existed: 3 interior orientation parameters (c, ξ_0, η_0) and 3n $(n > 3)$ absolute coordinate of object points Pn= (X_n, Y_n, Z_n), but with only 6 unknowns. Thus, the least mean square estimation is achieved, and the relative orientation of object point is obtained.

3.1.2 Restitution

When the camera moves to the other position, the goal is to create a model from 2 images (Two-view geometry is shown in Figure 12). The position and orientation parameters of camera are known and coordinates of 2 2D image points P (ξ_1, η_1) and Q (ξ_2, η_2) corresponding to the same 3D point P (X_1, Y_1, Z_1) and Q (X_2, Y_2, Z_2), are measured.

For camera at the initial position:

$$\xi_1 = \xi_0 - c\frac{r_{11}(X - X_1) + r_{21}(Y - Y_1) + r_{31}(Z - Z_1)}{r_{13}(X - X_1) + r_{23}(Y - Y_1) + r_{33}(Z - Z_1)}$$

$$\eta_1 = \eta_0 - c\frac{r_{11}(X - X_1) + r_{21}(Y - Y_1) + r_{31}(Z - Z_1)}{r_{13}(X - X_1) + r_{23}(Y - Y_1) + r_{33}(Z - Z_1)}$$

For the second frame from a different camera point than the first one:

$$\xi_2 = \xi_0 - c\frac{r_{11}(X - X_2) + r_{21}(Y - Y_2) + r_{31}(Z - Z_2)}{r_{13}(X - X_2) + r_{23}(Y - Y_2) + r_{33}(Z - Z_2)}$$

$$\eta_2 = \eta_0 - c\frac{r_{11}(X - X_2) + r_{21}(Y - Y_2) + r_{31}(Z - Z_2)}{r_{13}(X - X_2) + r_{23}(Y - Y_2) + r_{33}(Z - Z_2)}$$

It's possible to define the object point $Pn = (X_n, Y_n, Z_n)$ as long as the parallax equation avoidance is satisfied:

$$\vec{b} \wedge \vec{p}_{2i} \times \vec{p}_{1i} = 0 \text{ with } i \geq 5$$

Under this, the estimation of the 3D coordinate of object points $Pn = (X_n, Y_n, Z_n)$ is obtained as there existed: 2 image coordinates for each point $p_i(\xi_i, \eta_i)$ and 3 interior orientation parameters (c, ξ_0, η_0), but with only 5 unknowns about the translation and rotation $(b_y, b_z, w_2, \varphi_2, k_2)$.

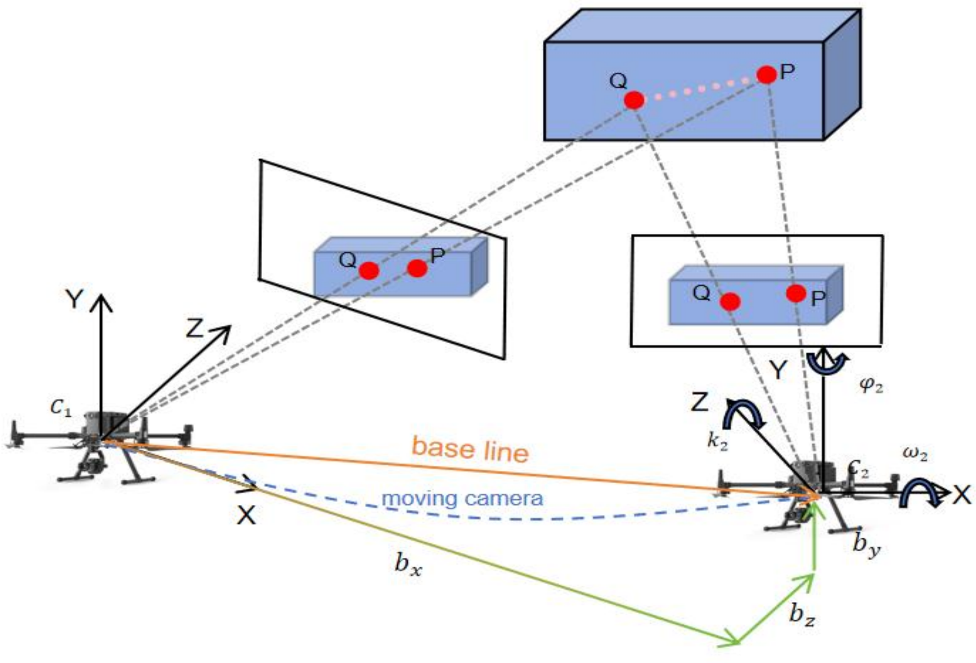

Figure 12 Two-view geometry.

3.1.3 Structure from Motion

This principle mentioned previously can be applied to the multiple-view geometry (shown in Figure 13) when a set of projective measurements represented by a set of 2D images is captured by the camera in different positions.

From this, the Structure from Motion (SfM) approach in computer vision is applied, to reconstruct the 3D model of the structure in a static scene which is represented by a set of 2D images, after the extraction of features from images (points of interest, line, etc.) and the estimation of the movement of camera by determining the relative position between images (in pairs).

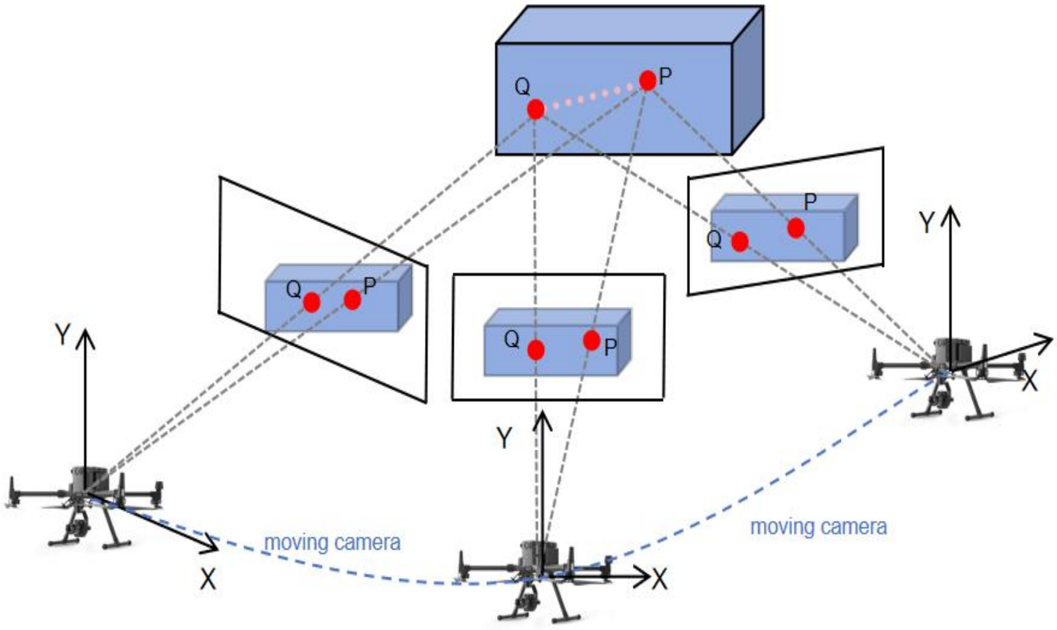

Figure 13 Multiple-view geometry.

3.1.4 UAV and UAV photogrammetry

Unmanned Aerial Vehicles (UAVs), commonly known as drones, have become a significant part of modern technology. For many local (limiting areas) or particular applications (emergency, monitoring, …) they are very effective tools, especially together with a rigorous photogrammetric approach also linked to the SfM techniques.

These aircraft, which are operated remotely or autonomously, offer a wide range of applications and benefits, including aerial surveying and mapping, aerial surveillance and security, aerial inspection of infrastructures and aerial delivery. Considering its low cost, high efficiency and great accessibility, UAVs are widely applied in civil structure and infrastructure equipped with high-resolution camera and other sensors, for example, application of UAV photogrammetry in structural monitoring.

Apparently, the acquisition of images and other related data plays an important and essential role in UAV photogrammetry as it determines the input of analysis and places a direct influence on the final result. Here in this section, some key concepts are addressed.

3.1.4.1 Flight planning

Flight planning for UAV photogrammetry is a crucial step in ensuring the successful capture of high-quality aerial images and data for mapping and surveying purposes. The goal of flight planning is to optimize the flight path of the drone to achieve the desired coverage, accuracy, and resolution while considering safety and regulatory compliance.

Overlap is one of the critical parameters in UAV photogrammetry flight planning, refers to the amount of redundancy or coverage between consecutive images captured during a UAV flight. It is typically expressed as a percentage, involving the overlap of images along both the flight direction (along-track or forward overlap) and across the flight direction (cross-track or lateral overlap).

This essential parameter contributes to the identification and matching of features, reduction of impact of missing or problematic images, augmentation of accuracy and resolution in the reconstruction of 3D model and map. Without too much consideration of time and cost, modern digital techniques and automation have made it more cost-effective to produce accurate orthophoto with higher redundancy and lower residual perspective deformations. A common recommendation is to use around 70-80% along-track overlap and 20-30% cross-track overlap.

3.1.4.2 Ground control points

It is necessary to detect some recognizable points on the frame and they are known as the Ground control points (GCPs), the reference points on the surface with precisely measured coordinates (usually provided by total station).

The GCPs, which might be natural, artificial, and pre-signalized points, are used to georeference and accurately scale the image captured by the UAV during a photogrammetric survey. Additionally, the georeferenced data can be seamlessly integrated with geographic information systems (GIS), enabling spatial analysis, mapping and decision-making based on exact and up-to-date information.

3.1.4.3 Image acquisition

Execution of the flight is performed and subsequently the images are acquired. It's crucial to guarantee safety and image quality during the flight. Particularly for the images, the minimum percentage of overlap is supposed to be respected for the following feature matching and the quality control should be checked to avoid some common problems like motion blur, exposure problems or missing images.

3.2 Optimized photogrammetric workflow

The optimized photogrammetric pipeline consists of several procedures, including pre-processing, photogrammetric process and the exports of final products. (Figure 14)

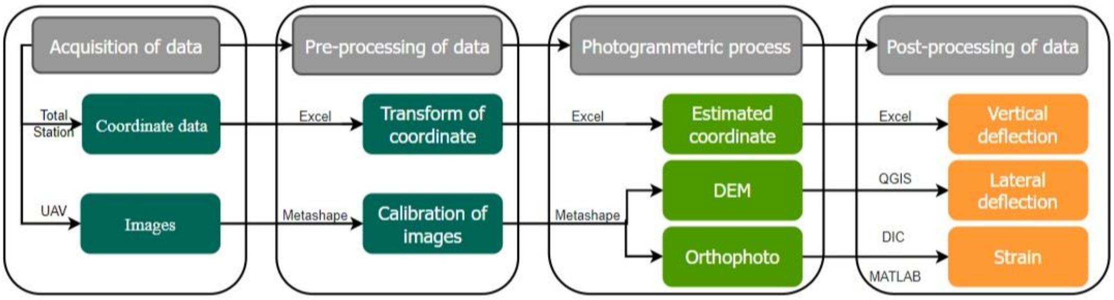

Figure 14 Optimized photogrammetric workflow.

3.2.1 Pre-processing

Before going ahead further, images and data may undergo pre-processing, which includes the corrections for lens distortion, radiometric correction and so on.

Here the transformation of the reference system is highlighted in this section.

Numerical analysis of displacement/deformation on topographic measurements requires a coherent reference system between the ground truth measurements, the topographic and photogrammetric measurements to perform a discrepancy analysis. Therefore, it's fundamental to apply coordinate transformation on original topographic data usually measured in instrumental reference system (RS) or in a georeferenced reference system.

From the instrumental reference system where the center of the total station is the origin, the topographic reference system could be developed and achieved by translation and rotation of the reference system and change of the axial nature. The relationship between the aforementioned two reference systems and the final photogrammetry reference system is presented in Figure 15.

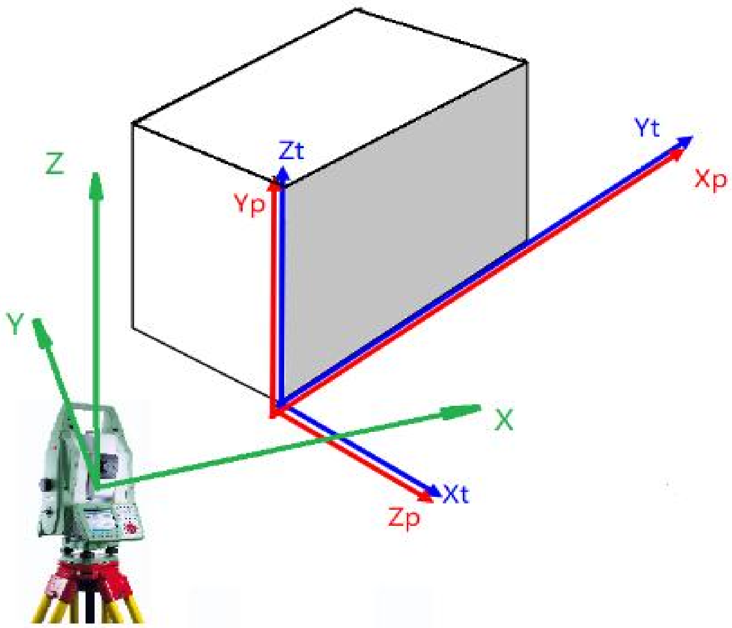

Figure 15 Different reference systems and the object.

The transform can be finished in two steps: firstly, from the instrumental reference system (the green one in Figure 15) to the topographic reference system (the blue one in Figure 15); and secondly, to derive the coordinate data in the photogrammetry reference system. In both cases the aim is always to reach the so-called photogrammetric reference system (the red one in Figure 15).

To perform the transformation of the reference system, it should be noted that 2 specific points are used to define the orientation in the topographic RS, which are the corresponding leftmost and rightmost measuring points in the project. In this case, the parameters a, b, c, and d related to the calculation of coordinates are obtained and varied in separate phases.

The calculation process is shown as follows:

Assumed one point P is measured as (x, y, z) in the instrumental reference system, the relationship between instrumental reference system and the topographic reference system can be found through rotation angle α after projecting the point on the same horizontal plane (Figure 16).

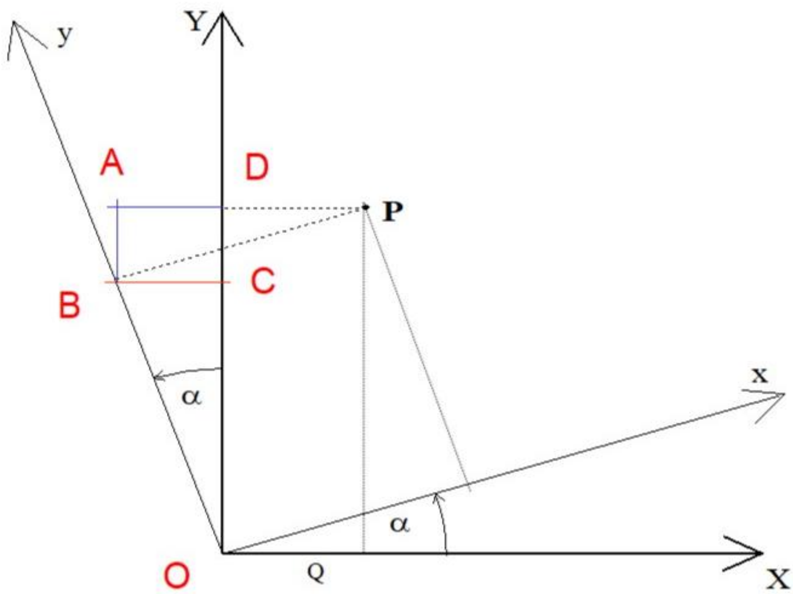

Figure 16 Transform between 2 different reference systems.

The topographic coordinate (X, Y, Z) can be expressed as:

$$\mathrm{Xt} = \mathrm{x}\cos\alpha - \mathrm{y}\sin\alpha + \mathrm{c} \tag{1}$$

$$\mathrm{Yt} = \mathrm{x}\sin\alpha + \mathrm{y}\cos\alpha + \mathrm{d} \tag{2}$$

Where $\sin\alpha = \mathrm{a}, \cos\alpha = \mathrm{b}$. So it can also be presented as:

$$\mathrm{Xt} = -\,\mathrm{ya} + \mathrm{xb} + \mathrm{c} \tag{3}$$

$$\mathrm{Yt} = \mathrm{xa} + \mathrm{yb} + \mathrm{d} \tag{4}$$

Finally, the photogrammetry coordinate can be acquired directly from the previous reference system by changing the direction of axles:

$$Xp = Yt \tag{5}$$

$$Yp = Zt \tag{6}$$

$$Zp = Xt \tag{7}$$

3.2.2 Photogrammetric processing

Agisoft Metashape is a photogrammetry software used for creating 3D models and maps by processing a series of overlapping photos. It is commonly applied in fields like geology, construction and so on. The general workflow displayed in the official guidebook[44] can be utilized in this scenario and it can be done in the following steps.

3.2.2.1 Alignment of photos

First and foremost, image alignment and processing are required after the loading of images. The image alignment establishes the spatial relationships between the camera position at the time of image capture. It's defined by the interior orientation parameters, including camera focal length, lens distortion and so on, together with the exterior orientation parameters. These parameters are calculated using aerotriangluation with bundle block adjustment based on the previously mentioned collinearity equations.

After this processing step, a tie point cloud containing triangulated positions of key points matched across the images is displayed. Besides, depth maps are calculated using stereo matching, for the overlapping image pairs considering their relative orientation parameters. And finally, one combined depth map is generated by merging depths maps for each camera.

3.2.2.2 Georeferencing

Georeferencing involves aligning a set of images to a known coordinate system (as an illustration, the photogrammetry coordinate in this project), or in other words, assigning the real-world 3D coordinate information to the points in the 2D images.

In photogrammetry, triangulation determines the 3D position of a point using its 2D projections from multiple images, while bundle adjustment refines camera positions and 3D coordinates to minimize errors. Feature detection identifies key image features, matched across images to compute camera poses and 3D points. Epipolar geometry (the geometry of stereo vision) establishes the relationship between camera views, enabling the determination of relative positions and orientations. Iterative optimization refines initial estimates through computations, enhancing the accuracy of the reconstructed 3D model.

This process allows that features in the image are accurately located in the Earth's surface, enabling to make measurements, perform spatial queries and so on.

In Metashape, markers can be added manually or detected automatically in images with the photogrammetric coordinate. Literally speaking, the more image data is confirmed in this process, the closer the estimated coordinate values are to the actual coordinate values. Then the estimated coordinates of markers and other interesting points can be viewed and exported.

3.2.2.3 Building of Dense point cloud

Metashape allows to create a point cloud by transforming the combined depth map into the partial point clouds, which are then merged into the definitive version of point cloud with additional noise filtering step applied in the overlapping regions. The point cloud is a collection of 3D estimated coordinates corresponding to the locations of the identified features.

3.2.2.4 Creation of mesh (3D polygonal model)

The reconstruction of polygonal mesh is based on the point cloud information or based on the depth maps data, among which the source data as point cloud will generate high quality output but in longer processing time.

3.2.2.5 Building of texture

Distinctive points or feature points in the images are adapted, serving as reference points for generating 3D models and creating textured models.

3.2.2.6 Building of tiled model

Based on depth maps data, hierarchical tiles format is a good solution for city scale modeling, textured from the source imagery. It allows for responsive visualization of large area 3D models in high resolution.

3.2.2.7 Generation of DEM

Digital elevation model (DEM) is a 2.5D model of a surface represented in a format of a regular grid, with height values stored in each single cell or pixel of the grid.

The preferred DEM of targeted plane can be rasterized from the dense cloud after applying filters to remove noise and unwanted objects which are unnecessary according to the project requirement.

3.2.2.8 Generation of Orthomosaic

Orthomosaic is a combined image created by seamless merging of the original images projected on object surface and transformed to the selected projection (i.e., geographic, planar, or cylindrical). A polygonal model or a DEM can be selected as a surface to which the images will be projected.

However, in some projects moving objects or some other external noises can cause artifacts which interfere with visual quality of the orthomosaic. To eliminate mentioned artifacts, Metashape offers seamline editing tool. The functionality allows users to choose images manually to texture the indicated part of the orthomosaic. Thus, the final orthomosaic can be improved visually according to the user's expectations.

The edition to orthomosaic could be achieved following the suggested steps:

A. Draw a polygon on the orthomosaic using *Draw Polygon* instrument to indicate the area to be retextured.

B. Select *Assign Images...* command from the context menu of the selected polygon.

C. In the *Assign Images* dialog box select the image to texture the area inside the polygon from.

D. Orthomosaic preview on the *Ortho* tab allows to evaluate the results of the selection. Click the *OK* button to finalize the image selection process.

E. Click *Update Orthomosaic* button from the *Ortho* view toolbar to apply the changes.

3.2.2.9 Alignment of chunks

Last but not least, the alignment of chunks is applied to the process of aligning multiple image sets within a project to create a coherent 3D reconstruction of the girder in different phases being captured. It is a crucial step in photogrammetry processing that establishes the spatial relationships between the photos and enables the generation of an accurate and complete 3D model.

3.2.3 Export of results

A large variety of results are available after the photogrammetric process. Depending on the specific project requirements and goals, the export format and type of data may vary. Generally, 3D models in format of OBJ, point cloud data in LAS, DEM, DSM and Orthophoto in PNG, GeoTIFF and TIFF, together with the reports in PDF, are useful for the subsequent analysis and visualization.

3.3 Post-processing of photogrammetric products

After obtaining the interesting products from Metashape, further post-processing work is needed to a direct and deepen understanding of the structural performance.

3.3.1 Estimated coordinates

During the photogrammetric process, Metashape estimates the 3D coordinates of various points based on the analysis of corresponding points in multiple 2D images.

The estimated coordinates of the feature points could be applied to compute the displacement and strains of the structure with a mathematical and numerical process.

All the analysis in this study is based on the computation of 3D-plane distance of lines:

$$D_{ij} = \sqrt{(x_i - x_j)^2 + (y_i - y_j)^2 + (z_i - z_j)^2} \tag{8}$$

where i and j are the end point for each single line.

This calculation work will be finished in Microsoft Excel.

3.3.2 DEM

DEM is the digital representation of ground surface topography or terrain, supplying a detailed and correct description of the surface through a grid of regularly spaced elevation points. DEM data is typically collected using various techniques (i.e., photogrammetry) and stored as a raster data structure where each single cell contains an elevation value.

In Metashape, the creation of a DEM involves using the data generated from photogrammetric processes to create a detailed 3D model of the elevation data. Once the DEMs of interesting surfaces are obtained, the deformation analysis can be conducted in QGIS, based on the DEM of difference (DoD).

DoD is a geospatial analysis technique used to compare two or more DEMs acquired at different times. It involves subtracting the elevation values of one reference DEM from the corresponding elevation values of other DEM to visualize and quantify changes in the surface over time. The resulting DoD highlights the variation in elevation, reflecting the changes in subsidence, settlement and any other movements that might affect the integrity of the infrastructure.

Although QGIS does not have native support for full deformation analysis, the combination with other plugins and processing tools to achieve certain aspects of the analysis is possible.

3.3.3 Orthophoto

Commonly employed in the field of remote sensing and photogrammetry, orthomosaic relates to the process of creating a high-resolution, georeferenced, and orthorectified image or map through the compilation of a large set of individual images.

Digital image correlation (DIC) is a powerful technique used in engineering to measure full-field displacements and strains on the surface of an object under loading.

When it comes to using orthophoto in DIC, the high-resolution and accurate representation of object surface provided by orthomosaics can be extremely beneficial. This high-quality visual data can significantly improve the accuracy of DIC measurements, especially in large-scale projects where precise surface information is critical.

In this present study, this work is performed with Ncorr, an open source 2D digital image correlation MATLAB program. While Ncorr itself is not designed for handling orthomosaic images, the utilizing orthophoto in DIC analysis follows a general workflow that involves integrating high-resolution surface information from orthophoto with the displacement and strain data obtained from the DIC process.

Basically, images of a set of samples are taken and used as inputs to a DIC program. The idea is to somehow obtain a one-to-one correspondence between material points in the reference (initial undeformed picture) and current (subsequent deformed pictures) configurations. DIC does this by taking small subsections of the reference image, called subsets (shown in Figure 17, where subset's coordinates are shown as red crosses), and deciding their respective locations in the current configuration.

For each subset, displacement and strain information are obtained through the transformation used to match the location of the subset in the current configuration. Many subsets are picked in the reference configuration, often with a spacing parameter to reduce computational cost[45]. The end result is a grid containing displacement and strain information with respect to the reference configuration, also referred to as Lagrangian displacements and strains.

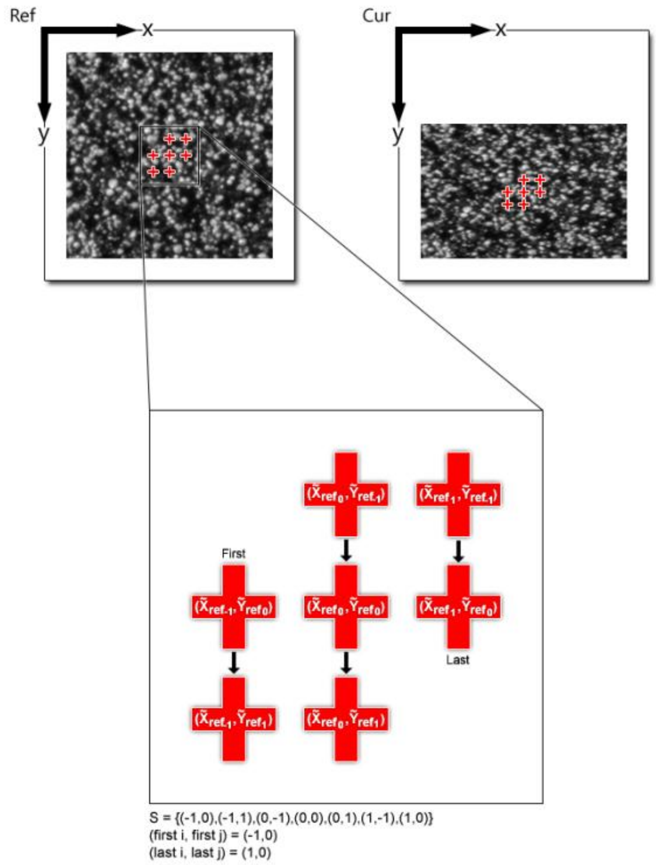

Figure 17 The idea of subsets.

The displacement in each direction is considered from plane parameters:

$$u_{plane}(x, y) = a_{u,plane} + \left(\frac{\partial u}{\partial x_{plane}}\right)x + \left(\frac{\partial u}{\partial y_{plane}}\right)y \tag{9}$$

$$v_{plane}(x, y) = a_{v,plane} + \left(\frac{\partial v}{\partial x_{plane}}\right)x + \left(\frac{\partial v}{\partial y_{plane}}\right)y \tag{10}$$

While the Green-Lagrangian strains are calculated from obtained by using the four displacement gradients as shown below:

$$E_{xx} = \frac{1}{2}\left(2\frac{\partial u}{\partial x} + \left(\frac{\partial u}{\partial x}\right)^2 + \left(\frac{\partial v}{\partial x}\right)^2\right) \tag{11}$$

$$E_{xy} = \frac{1}{2}\left(\frac{\partial u}{\partial y} + \frac{\partial v}{\partial x} + \frac{\partial u}{\partial x}\frac{\partial u}{\partial y} + \frac{\partial v}{\partial x}\frac{\partial v}{\partial y}\right) \tag{12}$$

$$E_{yy} = \frac{1}{2}\left(2\frac{\partial v}{\partial y} + \left(\frac{\partial u}{\partial y}\right)^2 + \left(\frac{\partial v}{\partial y}\right)^2\right) \tag{13}$$

4. Case study

In the present case study, a set of geomatics techniques are applied to extract information about the shape, size, and spatial properties of the bridge girder by analyzing hundreds of thousands of images taken from different views during different experimental phases.

In this study, only the first two cycles are being investigated due to poor and dim sunlight as the sun had gone down. Six different experimental stages are under survey, and each is analyzed within one Agisoft Metashape project, numbered "041"- "046". The overview of the loading cycles is shown as follows in Table 2 and the external loading force in function of time is presented in Figure 18.

Experimental Stages	External forces (F1=F2) [KN]	Time	Time point [s]	Photogrammetry Project
Original	0.00	12:00	0	041
Instrumentation	0.50	13:35	1500	042
First loading	130.00	15:00	6500	043
First unloading	8.50	15:08	7000	044
Second loading	180.00	15:34	8500	045
Second unloading	0.20	15:49	10000	046
Third loading	\	\	\	\
Third unloading	\	\	\	\

Table 2 Overview of loading cycles.

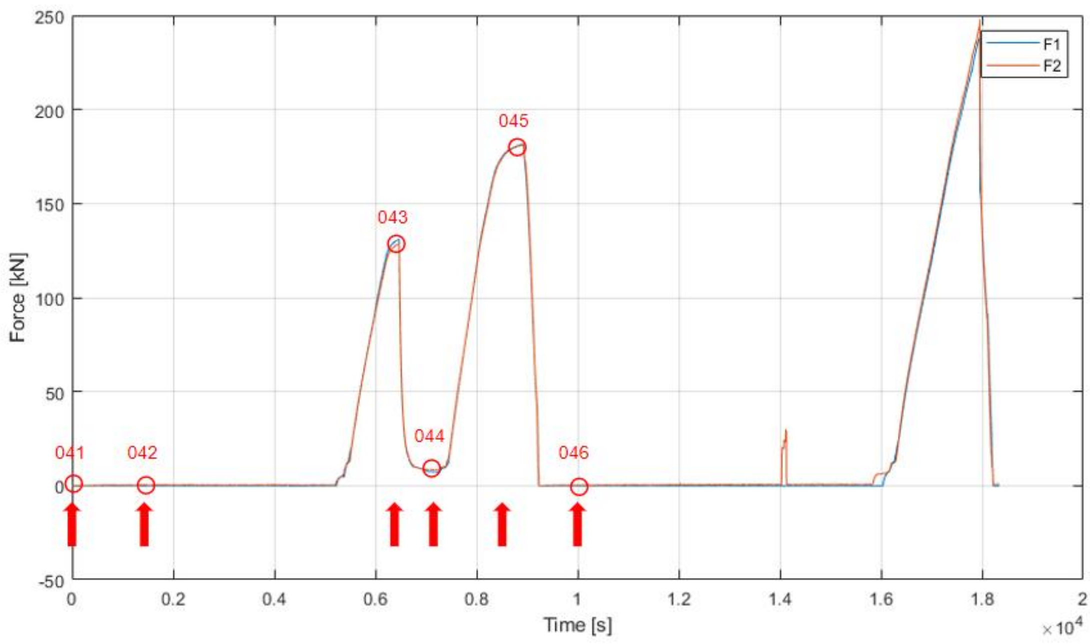

Figure 18 External loading forces in function of time.

4.1 Acquisition of data

With respect to the measurement and assessment of the test subject during the in-situ experiment, the total station and UAV is applied to collect the coordinate information of specific ground control points and the high-resolution images of the whole structural element.

4.1.1 Acquisition of coordinate information

It is feasible to obtain a precise value for the coordinate information of the objects of interest with the aid of a total station. In this case, the Leica Nova MS50 MultiStation offers complete versatility to present trustworthy results with the benefit of connection to GNSS, in addition to the typical total station functions that are supplemented by sensors for high precision and performance in fully automated surveying processes[46]. With numbers ranging from 01 to 08, from left to right, the arrangement of the 8 artificial markers, known as GCPs, on the loading surface has been determined in this case throughout the beam. The marker is depicted in Figure 19 and the relative position of the markers on the beam is shown on the 3D model in Figure 20.

So the precise instrumental coordinate data of 8 markers in 6 different phases is obtained and can be employed to fix the beam in a local reference system (topographic and photogrammetry RS) in order to estimate the corresponding spatial information of all feature points.

4.1.2 Acquisition of images

The aerial imaging solution DJI-Zenmuse P1, which is meant to revolutionize the field of photogrammetry, is used to take high-resolution photographs for photogrammetry work. The Zenmuse P1 enables professionals in fields like surveying, mapping, and construction to collect incredibly precise and detailed aerial photos for 3D modeling and mapping projects due to its cutting-edge technology and precision capabilities. Equipped with a large, 45-megapixel full-frame sensor and a high-quality 35mm lens, this drone-mounted camera delivers exceptional image quality and clarity. Its efficient one-inch CMOS sensor ensures precise image capture, making it ideal for capturing the intricate details required for photogrammetric applications[47]. Other properties are presented in Table 3.

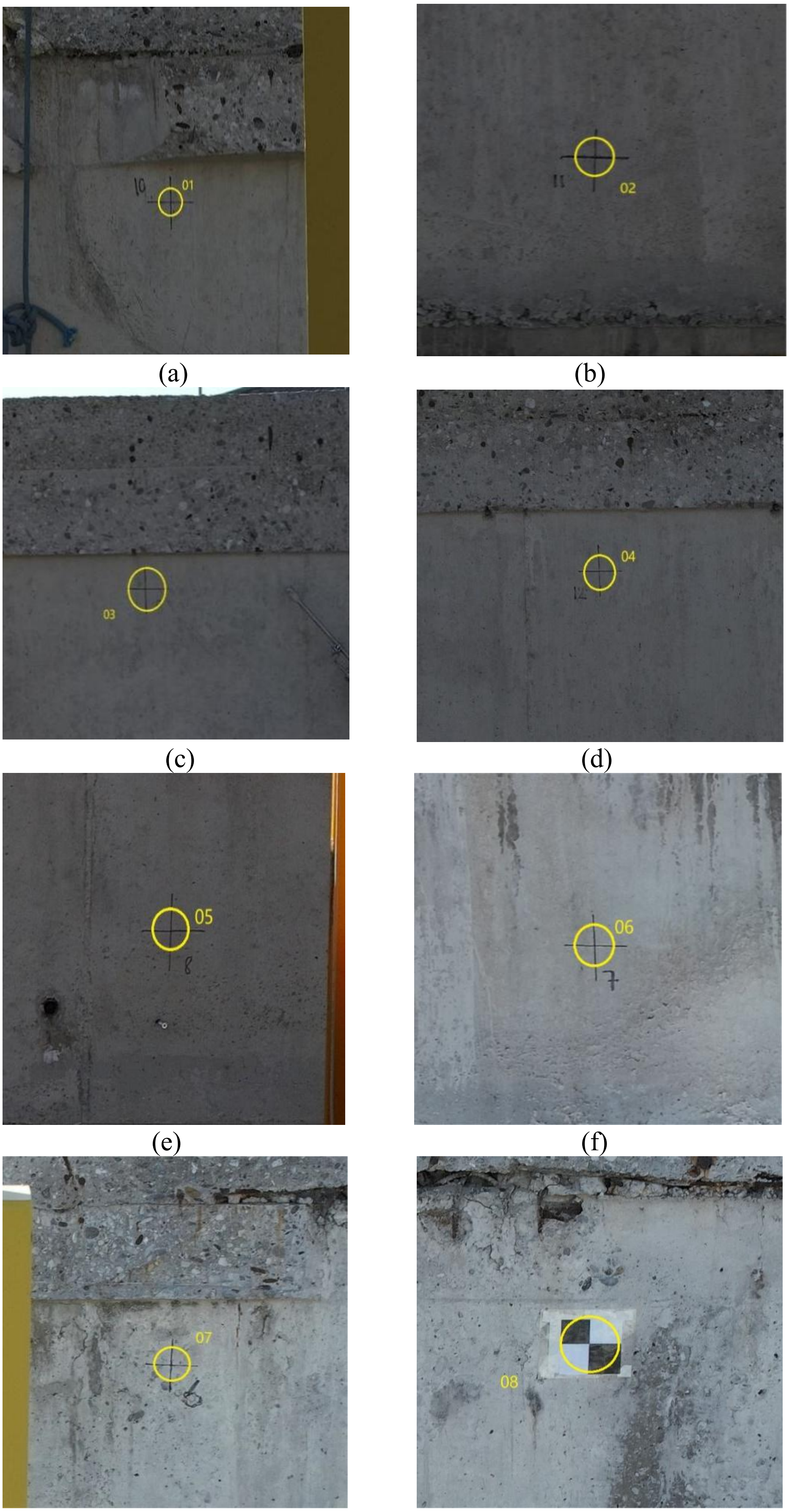

(a) (b)
(c) (d)
(e) (f)
(g) (h)

Figure 19 8 markers on the beam surface
(a)01; (b)02; (c)03; (d)04; (e)05; (f)06; (g)07; (h)08.

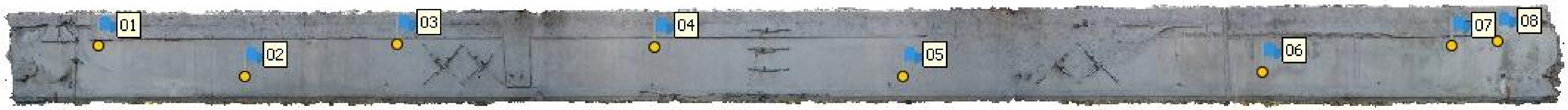

Figure 20 Relative position of 8 markers on the beam surface.

	Property	Value
Camera DJI Zenmuse P1	F-stop	f/5.6
	Exposure time	1/1600 sec
	ISO speed	ISO-1600
	Focal length	35 mm
	Metering mode	Center Weighted Average
Image	Dimensions	8192*5460
	Horizontal/Vertical resolution	72 dpi
Advanced photo	Contrast	Normal
	Light source	Daylight
	Exposure program	Manual
	Saturation	Normal
	Sharpness	Normal
	White balance	Auto

Table 3 Properties of camera and images.

As a direct consequence of the integration between Zenmuse P1 and DJI robust drone platforms, reliability and usability are guaranteed, enabling users to gather data effectively and consistently. The DJI Zenmuse P1 is a significant change in the field of photogrammetry, offering the accuracy and dependability required to take on challenging tasks with confidence, whether in mapping expansive landscapes, observing building progress, or conducting environmental evaluations.

The DJI Zenmuse P1 is commonly employed as an auxiliary payload compatible with select DJI drones, including the Matrice 300 RTK. Through this integration, the Matrice 300 RTK serves as a robust and dependable platform, facilitating the deployment of the Zenmuse P1 in diverse aerial surveying and mapping operations, thus ensuring the precise collection of data. The sophisticated flight control mechanisms and safety features of the Matrice 300 RTK complement the Zenmuse P1's capabilities in high-resolution imaging and data processing. Consequently, this combined solution is well-suited for challenging industrial and commercial applications that demand thorough and correct aerial data acquisition. Industries such as construction, infrastructure inspection, and environmental monitoring can greatly benefit from this comprehensive and streamlined aerial solution.

A series of overlapping photographs of the testing girder together with surrounding environment are captured and cover the object from different viewpoints. Overview of the drone's flight is detailed in Table 4, including the number of images captured in every stage, the number of flying strips in each survey, and the time cost.

Project	Number of images captured	Number of flying strips	Time of acquisition [mins]
041	187	4	4
042	156	3	3
043	150	3	3
044	108	3	2
045	155	3	2
046	156	3	3

Table 4 Overview of the drone's flight.

4.2 Pre-pocessing of data

The processing of data is performed simultaneously in the software Microsoft Excel and Agisoft Metashape. In Microsoft Excel the location data of the markers and other interesting points are calculated and processed numerically and mathematically, while in Agisoft Metashape the 3D reconstruction of the model is completed.

4.2.1 Original coordinate in Instrumental reference system

After defining the coordinate of the total station as the origin of the instrumental reference system, a point named as "1000" in the Y axis and quite far away from the origin is also defined. The original coordinates in the instrumental reference system (the reference system draw in green in Figure 15) of the center point of the mentioned 8 markers are obtained in software Leica Infinity. It is easier to define an ideal horizontal plane on which all points are projected once point "1000" is defined.

The spatial relationship between the instrumental reference system and the bridge girder is presented in Figure 15. All available original instrumental coordinates are displayed in Table 6, where the blank spaces in the Table are missing data due to technical reasons.

4.2.2 Topographic and Photogrammetry reference system

As mentioned in section 3.2.1, the transformation of reference system is conducted where markers 01 and 08 are used for the purpose of orientation in each project. Parameters a, b, c, and d related to the calculation of coordinates are obtained and varied in different phases, shown in Table 5.

Phases	041	042	043	044	045	046
a	0.371778736	0.371775807	0.371687895	0.371666341	0.371506045	0.371583223
b	-0.928321373	-0.928322546	-0.928357748	-0.92836637	-0.928430535	-0.928399649
c	25.55532762	25.55553129	25.55788794	25.55745533	25.55964545	25.55888437
d	10.22013923	10.22042964	10.22407458	10.22471462	10.23081711	10.22811253

Table 5 Values of a, b, c, d in coordinate transform.

In project 044, the coordinate data of marker 01 is missing, so the values of a, b, c, and d are calculated as the average of parameters from the other 5 projects.

The topographic position information of GCPs is calculated with equation (3)-(4), shown in Table 7 and the photogrammetry coordinate can be acquired with equation (5)-(7), shown in Table 8. Table 9 displays the estimated of markers, which will be detailed in 4.4.1.

4.3 Photogrammetric processing

The optimal photogrammetric procedure is described to extract exact 3D information of the observed items in this part, following the direct import of photos into the Agisoft Metashape environment, as seen in Figure 21.

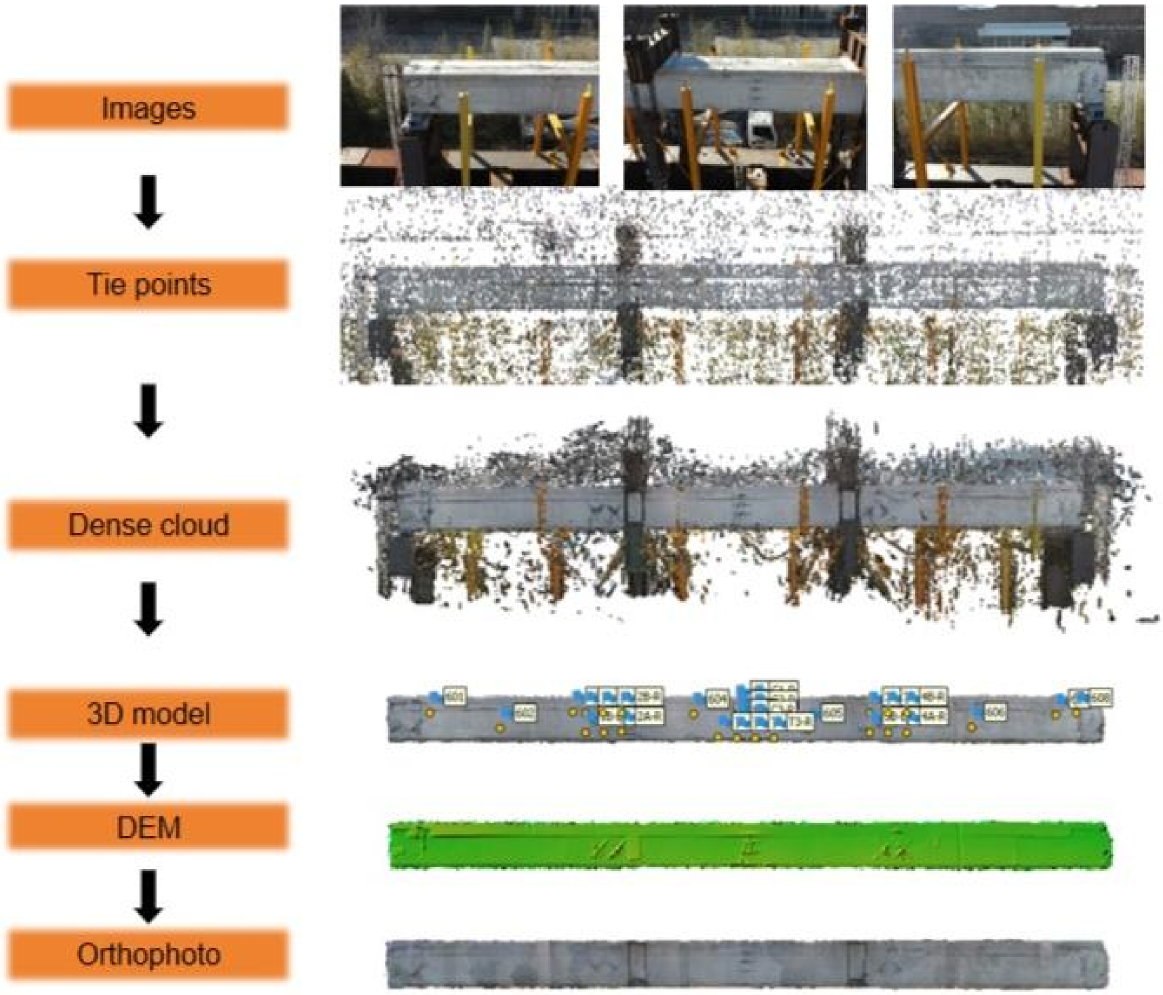

Figure 21 Optimized photogrammetric processing.

	Phase	41 Original			42 Instrumentation			043 First loading			044 First unloading			045 Second loading			046 Second unloading		
	Marks	**x**	**y**	**z**	**x**	**y**	**z**	**x**	**y**	**z**	**x**	**y**	**z**	**x**	**y**	**z**	**x**	**y**	**z**
	001	14.3585	5.9875	4.3697	14.3586	5.9878	4.3699	14.3600	5.9907	4.3643				14.3603	5.9948	4.3596	14.3601	5.9932	4.3636
	002	15.0524	4.2077	3.9723	15.0535	4.2075	3.9720	15.0538	4.2123	3.9633							15.0532	4.2099	3.9687
	003	15.7885	2.3604	4.3880	15.7899	2.3611	4.3872										15.7917	2.3632	4.3814
Original coordinate in instrumental reference system	004	17.0134	-0.6896	4.3423	17.0148	-0.6895	4.3412	17.0181	-0.6839	4.3092	17.0164	-0.6871	4.3364				17.0164	-0.6870	4.3332
	005	18.1673	-3.5973	3.9593	18.1688	-3.5970	3.9575				18.1694	-3.5951	3.9530	18.1733	-3.5903	3.9002	18.1699	-3.5949	3.9498
	006	19.8226	-7.7240	3.9928	19.8237	-7.7238	3.9934	19.8241	-7.7197	3.9750	19.8227	-7.7216	3.9904	19.8245	-7.7185	3.9599	19.8238	-7.7223	3.9891
	007				20.7069	-9.8678	4.3090	20.7062	-9.8634	4.3032	20.7061	-9.8649	4.3084	20.7032	-9.8600	4.2979	20.7062	-9.8661	4.3088
	008	20.9156	-10.3854	4.3551	20.9156	-10.3850	4.3556	20.9142	-10.3796	4.3528	20.9157	-10.3831	4.3554	20.9115	-10.3773	4.3493	20.9146	-10.3832	4.3557

Table 6 Original coordinate in instrumental reference system.

	Phase	41 Original			42 Instrumentation			043 First loading			044 First unloading			045 Second loading			046 Second unloading		
	Marks	**x**	**y**	**z**	**x**	**y**	**z**	**x**	**y**	**z**	**x**	**y**	**z**	**x**	**y**	**z**	**x**	**y**	**z**
	001	10.0000	10.0000	4.3697	10.0000	10.0000	4.3699	10.0000	10.0000	4.3643				10.0000	10.0000	4.3596	10.0000	10.0000	4.3636
	002	10.0175	11.9102	3.9723	10.0168	11.9110	3.9720	10.0169	11.9089	3.9633							10.0192	11.9132	3.9687
	003	10.0210	13.8988	4.3880	10.0196	13.8989	4.3872										10.0198	13.9020	4.3814
Topographic coordinate	004	10.0178	17.1855	4.3423	10.0166	17.1862	4.3412	10.0132	17.1844	4.3092	10.0154	17.1870	4.3364				10.0161	17.1889	4.3332
	005	10.0276	20.3138	3.9593	10.0263	20.3143	3.9575				10.0258	20.3152	3.9530	10.0208	20.3157	3.9002	10.0258	20.3172	3.9498
	006	10.0252	24.7601	3.9928	10.0243	24.7606	3.9934	10.0234	24.7591	3.9750	10.0246	24.7606	3.9904	10.0214	24.7618	3.9599	10.0240	24.7637	3.9891
	007				10.0015	27.0793	4.3090	10.0012	27.0771	4.3032	10.0011	27.0787	4.3084	10.0012	27.0765	4.2979	10.0013	27.0819	4.3088
	008	10.0000	27.6371	4.3551	10.0000	27.6370	4.3556	10.0000	27.6336	4.3528	9.9991	27.6377	4.3554	10.0000	27.6342	4.3493	10.0000	27.6394	4.3557

Table 7 Topographic coordinate.

	Phase	41 Original			42 Instrumentation			043 First loading			044 First unloading			045 Second loading			046 Second unloading		
	Marks	x	y	z	x	y	z	x	y	z	x	y	z	x	y	z	x	y	z
Photogrammetry coordinate	001	10.0000	4.3697	10.0000	10.0000	4.3699	10.0000	10.0000	4.3643	10.0000				10.0000	4.3596	10.0000	10.0000	4.3636	10.0000
	002	11.9102	3.9723	10.0175	11.9110	3.9720	10.0168	11.9089	3.9633	10.0169							11.9132	3.9687	10.0192
	003	13.8988	4.3880	10.0210	13.8989	4.3872	10.0196										13.9020	4.3814	10.0198
	004	17.1855	4.3423	10.0178	17.1862	4.3412	10.0166	17.1844	4.3092	10.0132	17.1870	4.3364	10.0154				17.1889	4.3332	10.0161
	005	20.3138	3.9593	10.0276	20.3143	3.9575	10.0263				20.3152	3.9530	10.0258	20.3157	3.9002	10.0208	20.3172	3.9498	10.0258
	006	24.7601	3.9928	10.0252	24.7606	3.9934	10.0243	24.7591	3.9750	10.0234	24.7606	3.9904	10.0246	24.7618	3.9599	10.0214	24.7637	3.9891	10.0240
	007				27.0793	4.3090	10.0015	27.0771	4.3032	10.0012	27.0787	4.3084	10.0011	27.0765	4.2979	10.0012	27.0819	4.3088	10.0013
	008	27.6370	4.3556	10.0000	27.6370	4.3556	10.0000	27.6336	4.3528	10.0000	27.6377	4.3554	9.9991	27.6342	4.3493	10.0000	27.6394	4.3557	10.0000

Table 8 Photogrammetric coordinate.

	Phase	41 Original			42 Instrumentation			043 First loading			044 First unloading			045 Second loading			046 Second unloading		
	Marks	x	y	z	x	y	z	x	y	z	x	y	z	x	y	z	x	y	z
Estimated coordinate	001	10.0009	4.3690	9.9986	10.0015	4.3697	10.0000	10.0014	4.3658	9.9996	10.0025	4.3699	9.9988	10.0013	4.3621	10.0018	10.0024	4.3672	10.0011
	002	11.9112	3.9726	10.0165	11.9110	3.9723	10.0167	11.9088	3.9596	10.0167	11.9126	3.9709	10.0183	11.9061	3.9474	10.0182	11.9123	3.9676	10.0188
	003	13.8980	4.3878	10.0231	13.8983	4.3869	10.0199	13.8972	4.3653	10.0177	13.9004	4.3837	10.0185	13.8955	4.3439	10.0156	13.9006	4.3798	10.0198
	004	17.1846	4.3427	10.0196	17.1851	4.3413	10.0163	17.1822	4.3109	10.0141	17.1870	4.3363	10.0148	17.1817	4.2794	10.0083	17.1882	4.3320	10.0147
	005	20.3131	3.9593	10.0281	20.3135	3.9579	10.0263	20.3108	3.9269	10.0245	20.3150	3.9527	10.0266	20.3117	3.8950	10.0202	20.3168	3.9489	10.0261
	006	24.7602	3.9937	10.0264	24.7604	3.9927	10.0245	24.7584	3.9754	10.0232	24.7610	3.9899	10.0245	24.7613	3.9601	10.0221	24.7636	3.9893	10.0244
	007	27.0793	4.3082	10.0001	27.0797	4.3093	10.0016	27.0766	4.3031	10.0014	27.0794	4.3080	10.0006	27.0777	4.2991	10.0007	27.0820	4.3094	10.0013
	008	27.6381	4.3539	9.9978	27.6378	4.3557	9.9999	27.6356	4.3522	9.9990	27.6376	4.3551	9.9996	27.6366	4.3510	9.9996	27.6401	4.3569	9.9999

Table 9 Estimated coordinate.

4.3.1 Alignment of photos

To align the imported images, go to the "*Workflow*" menu and choose "*Align Photos*". Metashape will automatically match and align the photos based on the features it detects. The alignment parameters are shown in Table 10.

Alignment parameters		
Accuracy		High
Generic preselection		Yes
Reference preselection		Source
Key point limit		10,000
Key point limit per Mpx		40,000
Tie point limit		10,000
Matching time	041	28 mins 14 s
	042	24 mins 14 s
	043	49 mins 42 s
	044	45 mins 37 s
	045	52 mins 02 s
	046	35 mins 25 s

Table 10 Alignment parameters.

4.3.2 Georeferencing

This process allows feature points in the image to be accurately located on the surface. In this section, the known photogrammetry coordinates of GCPs are input manually to the corresponding GCPs.

4.3.3 Build of dense point cloud

Once the alignment is optimized and satisfied, it's supposed to proceed to build a dense point cloud (DPC) from the aligned images. Go to "*Workflow*" menu and select "*Build Dense Cloud*" or "*Build Tiled Model*". The depth maps generation parameters are shown in Table 11.

Depth maps generation parameters		
Quality		High
Filtering mode		Mild
Processing time	041	1 h 48 mins
	042	1 h 18 mins
	043	1 h 20 mins
	044	4 mins 10 s
	045	59 mins 59 s
	046	2 h 22 mins

Table 11 Depth maps generation parameters.

With the input coordinates of GCPs, 3D position of each feature point is calculated, known as "estimated coordinate". In other words, the point cloud is a collection of 3D coordinates corresponding to the locations of the identified features.

4.3.4 Creation of mesh and texture

Create a 3D mesh and apply textures to projects since Metashape provides tools for mesh and texture generation under the "*Workflow*" menu. The model reconstruction parameters are shown in Table 12.

Reconstruction parameters		
Surface type		Arbitrary
Source data		Dense cloud
Interpolation		Disabled
Strict volumetric masks		No
Processing time	041	3 mins 45 s
	042	4 mins 13 s
	043	2 mins 36 s
	044	1 mins 54 s
	045	6 mins 39 s
	046	3 mins 59 s

Table 12 Reconstruction parameters for 3D model.

4.3.5 Generation of DEM and Orthophoto

With the dense point cloud, a DEM can be generated, also under the "*Workflow*" menu. Configure the settings for DEM generation, including the resolution and format, shown in Table 13. In this project, the DEM of the loading surface in XY plane is established separately for each single project, depicted in Figure 25.

DEM		
Coordinate system		Local coordinate
Source data		Dense cloud
Interpolation		Disabled
Processing time	041	08 s
	042	14 s
	043	19 s
	044	18 s
	045	19 s
	046	17 s

Table 13 Reconstruction parameters for DEM.

An orthomosaic is a georeferenced and high-resolution aerial image. Orthorectification allows to measure the field distances as the orthophoto is an accurate representation of the surface, having been adjusted for topographic relief, lens distortion and camera tilt. After building the texture, use the "*Build Orthomosaic*" function to generate the orthomosaic. Configure and uniform the resolution of the output with the minimum resolution of built DEMs: 0.001. Reconstruction parameters are shown in Table 14.

However, there are some side effects from external environments on the form of orthomosaic. The examples used for illustration here are all from project "042", right span of beam. There exists the supporting frame (the yellow frameworks in Figure 22) and loading frame (the iron framework in Figure 22). These artifacts are directly projected in the orthomosaic, shown in Figure 23. With the modification explained in section 3.2.2.8, the final orthomosaic with clear visuals is obtained, presented in Figure 24. The Orthophotos of the loading surface for each single project are rendered in Figure 26.

Orthomosaic		
Coordinate system		Local coordinate
Blending mode		Mosaic
Surface		DEM
Enable hole filling		Yes
Enable ghosting filter		No
Processing time	041	2 mins 03 s
	042	2 mins 15 s
	043	1 mins 46 s
	044	1 mins 28 s
	045	2 mins 07 s
	046	2 mins 00 s

Table 14 Reconstruction parameters for Orthomosaic.

Figure 22 Image captured on site.

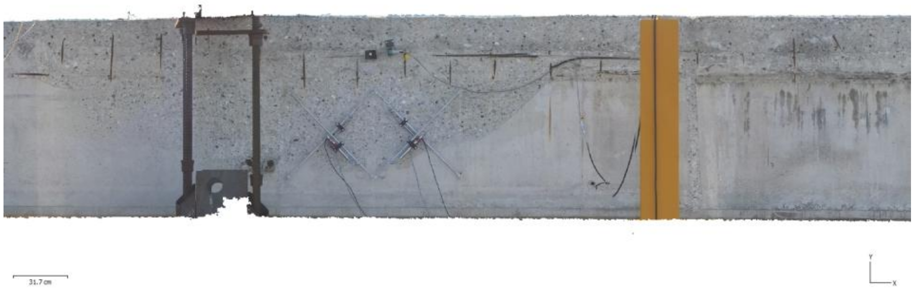

Figure 23 Orthomosaic without modification.

Figure 24 Orthomosaic with modification.

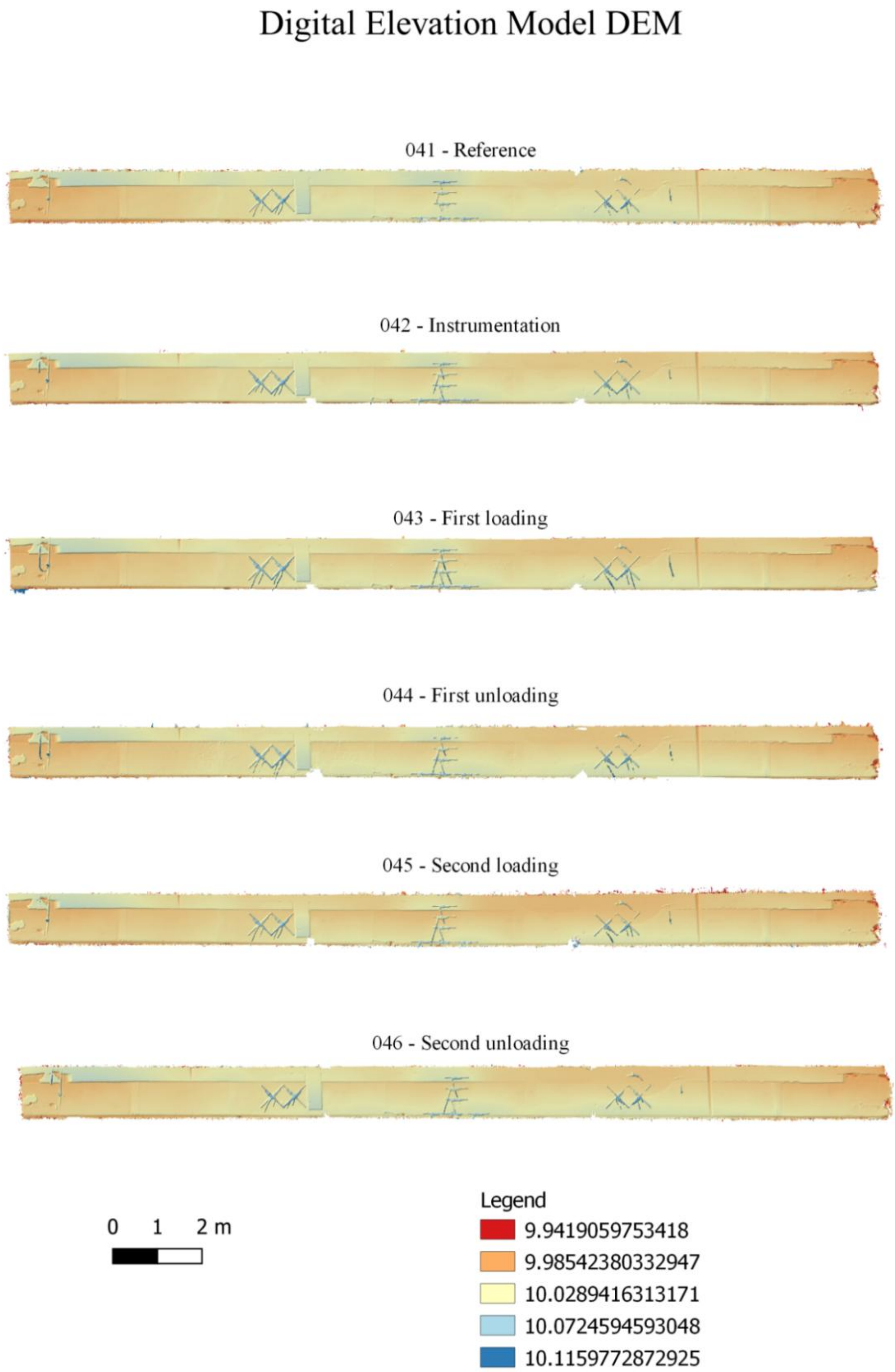

Figure 25 DEM of the loading surface of box girder.

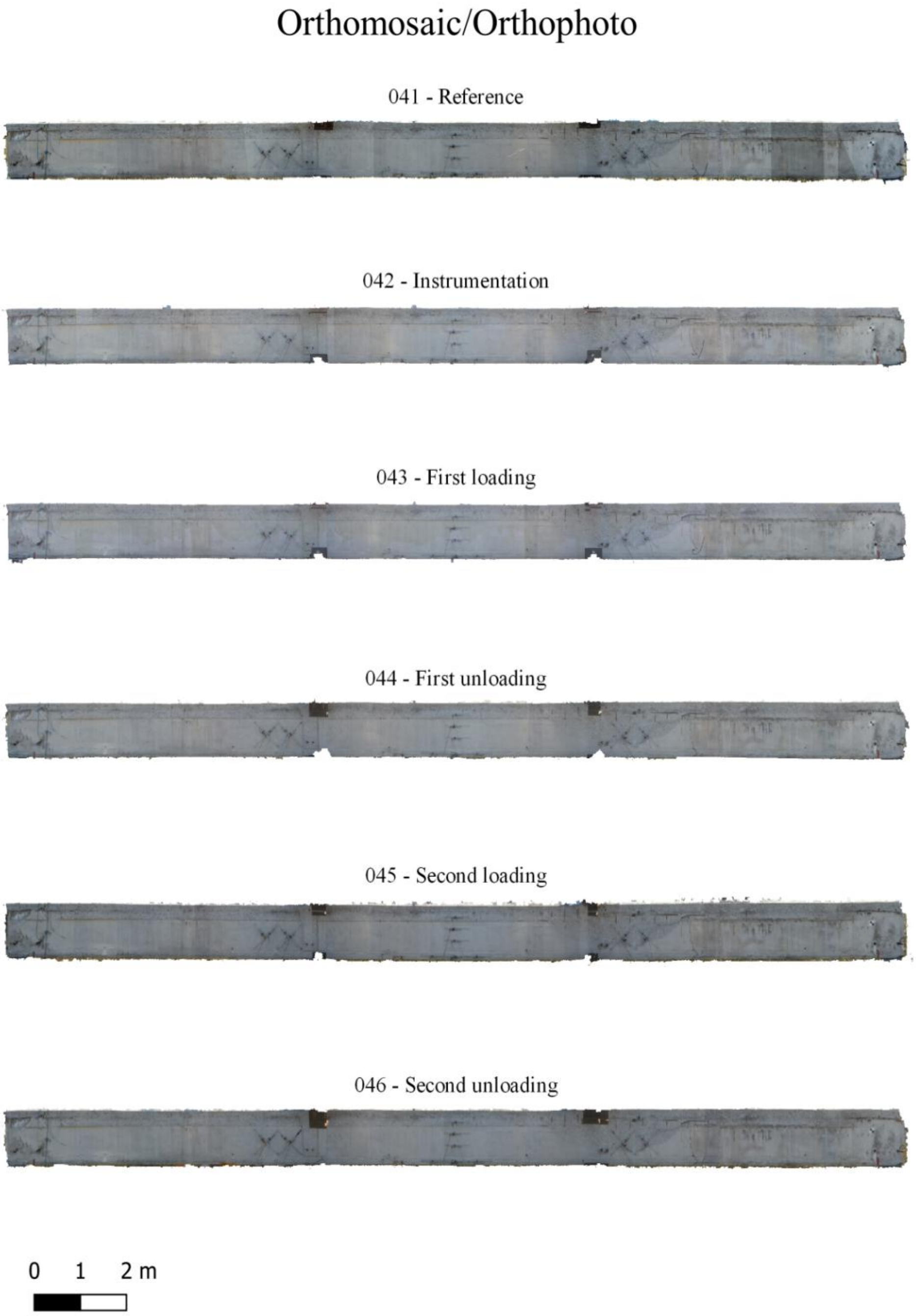

Figure 26 Orthophoto of the loading surface of box girder.

4.4 Export of results

When exporting photogrammetric results from Metashape, make sure to select the appropriate export formats and settings based on the specific requirements of the project and the compatibility with the software or systems for further analysis or integration.

4.4.1 Export of estimated coordinate

The estimated 3D coordinate of all surface points can be collected, including the center point of the GCPs and of the screws used to fix the aluminum frame where the

LVDTs are equipped.

The estimated coordinate of markers is manifested in Table 9.

4.4.2 Evaluation of model

To assess the accuracy of the reconstruction of model, the estimated coordinates of the markers are exported and compared with the relevant original instrumental coordinate and photogrammetry coordinate in this part.

This can be accomplished by calculating the 3D-plane distance between various and random pairs of marker points in different phases with formula (8), and then compare the obtained results within 2 different reference system. To have a fully systematic check, 8 random pairs of point distance are computed, which are spread over the girder surface.

The 3D-plane distance calculated within instrumental and photogrammetry reference system is shown as follows in Table 15 and 16, while the distance based on the estimated coordinate data is indicated in Table 17. The absolute variation between the photogrammetry value and estimated value is posted in Table 18. The parameters in the shaded area are missing data due to technical reasons.

	Points Pair	1-2	1-8	2-4	2-7	3-5	3-6	4-7	6-8
Original 3D-plane distance [m]	041 Original	1.9512	17.6371	5.2883		6.4294	10.8685		2.8998
	042 Instrumentation	1.9521	17.6370	5.2881	15.1720	6.4298	10.8688	9.8931	2.8992
	043 1st loading	1.9506	17.6336	5.2869	15.1720			9.8927	
	044 1st unloading							9.8917	2.8993
	045 2nd loading		17.6342						2.8987
	046 2nd unloading	1.9536	17.6394	5.2883	15.1725	6.4297	10.8687	9.8930	2.8991

Table 15 3D-plane point distance on instrumental coordinate.

	Points Pair	1-2	1-8	2-4	2-7	3-5	3-6	4-7	6-8
Photogrammetry 3D-plane distance [m]	041 Original	1.9512	17.6371	5.2883		6.4294	10.8685		2.8998
	042 Instrumentation	1.9521	17.6370	5.2881	15.1720	6.4298	10.8688	9.8931	2.8992
	043 1st loading	1.9506	17.6336	5.2869	15.1720			9.8927	
	044 1st unloading							9.8917	2.8993
	045 2nd loading		17.6342						2.8987
	046 2nd unloading	1.9536	17.6394	5.2883	15.1725	6.4297	10.8687	9.8930	2.8991

Table 16 3D-plane point distance on photogrammetry coordinate.

	Points Pair	1-2	1-8	2-4	2-7	3-5	3-6	4-7	6-8
Estimated 3D-plane distance [m]	041 Original	1.9511	17.6372	5.2863	15.1718	6.4294	10.8694	9.8948	2.9004
	042 Instrumentation	1.9505	17.6364	5.2869	15.1724	6.4295	10.8693	9.8947	2.9003
	043 1st loading	1.9502	17.6342	5.2851	15.1717	6.4285	10.8682	9.8944	2.9019
	044 1st unloading	1.9514	17.6350	5.2870	15.1706	6.4291	10.8678	9.8925	2.9019
	045 2nd loading	1.9494	17.6352	5.2861	15.1757	6.4319	10.8725	9.8960	2.9018
	046 2nd unloading	1.9514	17.6377	5.2884	15.1735	6.4307	10.8701	9.8938	2.9000

Table 17 3D-plane point distance on estimated coordinate.

Absolute variation Δ [m]	Points Pair	1-2	1-8	2-4	2-7	3-5	3-6	4-7	6-8
	041 Original	0.0001	0.0001	0.0020		0.0000	0.0008		0.0006
	042 Instrumentation	0.0016	0.0006	0.0011	0.0005	0.0003	0.0005	0.0016	0.0011
	043 1st loading	0.0004	0.0006	0.0017	0.0003			0.0017	
	044 1st unloading							0.0008	0.0025
	045 2nd loading		0.0011						0.0031
	046 2nd unloading	0.0022	0.0016	0.0001	0.0010	0.0010	0.0013	0.0008	0.0009

Table 18 Absolute Variation of point distance.

The complete equivalence of the first two sets of data proves the effectiveness of the coordinate transformation, while there exists absolute variation between photogrammetric 3D-plane distance and estimated 3D-plane distance.

The variation of the distance Δ is within the range of [0.0000,0.0031] with meter as the unit of measurement. The variation is in the acceptable error range, confirming the authenticity of the photogrammetric process and then the following post-processing of data could be continued.

4.4.3 Export of photogrammetric products

We export the DEM and Orthomosaic of the girder in different loading and unloading phases and then introduce them in different software tools to analyze the behavior of girder by appending different projects.

4.4.4 Export of processing reports

According to the exported report, valuable information could be taken advantage of to analyze the process and the results.

From the very beginning of the survey, the physical information of camera, photo and image could be found. Also, Metashape can supply a report on the calibration process and the accuracy of the camera parameters.

Since the GCPs are introduced and the project is georeferenced, the relative information, such as the coordinate system, projection, GCP location and error estimate, could be reported as part of the report.

Metashape often generates processing logs that detail each step taken place during the photogrammetry process. These logs aid to understand what the software did and troubleshoot any issues.

What’s more, a quality report after processing a set of photos. This report provides information about the accuracy and quality of the generated 3D model. It may include statistics on the alignment error, reconstruction error, and other quality metrics.

All processing reports are attached in the Appendix, in the sequence of experimental phases.

4.5 Post-processing of data

In this section, further analysis work is implemented to supply a more intuitive result and critical reflection.

On the one hand, the estimated 3D coordinate of 8 GCPs and 22 sensor points are exported and used to monitor the vertical deflection and strains of the girder through phases. On the other hand, DEMs and Orthomosaics are introduced in QGIS to provide a comprehensive view of the structural element, allowing to identify the potential deformation.

4.5.1 Post-processing of estimated coordinate

This task is also conducted in software Microsoft Excel, focusing on the vertical deflection and strains of the box girder.

The vertical deflection of the box girder is obtained from the relative displacement of 8 GCPs in vertical direction, with project 041 as the reference. The results are displayed in section 5.1, compared with that from transducer-based measuring method. Meanwhile the strains in bending zone and shearing zone are represented by the relative distance between different pairs of sensor points. The same calculation principle for 3D-distance in section 3.3.1 is applied again.

To confirm the accuracy of UAV photogrammetry in the assessment of strains, these values are measured up to the LVDTs' outcomes. The results are presented in section 5.3 and 5.4.

4.5.2 Post-processing of DEM

In QGIS, DEMs in the XY plane for different projects are input and compared with project 041 which stands for the initial condition.

With the application of the tool called "*Raster calculator*", where DEM041 is set as "*Main input layer*" and the other 5 DEMs are set as "*Additional layers*", formula "*Subtraction -*" is used to calculate the DEM of difference (DoD) in different loading and unloading phases. The difference is represented by a set of "*pseudo-color*". To have a better visualization, the distribution of color band is adjusted to be "discrete" and "*quantify*".

The results stand for the lateral deflection of the box girder due to distortion during the FPBT, discussed in section 5.2.

4.5.3 Post-processing of Orthomosaic

The integration of orthophoto with the DIC results in Ncorr can offer valuable insights into the deformation behavior of materials or structures.

First of all, the images with sufficient resolution and surface features are imported in

Ncorr in the format of PNG. Loading the orthophoto from project "041" as the reference image and orthophotos as current images allows conducting a comparative study throughout stages.

Then the "*Region of interest*" (ROI) is defined. In this case, 3 ROIs are under investigation: one is defined near the mid-span, set for vertical deflection (Figure 27), one is also near the mid-span but with smaller area to avoid potential noise, set for the analysis of bending strains (Figure 28); the last one is within the left shearing zone, in order to perform the analysis of shearing strains (Figure 29).

The DIC parameters are set to define the subset options, including the radius and spacing. Later, the DIC analysis could start, following the selection of a contiguous region to process and of the placement of seeds.

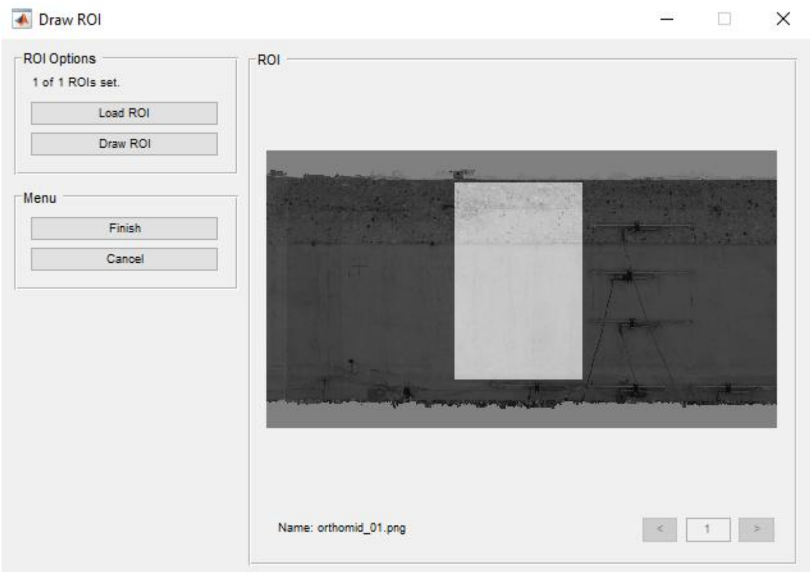

Figure 27 ROI in mid-span for analysis of vertical deflection.

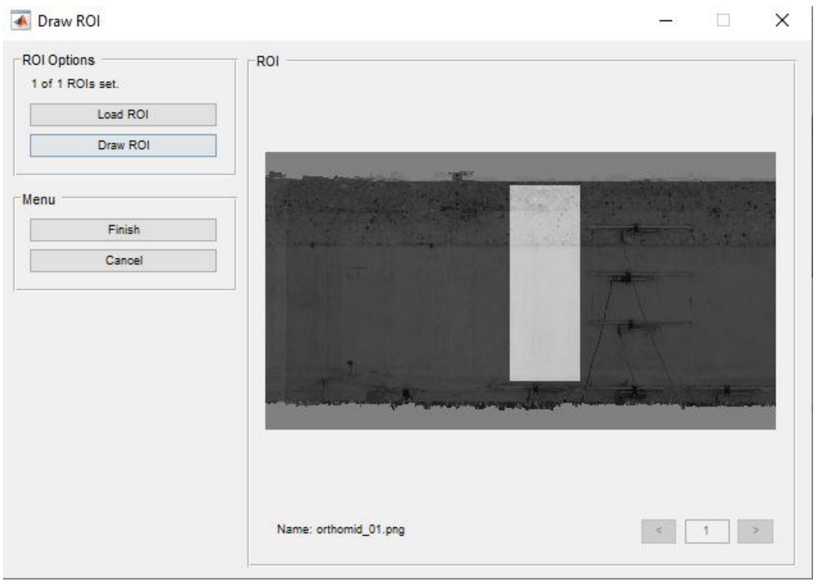

Figure 28 ROI in mid-span for analysis of bending strain.

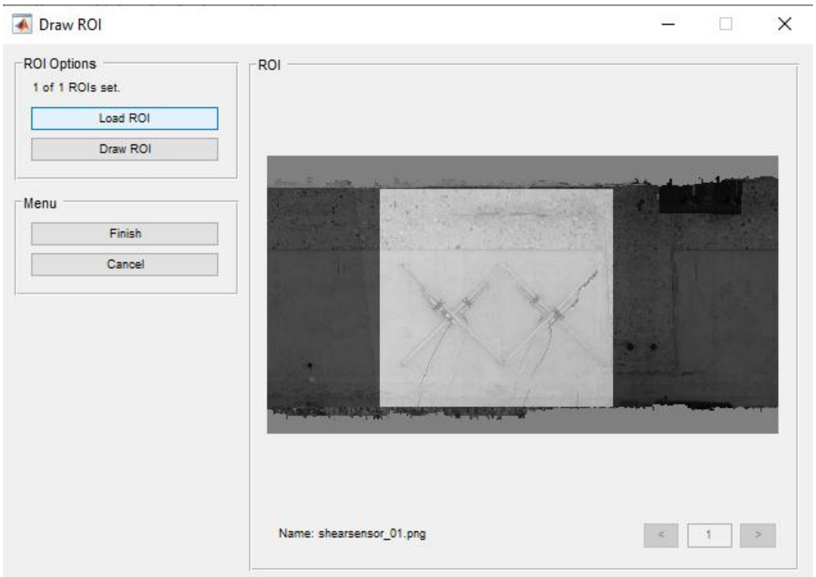

Figure 29 ROI in left span for analysis of shearing strain.

Finally, the displacement and strain analysis could be performed easily by going to *Analysis > Format Displacements/ Calculate Strains* in the main Ncorr graphical user interface (GUI). The displacement in horizontal and vertical direction and the strains E_{xx}, E_{xy}, E_{yy} are processed separately.

The results are in elaboration in section 5.

5. Results and Discussions

In the present research, the most representative outcomes of the structural response are presented and discussed. All be comparison assumes that the transducer-based measurement describes a more precise structural behavior.

5.1 Vertical deflection

Vertical deflection of the whole beam is of greatest interest, which reflects the acceptable limits of the structural deformation, as excessive deflection can indicate structural weakness or potential failure. Measuring and controlling vertical deflection is therefore crucial in the design and construction of such structures to guarantee their safety and stability.

In this study, the vertical deflection of girder during the experimental test is measured both by 9 potentiometer transducers connected to the bottom of the girders continuously and 8 GCPs in girder surface through UAV photogrammetry technique, shown in Figure 30. The transducer-measured deflection curves are delivered in dashed lines while the photogrammetry-measured ones are in solid lines.

Clearly these both two sets of curves are parabolic and reach the maximum displacement near the mid-span position. In addition to this, the corresponding curves of these two sets in the same stages exhibit analogous consequences.

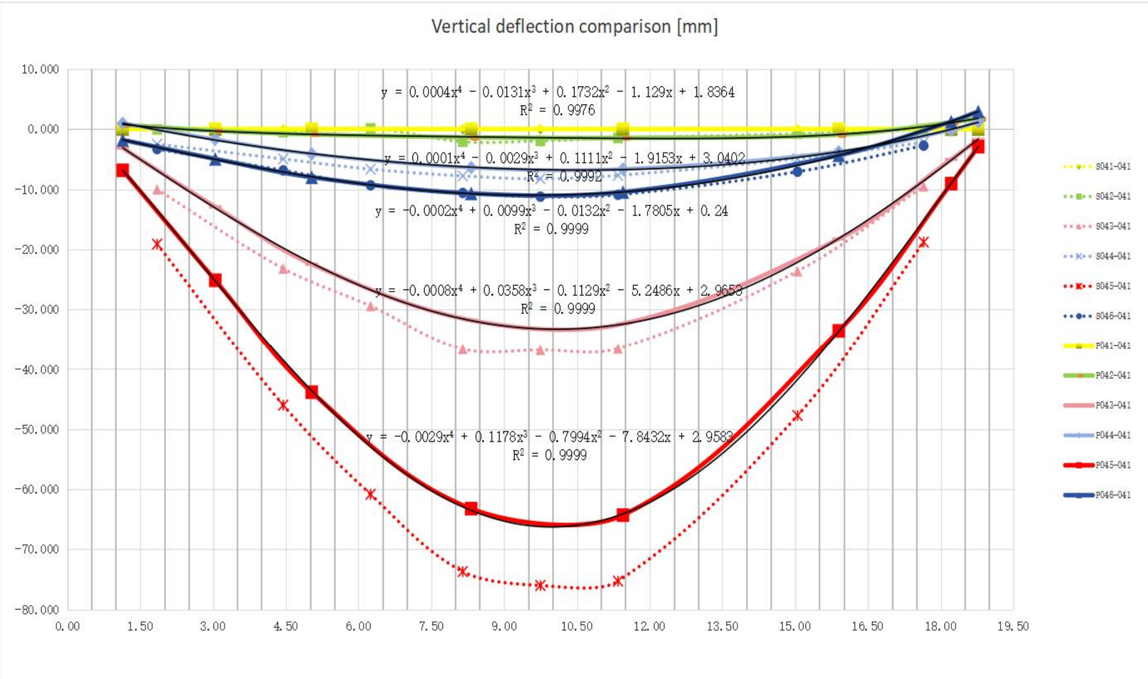

Figure 30 Comparison of deflection curves.

However, considering the transducers and the GCPs are not matched in the position along the girder, it’s impossible to compare the measured vertical deformation in the same section. In this case, it would be more interesting to compare the vertical displacement measured by these two methods at the same location along the beam axis, as it's assumed the points within the same section share the same movement, shown in Figure 31, where inclination angle, or rotation angle α is regarded as constant.

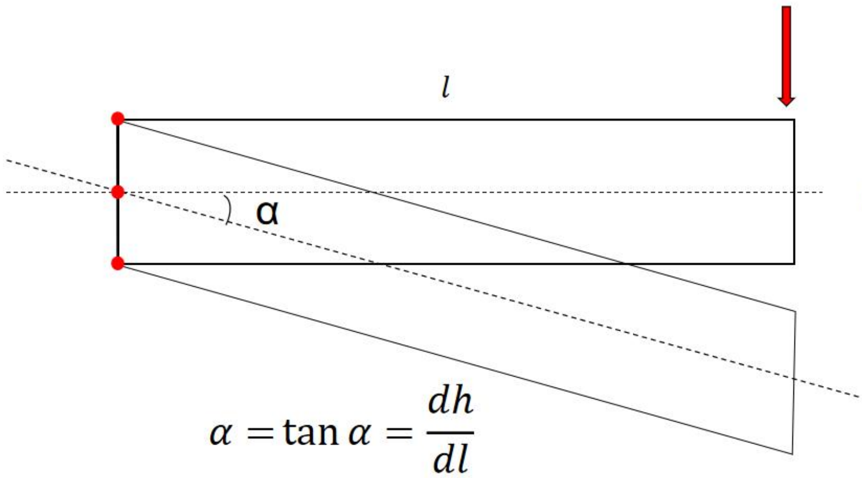

Figure 31 Vertical displacement within same cross-section.

Therefore, to perform a better analysis of the structural behavior in vertical direction, the fitting of deflection curves from photogrammetry technique are necessary as its measurement range is greater than that of transducer. The fitting of curves is detailed in Table 19, where the goodness of fit R^2, also known as coefficients of determination, are all approached to 1.

$$\mathrm{R}^2 = 1 - \frac{\mathrm{SS_{res}}}{\mathrm{SS_{tot}}} \tag{14}$$

where:

SS_{res} is the sum of residuals' square, also called the residual sum of squares.

$SS_{res} = \sum_i (y_i - f_i)^2 = \sum_i e_i{}^2$.

y_i is the element of the data set (or observed data) and f_i is the predicated value.

$SS_{tot} \sum_i (y_i - \bar{y})^2$.

$\bar{y} = \frac{1}{n}\sum_{i=1}^{n} y_i$ is the mean value of the observed data.

Stages	Fitting curves	R^2
042-041	$y = 0.0004x^4 - 0.0131x^3 + 0.1732x^2 - 1.129x + 1.8364$	0.9976
043-041	$y = -0.0008x^4 + 0.0358x^3 - 0.1129x^2 - 5.2486x + 2.9653$	0.9999
044-041	$y = 0.0001x^4 - 0.0029x^3 + 0.1111x^2 - 1.9153x + 3.0402$	0.9992
045-041	$y = -0.0029x^4 + 0.1178x^3 - 0.7994x^2 - 7.8432x + 2.9583$	0.9999
046-041	$y = -0.0002x^4 + 0.0099x^3 - 0.0132x^2 - 1.7805x + 0.2400$	0.9999

Table 19 Fitting of deflection curves from photogrammetry.

In the present case, the absolute difference between deflection curves at the same position is computed as shown in Table 20. It's found that the variation is in the range of $[0.032, 10.634]$ with millimeter as the unit of measurement, within the acceptable error range. At the same time, it's realized that the difference is comparatively larger in two loading stages "043" and "045", highlighted as shadow area in Table 20.

$$\text{Variation ratio} = \frac{|\text{transducer measurement} - \text{photogrammetry measurement}|}{\text{transducer measurement}}$$

The absolute variation percentage is calculated as the ratio between absolute variation and transducer-based measurement, shown in Figure 32. Furthermore, it's noted that the closer from interesting point to the mid-span, where happens larger deformation, the lower the variation, always lower than 20%.

From the point of view of authors, besides the problem of physical parameters of resolution of camera, it's mainly because the UAV photogrammetry measurement is not conducted at the exact time of maximum loading and corresponding maximum deformation, leading to overall smaller deflection values than expected.

	Position	041-041	042-041	043-041	044-041	045-041	046-041
absolute variation [mm]	1.85	0.000	0.325	3.120	2.375	5.576	0.289
	4.45	0.000	0.230	3.425	1.478	7.494	0.267
	6.25	0.000	1.142	2.721	1.537	7.913	0.073
	8.15	0.000	0.912	5.190	1.482	10.634	0.032
	9.75	0.000	0.752	3.823	1.425	9.507	0.251
	11.35	0.000	0.309	4.491	0.742	10.380	0.428
	15.05	0.000	0.733	3.036	0.444	4.380	1.042
	17.65	0.000	2.701	3.895	0.180	0.588	2.486

Table 20 Absolute variation of vertical deflection.

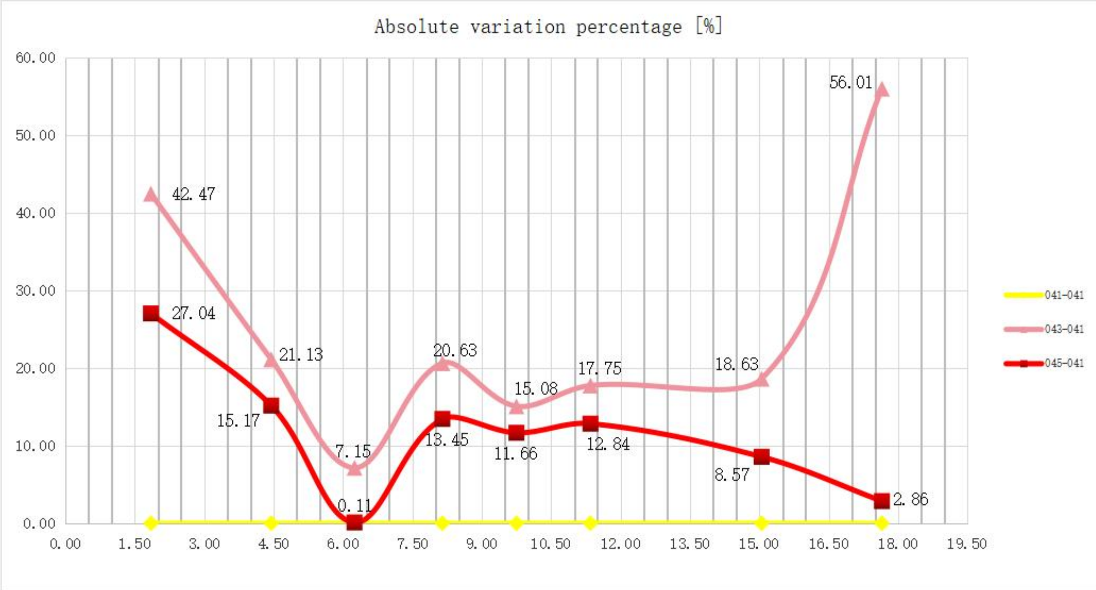

Figure 32 Absolute variation percentage of vertical deflection.

Overall, this proves that the photogrammetry-based measurement provides a reliable survey in the displacement since these measurement techniques show good agreement with each other in vertical deflection, especially in stable phases.

DIC is subsequently included for the purpose of reviewing and assessing the vertical deflection measured at the mid-span by the two previously described techniques. In this matter, the ROI is set to be near the mid-span, around 9.75m from the left side. That is, the main related physical phenomenon discussed as follows is the mid-span vertical deflection. The plots of displacement in vertical direction are presented in Figure 33.

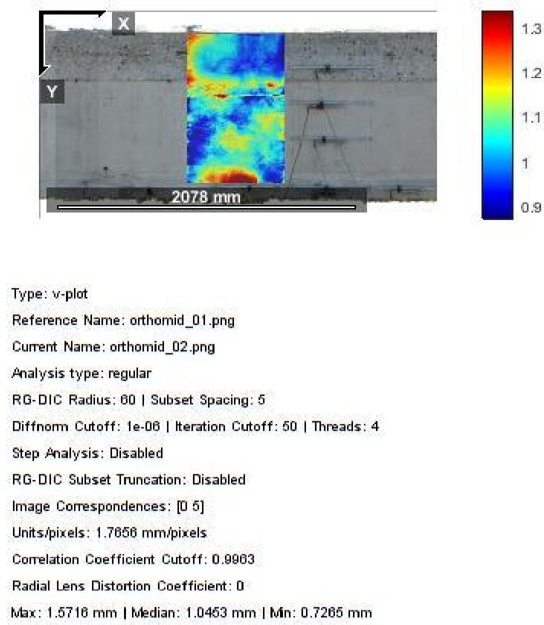

(a)

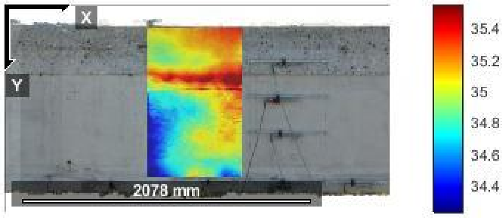

Type: v-plot
Reference Name: orthomid_01.png
Current Name: orthomid_03.png
Analysis type: regular
RG-DIC Radius: 60 | Subset Spacing: 5
Diffnorm Cutoff: 1e-06 | Iteration Cutoff: 50 | Threads: 4
Step Analysis: Disabled
RG-DIC Subset Truncation: Disabled
Image Correspondences: [0 5]
Units/pixels: 1.7656 mm/pixels
Correlation Coefficient Cutoff: 1.0665
Radial Lens Distortion Coefficient: 0
Max: 35.6703 mm | Median: 35.0023 mm | Min: 33.9683 mm

(b)

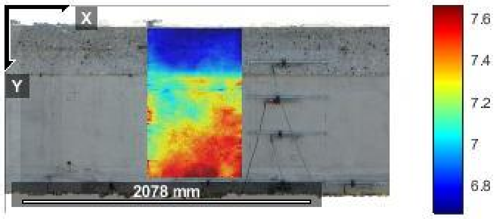

Type: v-plot
Reference Name: orthomid_01.png
Current Name: orthomid_04.png
Analysis type: regular
RG-DIC Radius: 60 | Subset Spacing: 5
Diffnorm Cutoff: 1e-06 | Iteration Cutoff: 50 | Threads: 4
Step Analysis: Disabled
RG-DIC Subset Truncation: Disabled
Image Correspondences: [0 5]
Units/pixels: 1.7656 mm/pixels
Correlation Coefficient Cutoff: 0.9606
Radial Lens Distortion Coefficient: 0
Max: 7.9312 mm | Median: 7.2066 mm | Min: 6.5888 mm

(c)

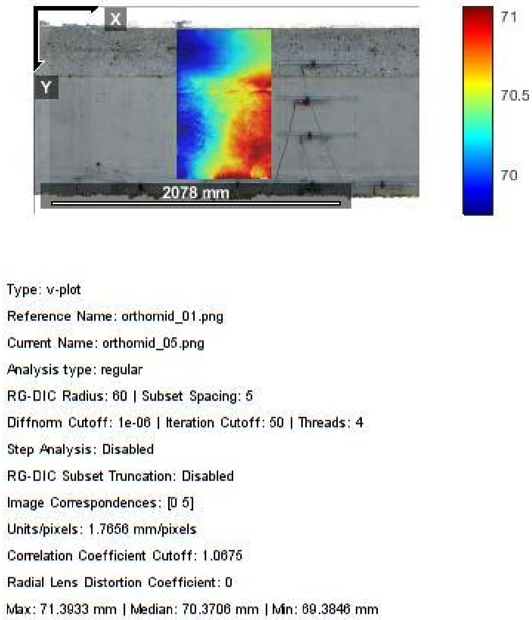

(d)

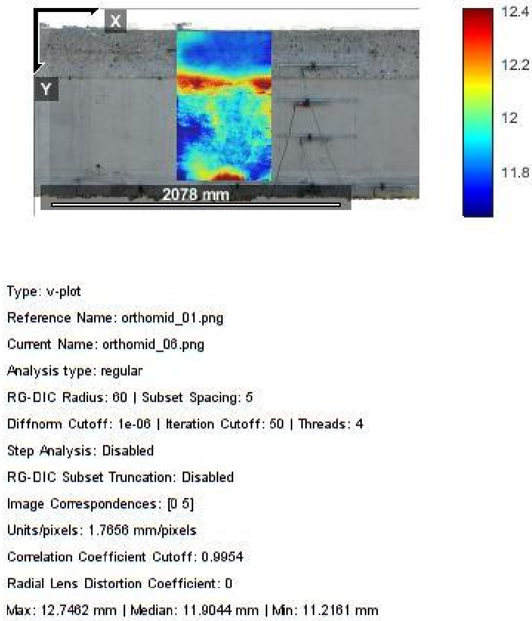

(e)

Figure 33 Vertical displacement of different stages in mid-span

(a)042; (b)043; (c)044; (d)045; (e)046.

It deserves great attention that the pattern of vertical displacement change calculated by DIC technology is consistent with the conclusions we have drawn before, which means the larger deformation does appear with the maximum loading and it puts forward a very resembling degree with that of mentioned findings, just several millimeters in difference.

The comparison of the vertical displacement at the mid-span measured by 3 methods are elaborated in Table 21:

Vertical displacemnt at loctation = 9.75m [mm]	Measuring Method	Experimental stages					
		041	042	043	044	045	046
	Transducer	0.000	-1.985	-36.812	-8.282	-76.036	-11.257
	Photogrammetry	0.000	-1.234	-32.989	-6.857	-66.529	-11.006
	DIC	0.000	-1.045	-35.002	-7.207	-70.371	-11.904

Table 21 Vertical displacement at mid-span.

It's found that the result offered by DIC is within the upper range of "photogrammetry result" and the lower range of "transducer result", which could be described as "conservative but persuasive" in some cases. A more evident expression is provided in Figure 34.

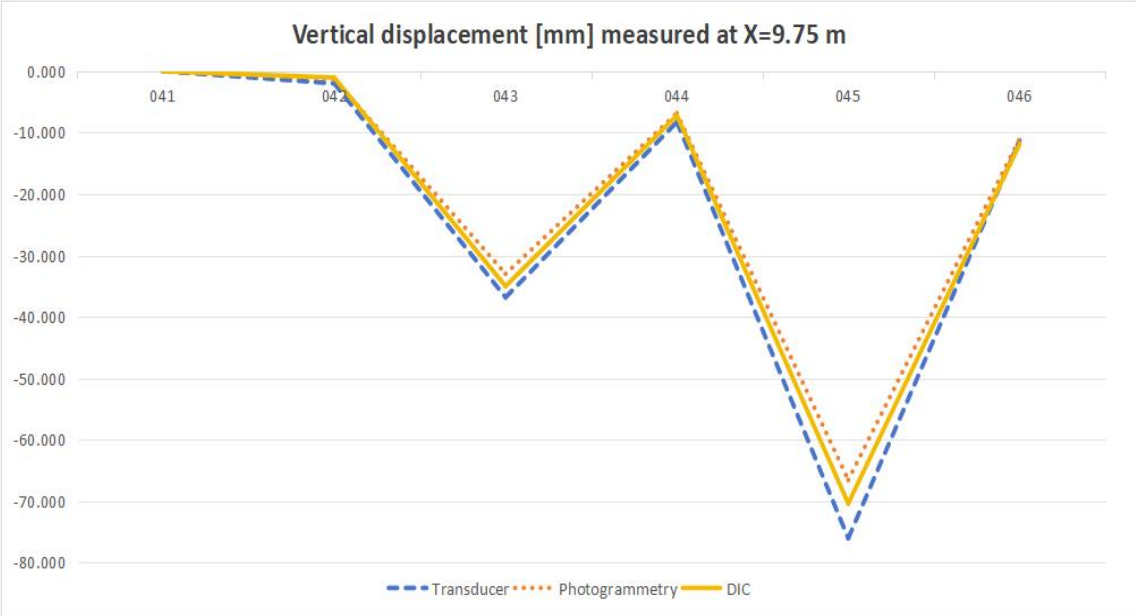

Figure 34 Vertical displacement at mid-span.

If the assessment results are evaluated with the transducer-based parameters, the analysis could be deepened with the variation percentage, delivered in Table 22 and Figure 35.

Absolute variation percentage [%]	Measuring Method	Experimental stages					
		041	042	043	044	045	046
	Transducer	0.000	0.000	0.000	0.000	0.000	0.000
	Photogrammetry	0.000	37.861	10.385	17.205	12.503	2.226
	DIC	0.000	47.347	4.916	12.981	7.450	5.754

Table 22 Absolute variation percentage at mid-span.

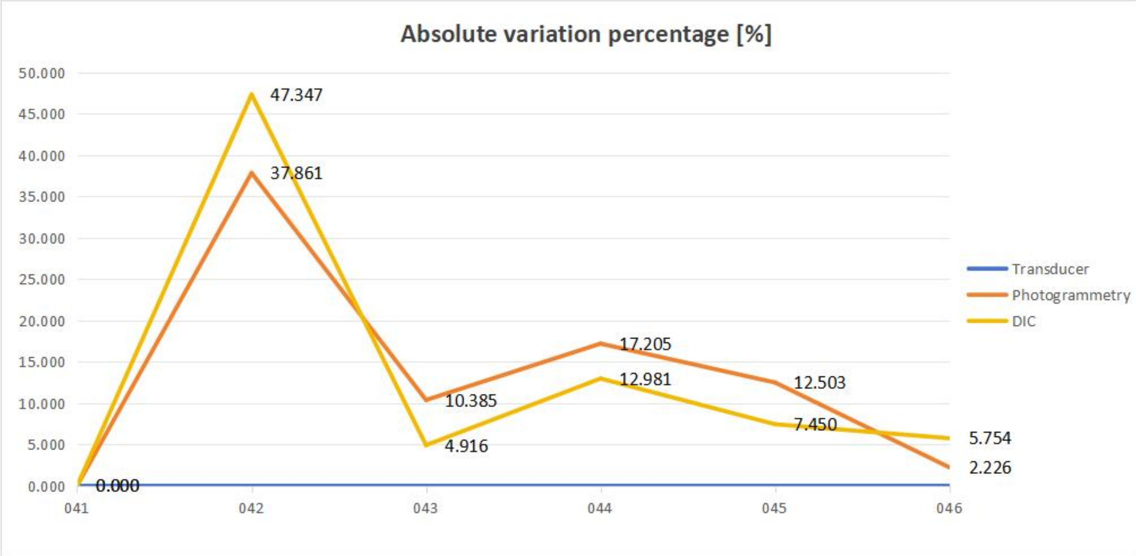

Figure 35 Absolute variation percentage at mid-span.

First and foremost, DIC tends to supply with more assembling outcomes with the transducer-based value when compared to photogrammetry. It deserves extra attention about the location of ROI, which is not at the exact mid-span, but about 0.25m away from. This means the displacement calculated by DIC at mid-span should be larger than the value discussed here, leading to an assessment with an even lower error percentage. Additionally, it appears that the variation is significant in the second stages ("Instrumentation"), up to almost 50%. However, the variation at other experimental phases is comparatively lower, within 20%, especially for two loading stages ("043" and "045") where the large deformation shows up.

5.2 Lateral deflection

Lateral deflection refers to the sideways movement perpendicular to the vertical load. It typically becomes more prominent when the load is applied off-center along the length of the girder. The lateral deflection of the beam at the mid-span is a critical parameter to evaluate the behavior of the beam under the applied load.

In this FPBT, two external forces are always assumed to be equal and form the applied force together. Under this circumstance, the lateral deflection is mainly caused by the bending moment and has nothing to do with torsion. According to the study from Vizzaccaro, A., the great loading induces bending, resulting in this elastic behavior of material along its length[48]. A more detailed analysis, such as finite element analysis or numerical methods, can be developed to obtain a more accurate predictions of lateral deflection with specific parameters related to geometry, material and loading configuration (shown in Figure 36).

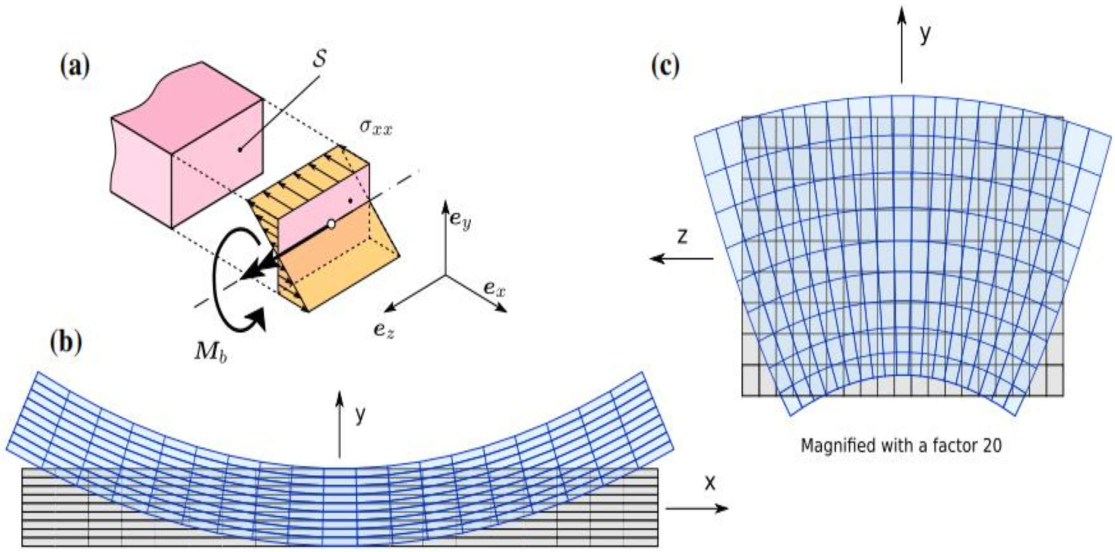

Figure 36 Analytical solution of a beam in pure bending

(a) Stress state σ_{xx} in a cross-section S; (b, c) reference (in grey) and deformed (in blue) configurations of the beam. The Poisson effect has been magnified with a factor 20 in the cross-section view (c).

In QGIS, this lateral deflection is identified with the analysis of DEMs. The DEM of difference of the girder surface, refers to DoD in the following discussion, is expressed in distinct color, representing the degree of the sideways movement (shown in Figure 37, with m as unit of measurement). The darker the color green, the larger the lateral deflection and vice versa.

It's quite apparent that during the 2 loading phases, the degree of lateral deflection presents an ascending trend, and the range of deformation expands. In the two unloading stages, the lateral movement decreases relatively, but it cannot turn its original reference state as shown in "DoD042_041".

The detection of deformation can supply insights into the distribution of stresses and strains, in addition to the safety, stability and integrity of the beam. In summary, comparing the DEMs of girder surface under different loading and unloading phases provides a wealth of information about the structural performance. This finding is quite useful for the engineer to ensure proper design (e.g., prestressing tendons, stirrups), quality materials and appropriate construction practice.

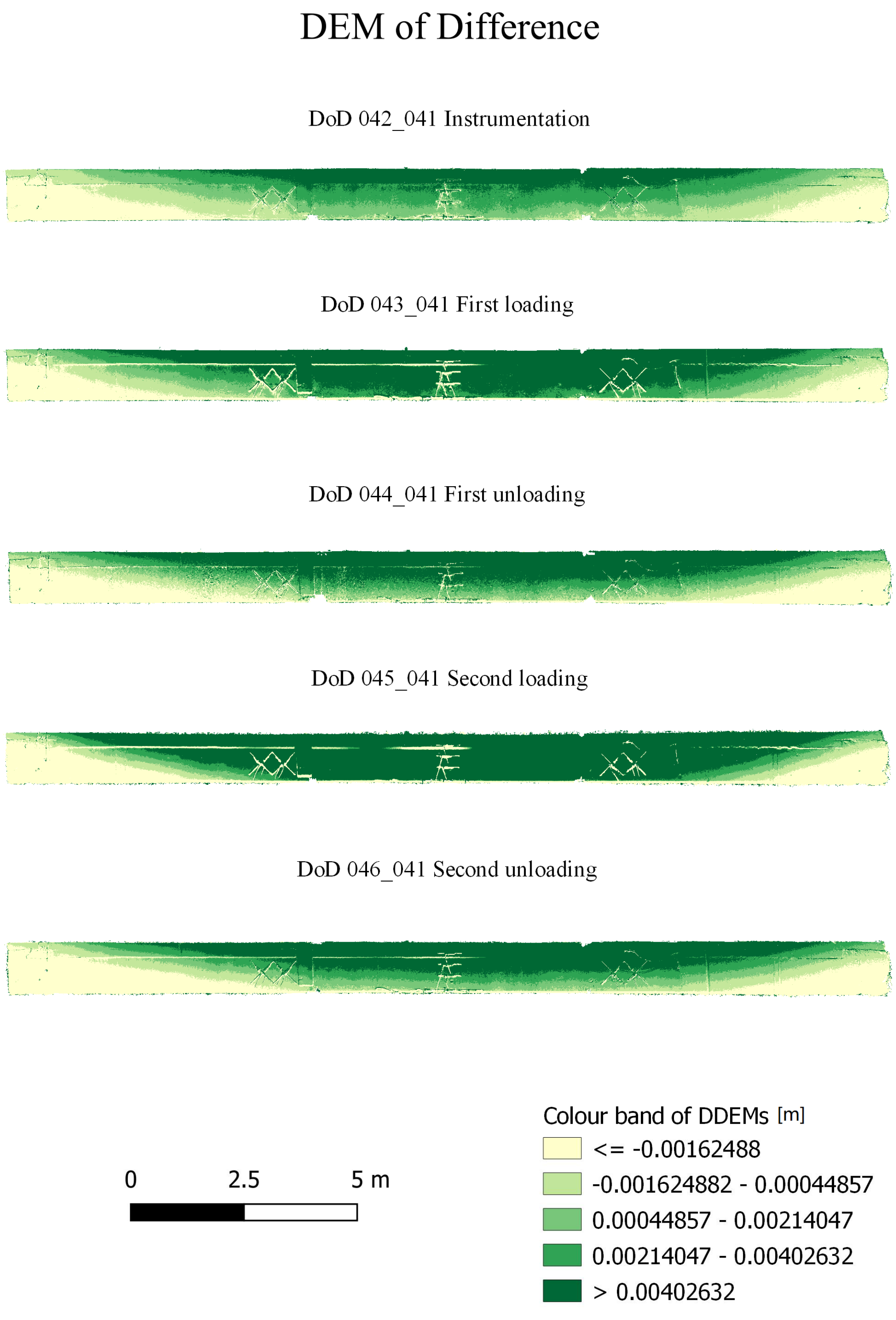

Figure 37 DoDs at different stages.

5.3 Bending strains

In this primary comparison, the bending strains measured from photogrammetry technique is represented by the 3D-plane displacement between the screws' center, which are used to fix the frames and transducers, referring to "data 1" in Figure 38 and Figure 39.

The results are calculated with the initial state "041" as reference and then input to MATLAB directly to compare with the transducer-based outcomes, shown in "blue curves" in Figure 38 and 39.

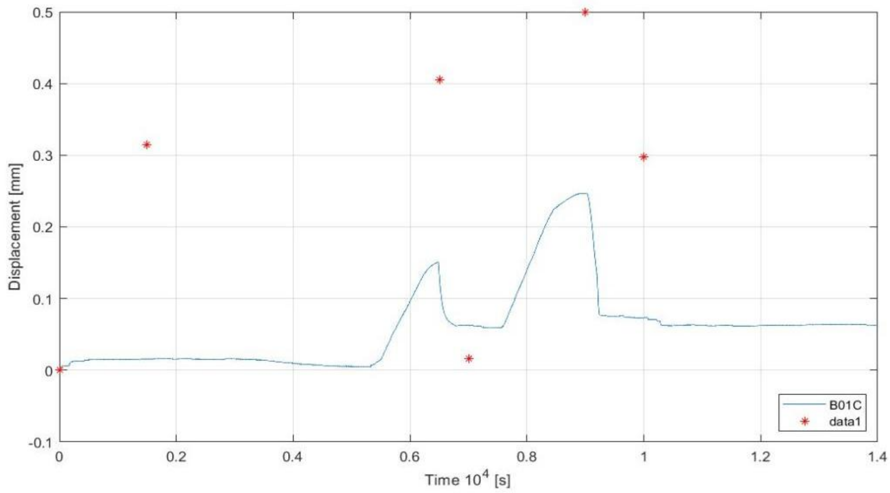

(a)

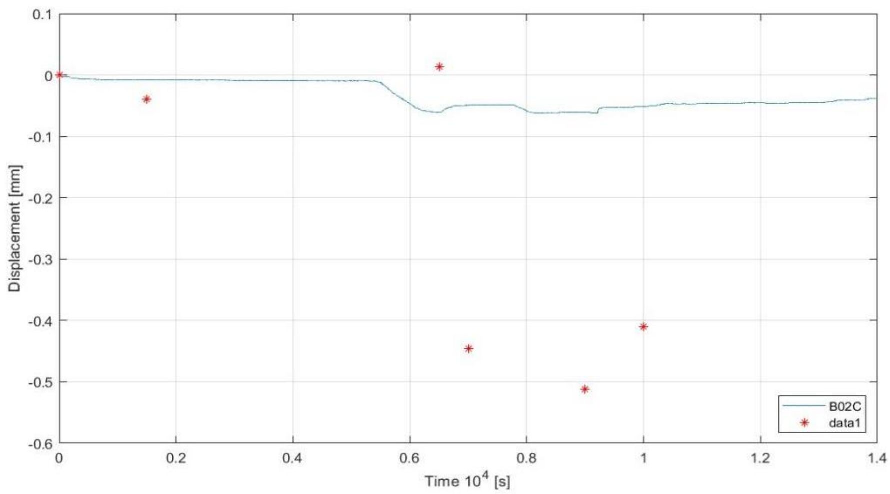

(b)

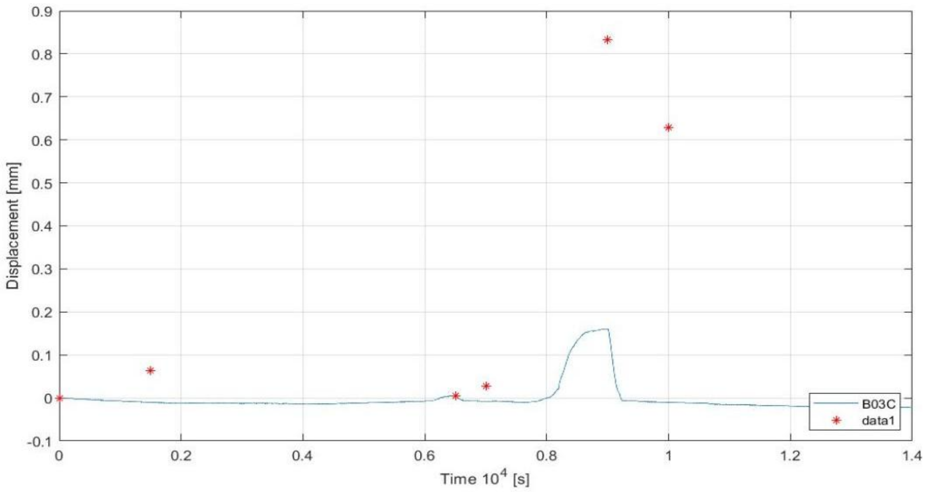

(c)

Figure 38 Comparison of compressive strain in mid-span (a)B01C; (b)B02C; (c)B03C.

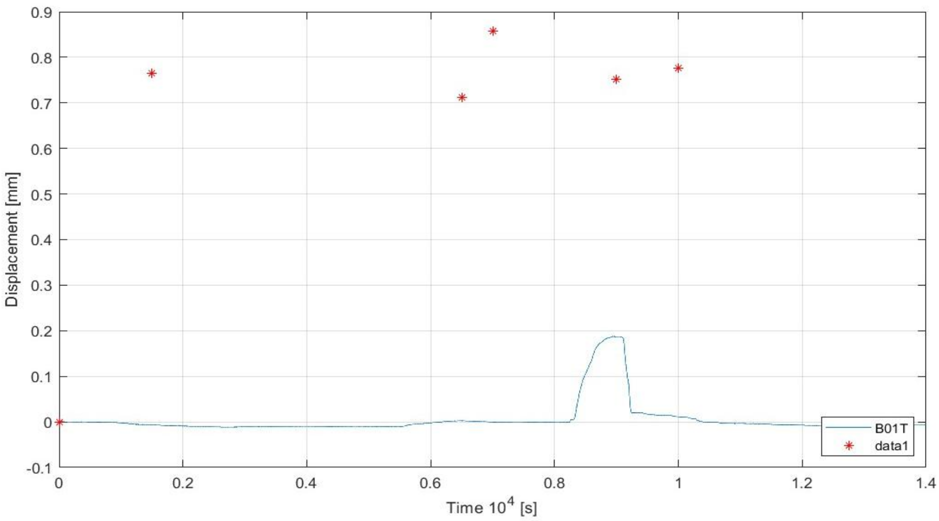

(a)

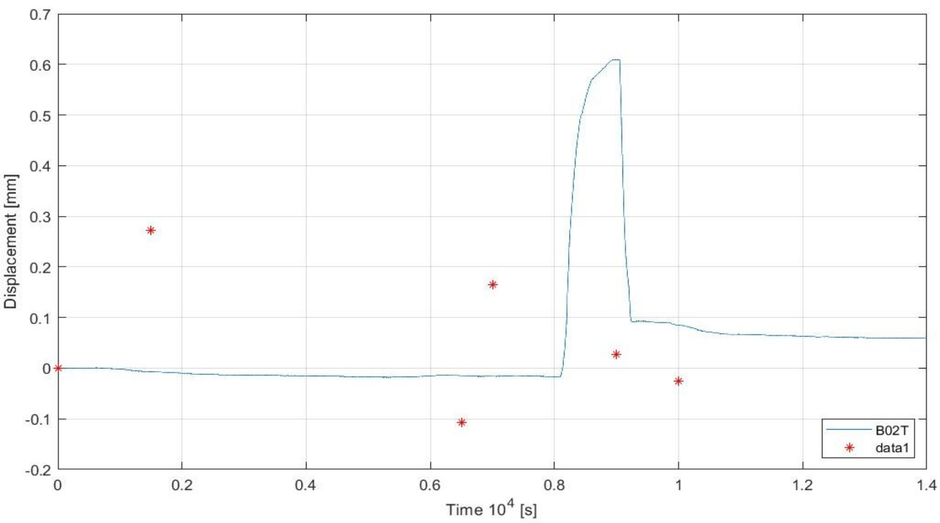

(b)

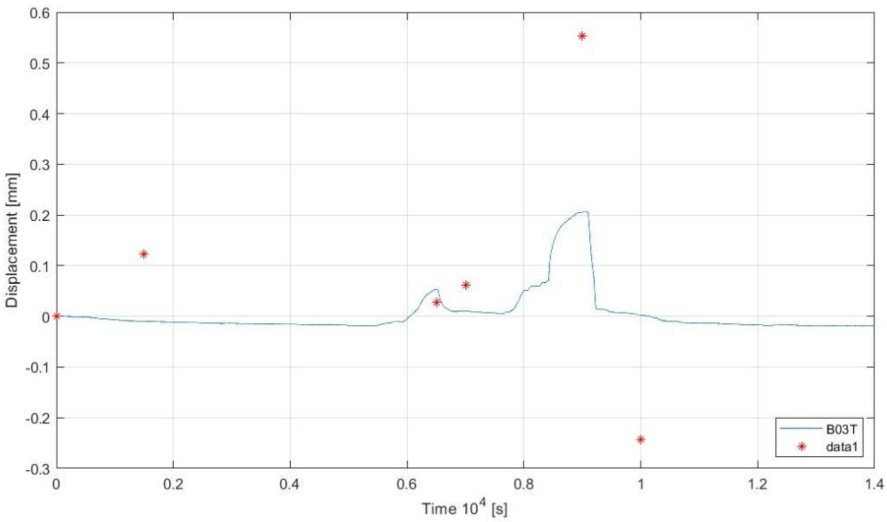

(c)

Figure 39 Comparison of tensile strain in mid-span
(a)B01T; (b)B02T; (c)B03T.

It seems that the photogrammetry-based strains are not perfectly consistent with the transducer-based measurement. However, it should be highlighted that the maximum variation is still within 1 mm and it's acceptable and satisfactory. What's more, it's still able to draw the meaningful trend-line for the strains throughout experimental tests even if there's some considerable noise.

Then it's supposed to proceed with the consideration of DIC here since it's furnished with strain analysis automatically. The plots of horizontal strain E_{xx} are presented in Figure 40.

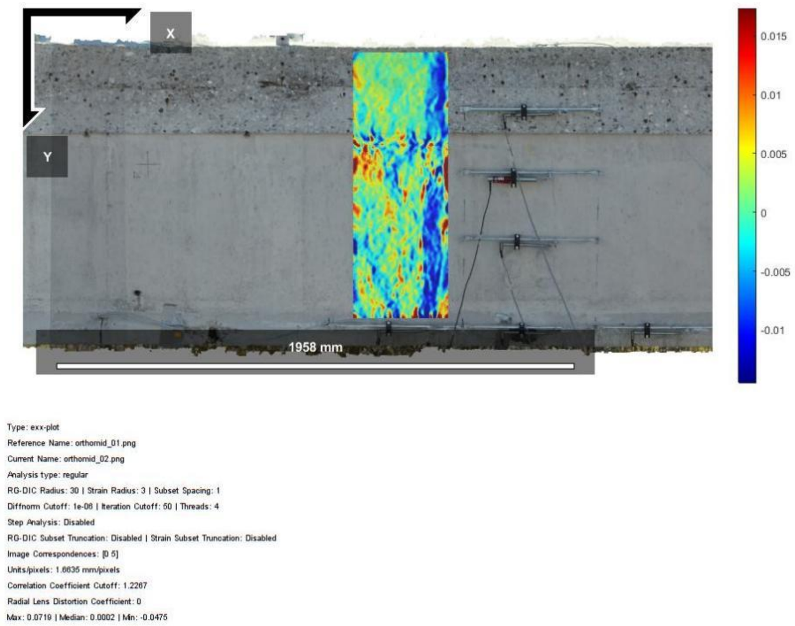

(a)

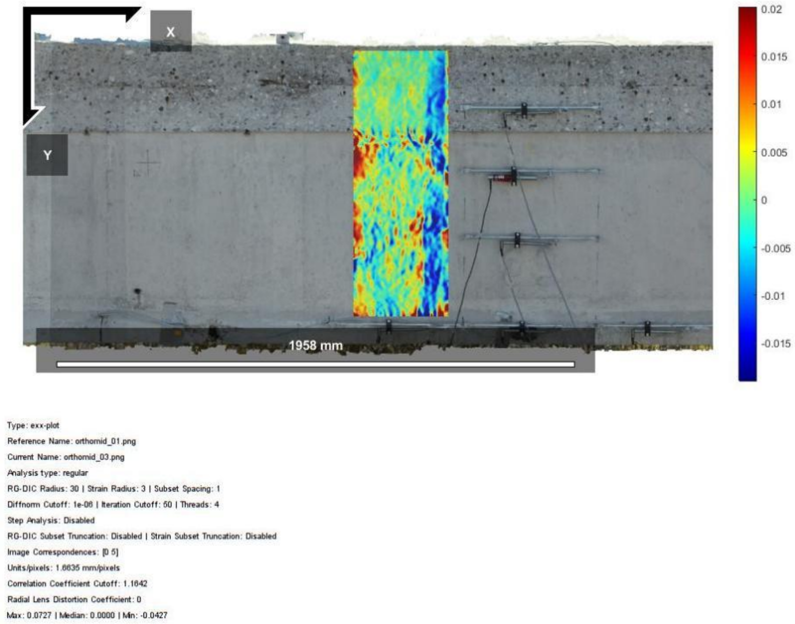
X
Y
1958 mm
0.02
0.015
0.01
0.005
0
-0.005
-0.01
-0.015
Type: exx-plot
Reference Name: orthomid_01.png
Current Name: orthomid_03.png
Analysis type: regular
RG-DIC Radius: 30 | Strain Radius: 3 | Subset Spacing: 1
Diffnorm Cutoff: 1e-06 | Iteration Cutoff: 50 | Threads: 4
Step Analysis: Disabled
RG-DIC Subset Truncation: Disabled | Strain Subset Truncation: Disabled
Image Correspondences: [0 5]
Units/pixels: 1.6635 mm/pixels
Correlation Coefficient Cutoff: 1.1642
Radial Lens Distortion Coefficient: 0
Max: 0.0727 | Median: 0.0000 | Min: -0.0427

(b)

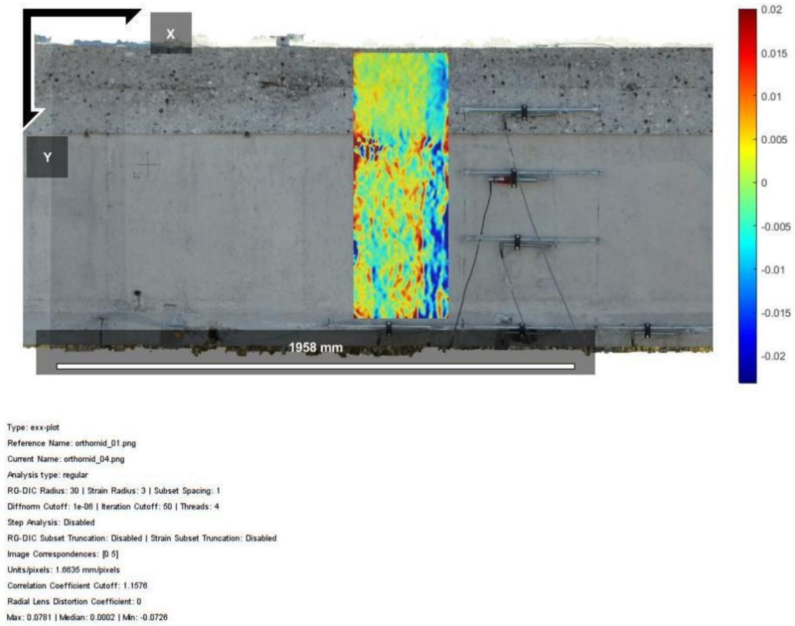
X
Y
1958 mm
0.02
0.015
0.01
0.005
0
-0.005
-0.01
-0.015
-0.02
Type: exx-plot
Reference Name: orthomid_01.png
Current Name: orthomid_04.png
Analysis type: regular
RG-DIC Radius: 30 | Strain Radius: 3 | Subset Spacing: 1
Diffnorm Cutoff: 1e-06 | Iteration Cutoff: 50 | Threads: 4
Step Analysis: Disabled
RG-DIC Subset Truncation: Disabled | Strain Subset Truncation: Disabled
Image Correspondences: [0 5]
Units/pixels: 1.6635 mm/pixels
Correlation Coefficient Cutoff: 1.1576
Radial Lens Distortion Coefficient: 0
Max: 0.0781 | Median: 0.0002 | Min: -0.0726

(c)

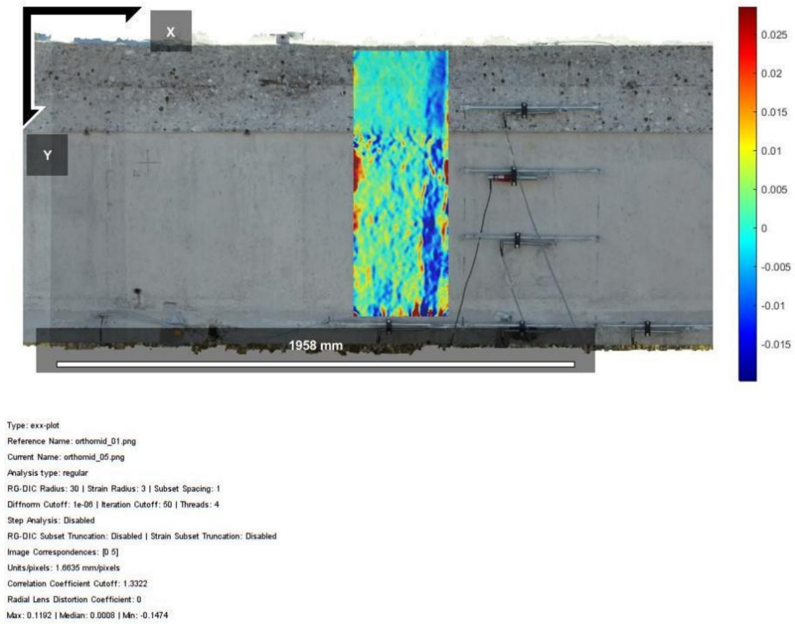

(d)

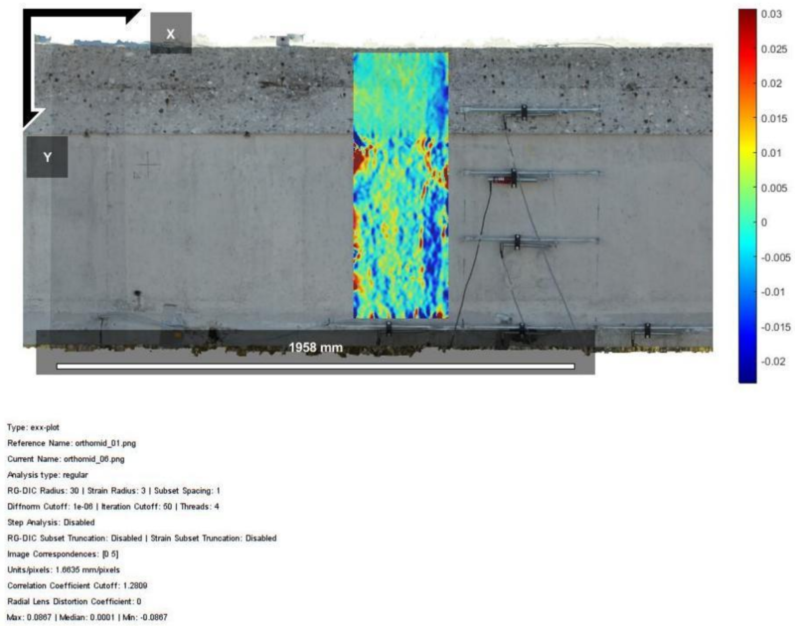

(e)

Figure 40 Horizontal strain E_{xx} of different stages in mid-span

(a)042; (b)043; (c)044; (d)045; (e)046.

The monitoring values provided by transducers are transformed from displacement of screws' center points to strains as:

$$\varepsilon = \frac{\Delta L}{L_0}$$

with unit of measurement as $\varepsilon = [\mathrm{mm/mm}]$.

Since the magnitude of the measured strain is small, the standard practice is to use units of microstrain ($\mu\varepsilon$), which is $[\varepsilon \times 10^{\wedge} - 6]$.

Three compressive LVDTs “B01/02/03C” and the leftmost tensile LVDT “B01T” at the bottom (the closest transducer to the ROI) in 2 loading stages are discussed in this part due to their recognizable measurement.

The strains calculated directly by DIC technology are provided in Figure 41. The displacement and corresponding strain with respect to the aluminum frames is shown in Table 23.

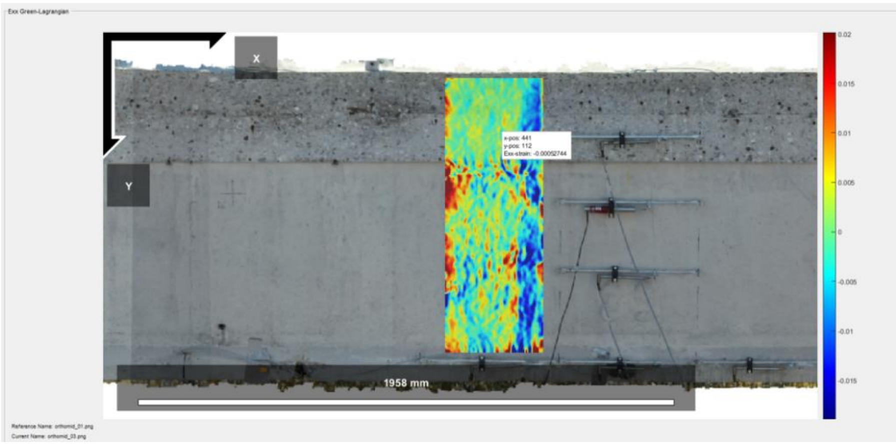

(a) Horizontal strain E_{xx} around B01C at “043”

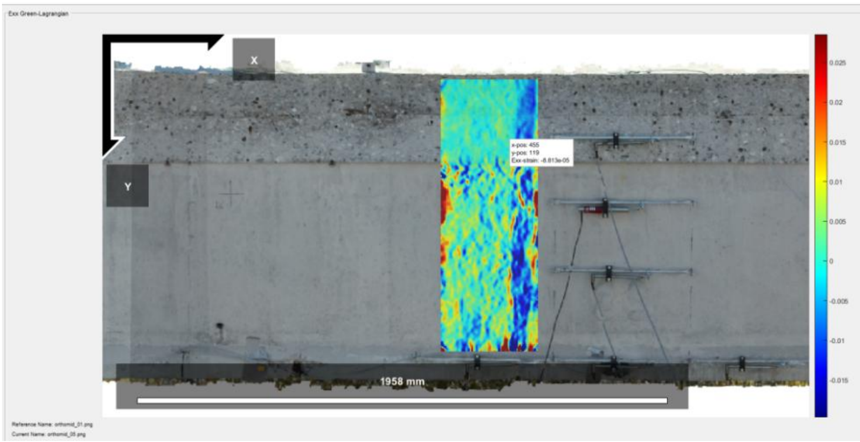

(b) Horizontal strain E_{xx} around B01C at “045”

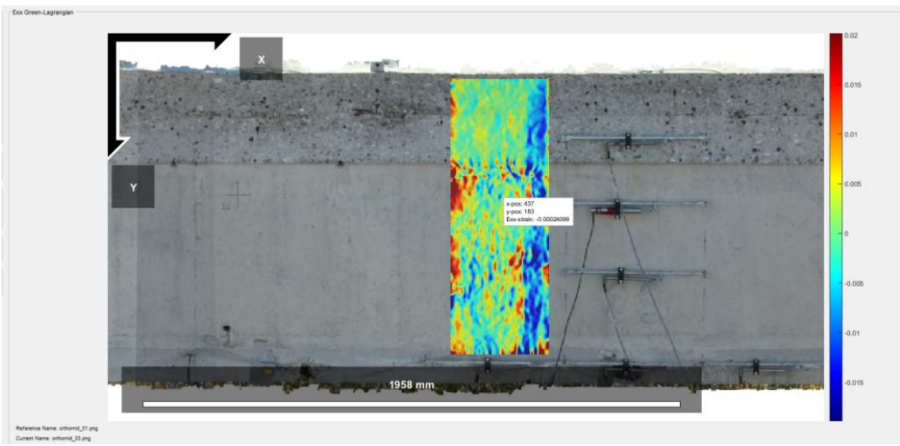

(c) Horizontal strain E_{xx} around B02C at “043”

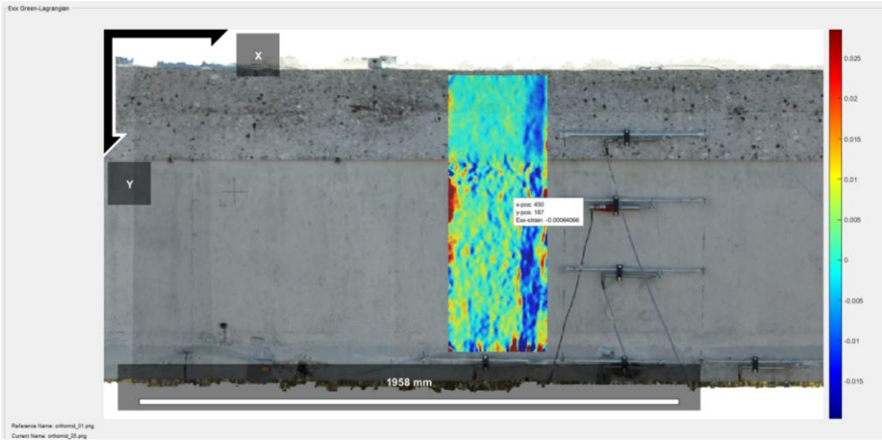

(d) Horizontal strain E_{xx} around B02C at “045”

(e) Horizontal strain E_{xx} around B03C at “043”

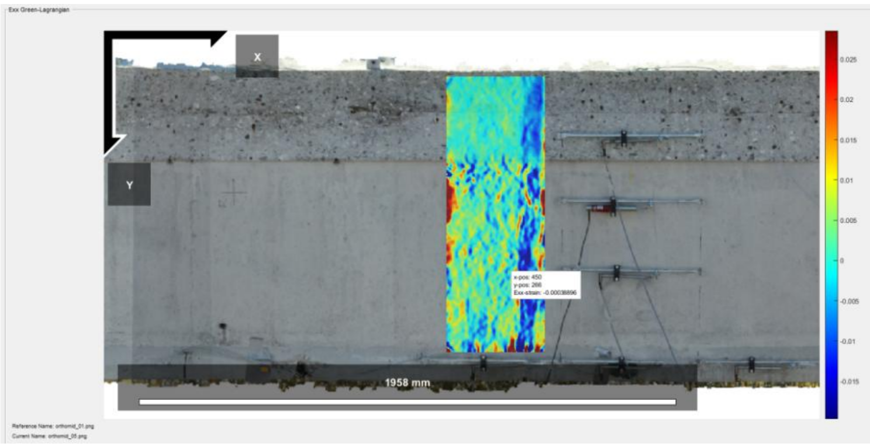

(f) Horizontal strain E_{xx} around B03C at “045”

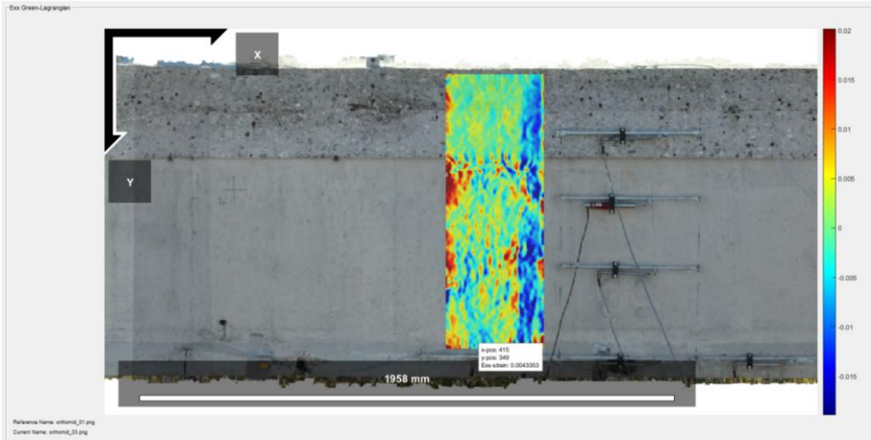

(g) Horizontal strain E_{xx} around B01T at “043”

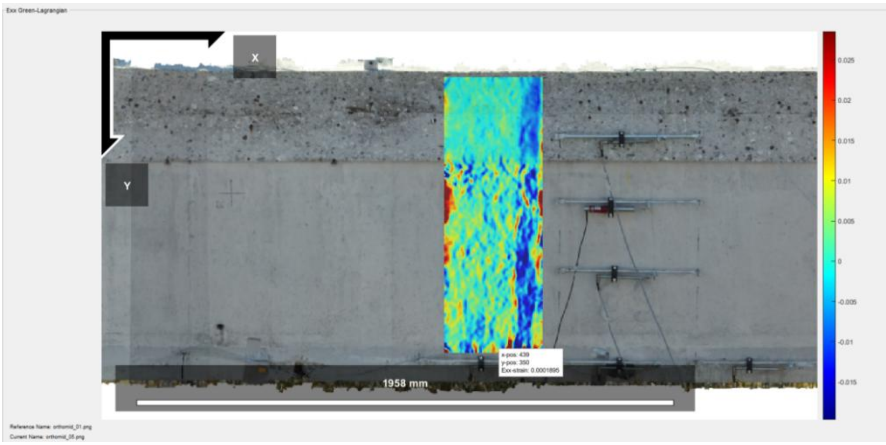

(h) Horizontal strain E_{xx} around B01T at “045”

Figure 41 Horizontal strain E_{xx} of 4 transducers in bending zone.

Transducer measurement	Displacement [mm]		
	Stage	043	045
	B01C	−0.151071	−0.246353
	B02C	−0.061170	−0.062419
	B03C	−0.005490	−0.160341
	B01T	0.002198	0.186786
	L0	500	500

Bending strains	Strain [$\mu\varepsilon$]		
	Stage	043	045
B01C	Transducer	−302.14	−492.71
	DIC	−527.44	−88.13
B02C	Transducer	−122.34	−124.84
	DIC	−240.99	−640.66
B03C	Transducer	−10.98	−320.68
	DIC	−12.92	−3592.20
B01T	Transducer	4.40	373.57
	DIC	4335.30	189.50

Table 23 Comparison of bending strain E_{xx}

From the table, the conclusion can be drawn as the DIC technology achieves a reliable estimation of horizontal strain when evaluated against the transducer-based results, although the magnitude of some values is not at the same level. It could be more meaningful if explained as: strain itself is a kind of parameter of small value, where the reasonable error range of the strain could be relatively large.

To have a further analysis of the bending strain along depth within cross-section, the principles of beam theory can be applied. In bending, the beam experiences both tensile and compressive stresses across its depth, resulting in a distribution of strains. The stress and strain distribution across beam depth is displayed in Figure 42.

Assuming linear elastic behavior (Hooke's Law), the strain ε at any point within the beam can be expressed in terms of the distance from the neutral axis c, where the neutral axis is the axis through which there is no change in length during bending. In the case of a box beam, the neutral axis is generally located at the centroid of the cross-sectional shape, which is likely at the center for a symmetrical box beam. In bending, the top fibers of the beam are in compression, and the bottom fibers are in tension. The neutral axis separates these regions, and its location is influenced by the balance between the magnitudes of tensile and compressive stresses. As the beam deforms under the applied loads, the neutral axis moves continuously along the cross-section to maintain the equilibrium of forces and moments[49].

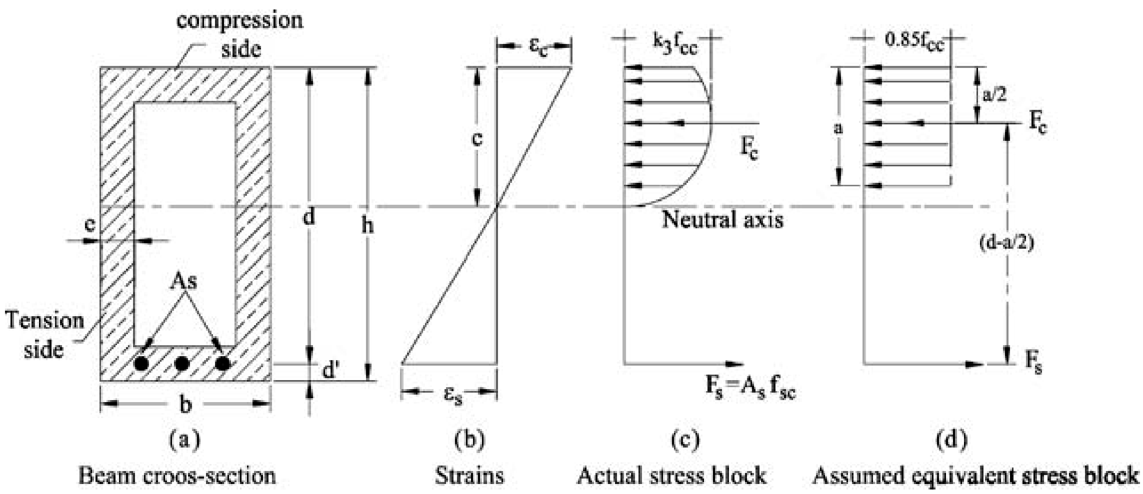

Figure 42 Stress and strain distribution across beam depth.

In this study, a rough approximation of neutral axis is made where there’s presented a sudden transition from compressive strains to tensile strains, shown as the white dashed line in Figure 43. In these two figures, the blue area is under compression while the majority of the red area experiences tensile strains. With the increase of external loading, the location of neutral axis moves upwards lightly.

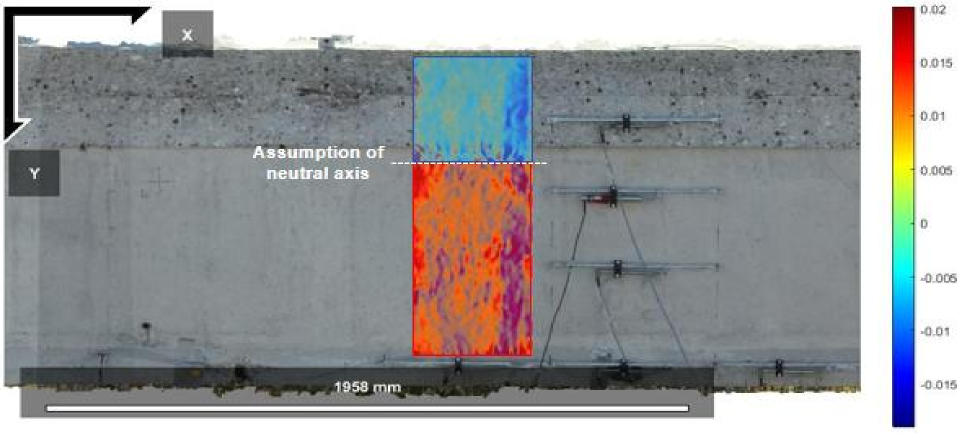

(a)

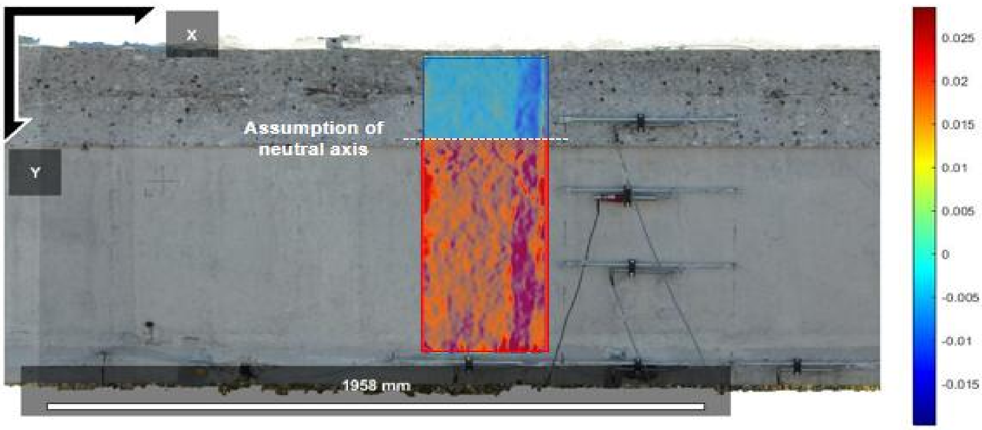

(b)

Figure 43 Division of bending strains with DIC

(a)first loading stage: 043; (b)second loading stage: 045.

DIC technology calculates the bending strains in horizontal direction for each pixel automatically. All these values are extracted and processed to obtain the average value of strain, separately for compressive zone and tensile zone, shown in Figure 44. The computed negative compressive strain is found on the top of the cross-section while the positive tensile strain is on the bottom. The straight dashed line between these two points intersects the ordinate axis, thus deciding the location of the neutral axis.

To evaluate this assumption, the transducer measurement of bending strains is also plotted in the same figure and fitted with a straight trend line (black solid line in Figure 44). In this case, the neutral axis can also be defined in the same principle.

In the first loading stage 043, the definition of neutral axis and the estimation of tensile strain by DIC is in good agreement with the transducer measurement, while the predicted larger compressive strain provides a more conservative warning.

As for the second loading phase 045, the prediction of compressive strain from the two methods seems to be perfectly matched as the two points are almost overlapped completely. However, a large noise takes place in the definition of neutral axis and tensile strain.

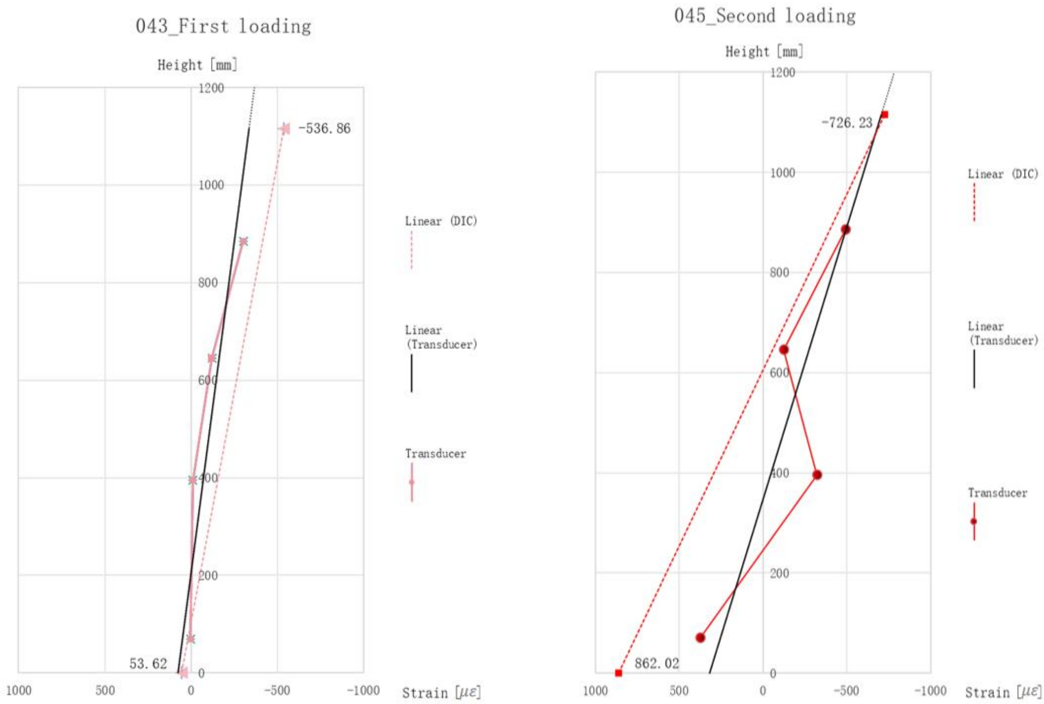

(a) (b)

Figure 44 Bending strain distribution along beam depth

(a)first loading stage: 043; (b)second loading stage: 045.

In summary, these comparable values of bending strains given by DIC technology confirms a fact that there is the potential application in the large-scale experimental test with precise products with the accuracy of the same order of magnitude or even more faithful, but it still deserves more experiments to validate, improve and polish this method.

5.4 Shearing strains

In the investigation of the shearing zones, the comparison is carried out separately: one is between the photogrammetry-based estimated coordinate and LVDT-based measurement (Figure 45); whilst the other is implemented in DIC technique and sensor data (Figure 46).

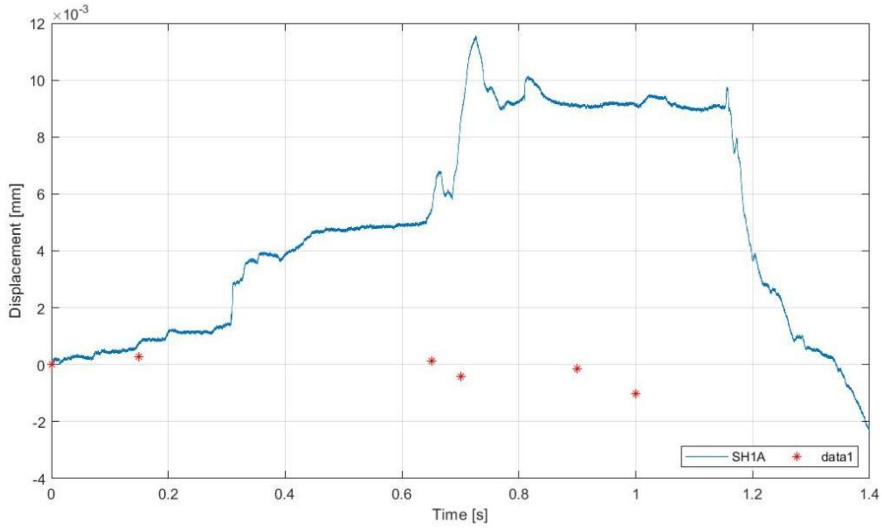
×10^-3
Displacement [mm]
Time [s]
SH1A
data1

(a)

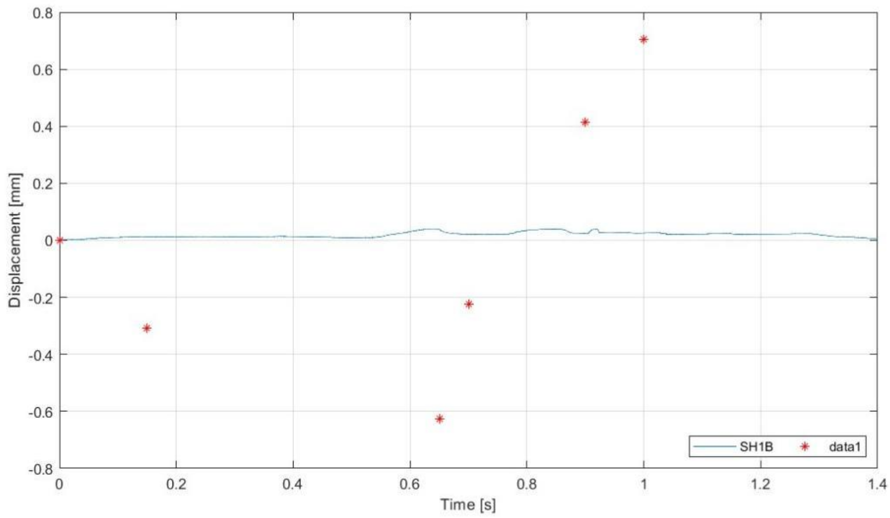
Displacement [mm]
Time [s]
SH1B
data1

(b)

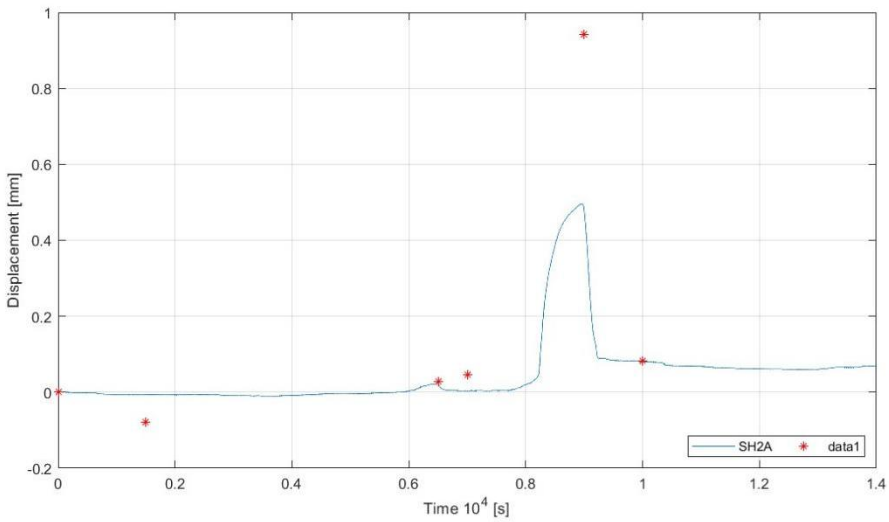
Displacement [mm]
Time 10^4 [s]
SH2A
data1

(c)

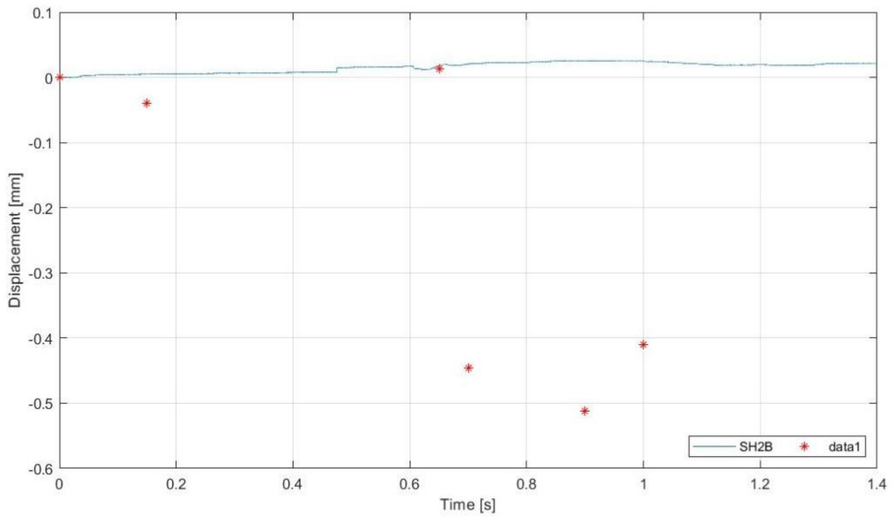

(d)

Figure 45 Comparison of shearing strains

(a)SH1A; (b)SH1B; (c)SH2A; (d)SH2B.

There's no doubt that the gap between the two sets of data still cannot be ignored but the variation is limited to 1 mm or even less.

When it comes to the shearing strains, it will be more meaningful to investigate the strain in the inclined direction. Here are the plots of strain E_{xy} in different experimental tests, obtained with the calculation in DIC, shown in Figure 46.

If we focus the attention on the ROI, it's not difficult to discover there's a strong bond between the layout of the transducers and the detected shearing strains. It provides an intuitive and vivid expression for the qualitative understanding of shearing strain, where around the compressive transducer like "SH1B" and "SH2B" the computed negative strains are mainly blocked with color "blue". On the contrary, near the area of the tensile elements "SH1A" and "SH2A", there was presented an obvious shape in the color "red". This relationship is highlighted with the double-arrow shape in (b) and (d) of Figure 46.

This would be more interesting to predict the global behavior of the beam under loading with the assumption that the layout of shearing sensors covers a larger area of the girder. It paves the way to measure the strains of testing objects without the complex installment of sensors and other monitoring instruments.

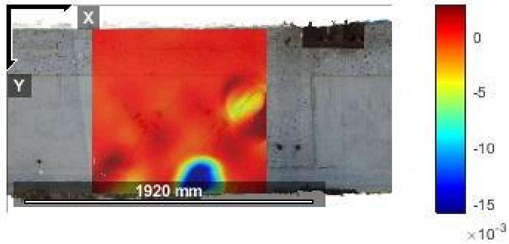

Type: exy-plot
Reference Name: shearsensor_01.png
Current Name: shearsensor_02.png
Analysis type: regular
RG-DIC Radius: 60 | Strain Radius: 15 | Subset Spacing: 5
Diffnorm Cutoff: 1e-06 | Iteration Cutoff: 50 | Threads: 4
Step Analysis: Disabled
RG-DIC Subset Truncation: Disabled | Strain Subset Truncation: Disabled
Image Correspondences: [0 5]
Units/pixels: 1.6307 mm/pixels
Correlation Coefficient Cutoff: 1.8792
Radial Lens Distortion Coefficient: 0
Max: 0.0088 | Median: 0.0001 | Min: -0.0183

(a)

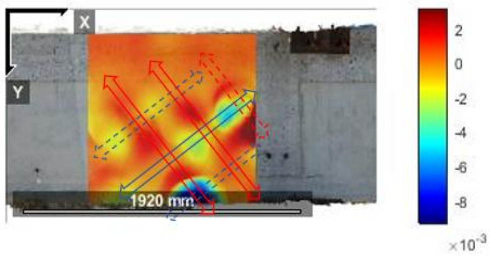

Type: exy-plot
Reference Name: shearsensor_01.png
Current Name: shearsensor_03.png
Analysis type: regular
RG-DIC Radius: 60 | Strain Radius: 15 | Subset Spacing: 5
Diffnorm Cutoff: 1e-06 | Iteration Cutoff: 50 | Threads: 4
Step Analysis: Disabled
RG-DIC Subset Truncation: Disabled | Strain Subset Truncation: Disabled
Image Correspondences: [0 5]
Units/pixels: 1.6307 mm/pixels
Correlation Coefficient Cutoff: 1.9534
Radial Lens Distortion Coefficient: 0
Max: 0.0107 | Median: 0.0002 | Min: -0.0228

(b)

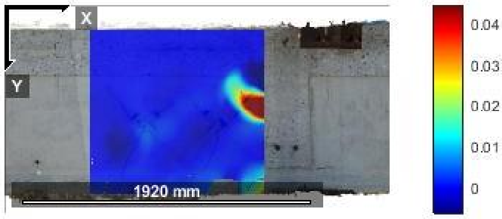
X
Y
1920 mm
0.04
0.03
0.02
0.01
0
Type: exy-plot
Reference Name: shearsensor_01.png
Current Name: shearsensor_04.png
Analysis type: regular
RG-DIC Radius: 60 | Strain Radius: 15 | Subset Spacing: 5
Diffnorm Cutoff: 1e-06 | Iteration Cutoff: 50 | Threads: 4
Step Analysis: Disabled
RG-DIC Subset Truncation: Disabled | Strain Subset Truncation: Disabled
Image Correspondences: [0 5]
Units/pixels: 1.6307 mm/pixels
Correlation Coefficient Cutoff: 1.9989
Radial Lens Distortion Coefficient: 0
Max: 0.0971 | Median: 0.0003 | Min: -0.0395

(c)

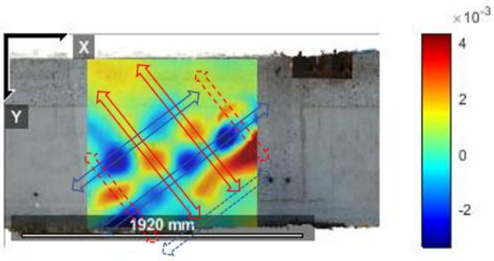
X
Y
1920 mm
$\times 10^{-3}$
4
2
0
-2
Type: exy-plot
Reference Name: shearsensor_01.png
Current Name: shearsensor_05.png
Analysis type: regular
RG-DIC Radius: 60 | Strain Radius: 15 | Subset Spacing: 5
Diffnorm Cutoff: 1e-06 | Iteration Cutoff: 50 | Threads: 4
Step Analysis: Disabled
RG-DIC Subset Truncation: Disabled | Strain Subset Truncation: Disabled
Image Correspondences: [0 5]
Units/pixels: 1.6307 mm/pixels
Correlation Coefficient Cutoff: 1.4801
Radial Lens Distortion Coefficient: 0
Max: 0.0110 | Median: 0.0006 | Min: -0.0045

(d)

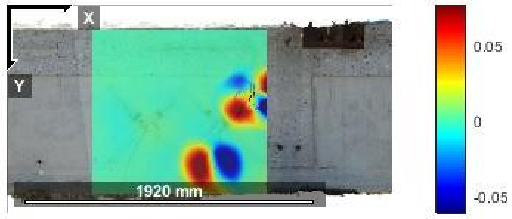

Type: exy-plot
Reference Name: shearsensor_01.png
Current Name: shearsensor_06.png
Analysis type: regular
RG-DIC Radius: 60 | Strain Radius: 15 | Subset Spacing: 5
Diffnorm Cutoff: 1e-06 | Iteration Cutoff: 50 | Threads: 4
Step Analysis: Disabled
RG-DIC Subset Truncation: Disabled | Strain Subset Truncation: Disabled
Image Correspondences: [0 5]
Units/pixels: 1.6307 mm/pixels
Correlation Coefficient Cutoff: 1.7933
Radial Lens Distortion Coefficient: 0
Max: 0.0981 | Median: 0.0006 | Min: -0.1440

(e)

Figure 46 E_{xy} of different stages in shearing zone

(a)042; (b)043; (c)044; (d)045; (e)046.

As for the quantitative analysis, the displacement and corresponding strain in two loading stages with respect to the aluminum frames is shown in Table 24. The strains calculated directly by DIC technology are provided in Figure 47.

	Displacement [mm]		
Transducer measurement	Stage	043	045
	SH1A	0.005952	0.009296
	SH1B	-0.038408	-0.038107
	SH2A	0.016966	0.495058
	SH2B	-0.018296	-0.025576
	L0	707	707

Shearing strains	Strain [$\mu\varepsilon$]		
	Stage	043	045
SH1A	Transducer	8.42	13.15
	DIC	83.48	471.47
SH1B	Transducer	-54.33	-53.90
	DIC	-297.44	-98.26
SH2A	Transducer	24.00	700.22
	DIC	43.38	670.92
SH2B	Transducer	-25.88	-36.18
	DIC	-89.91	-64.20

Table 24 Comparison of shearing strain E_{xy}.

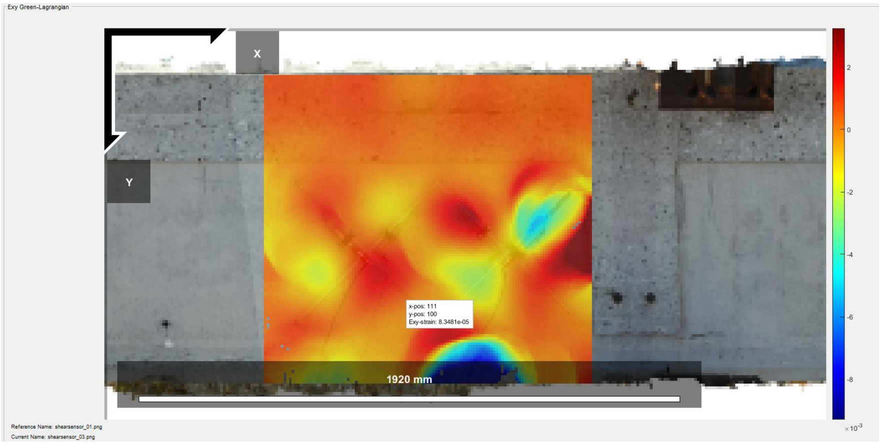

(a) Shearing strain E_{xy} around SH1A at “043”

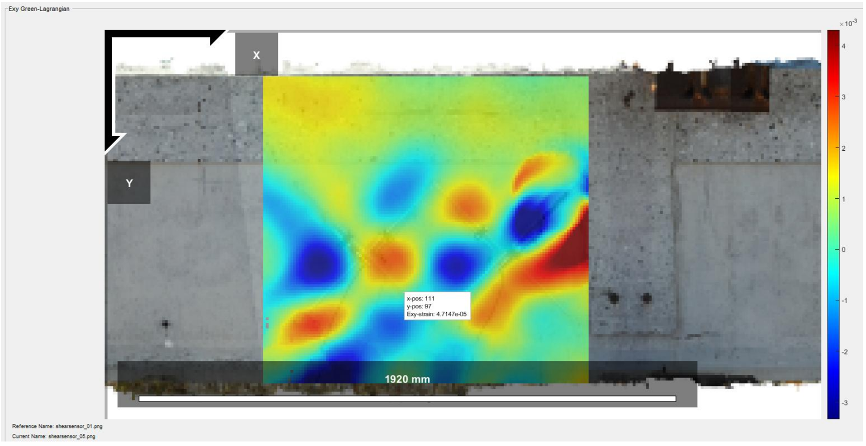

(b) Shearing strain E_{xy} around SH1A at “045”

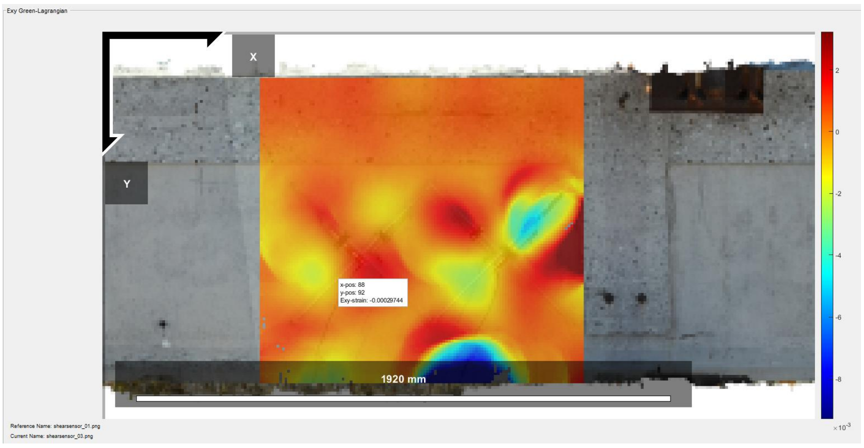

(c) Shearing strain E_{xy} around SH1B at “043”

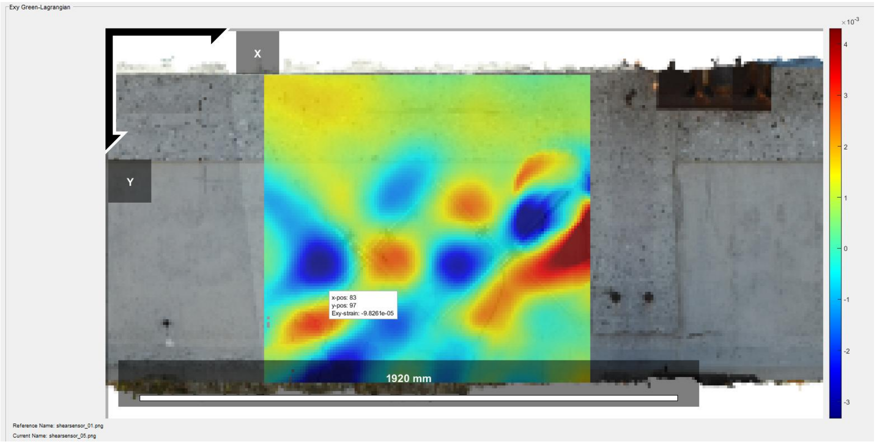

(d) Shearing strain E_{xy} around SH1B at “045”

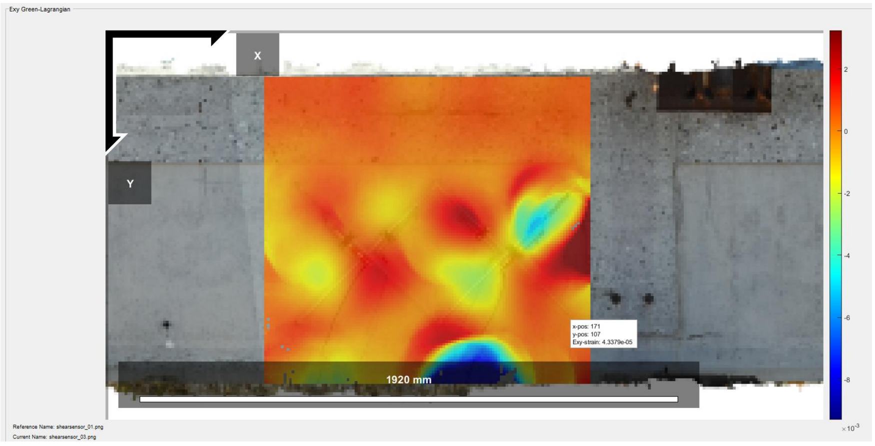

(e) Shearing strain E_{xy} around SH2A at “043”

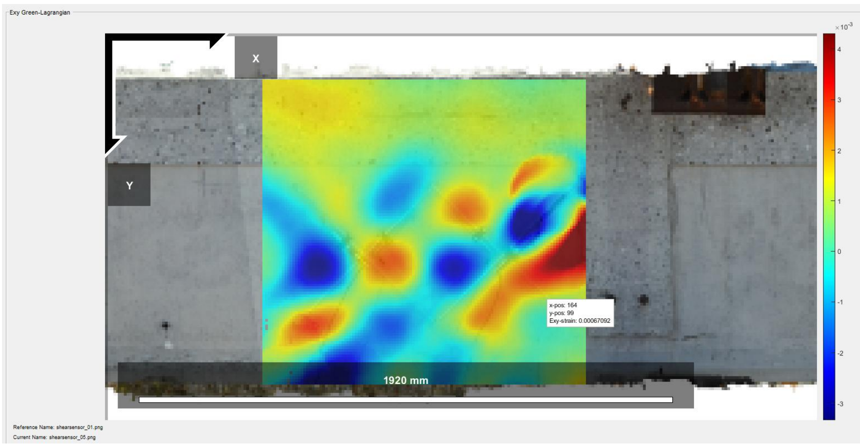

(f) Shearing strain E_{xy} around SH2A at “045”

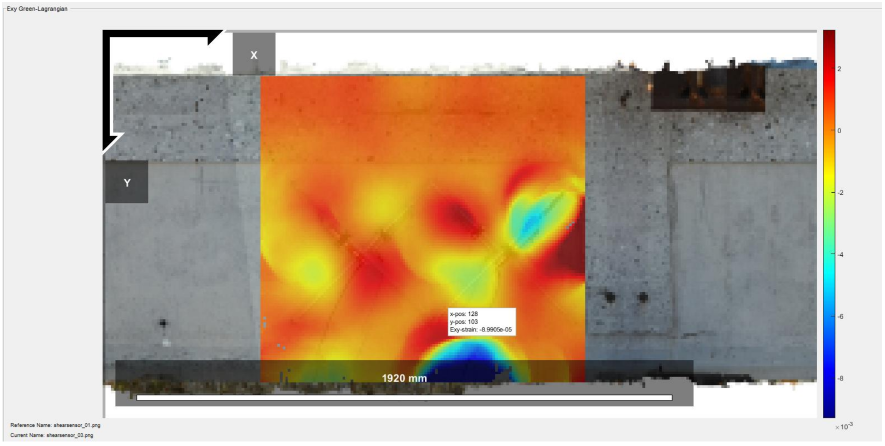

(g) Shearing strain E_{xy} around SH2B at “043”

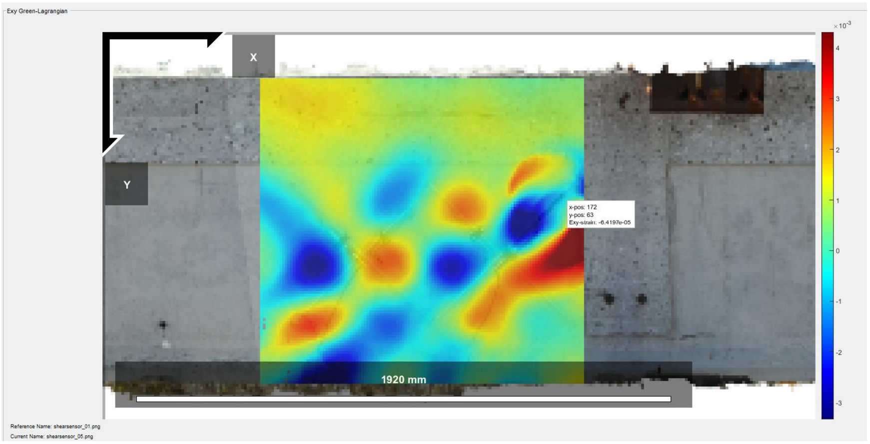

(h) Shearing strain E_{xy} around SH2B at “045”

Figure 47 Shearing strain E_{xy} of 4 transducers at loading stages.

It’s conspicuous that DIC estimates the shearing strains as well as its work in the assessment of bending strains, whose values are preferable to be in the same magnitude with that of the reference standard.

6. Conclusion and Recommendation

This study has detailed a set of strategic photogrammetric procedures executed and described for the structural monitoring in a large-scale FPBT on a PC bridge girder. With the implementation of several innovative geomatics tools and techniques including total station and UAV, Agisoft Metashape, QGIS and MATLAB, the measuring outcomes are in satisfactory agreement with the transducer-based assessment during the experimental test with respect to the global structural behavior of the girder, overcoming with some physical limitations from external environment. They can be summarized as:

A. The convenience and feasibleness of UAV photogrammetry has been proved in the assessment of displacement and deformation with significant accuracy at millimeter level.

B. Many pre-processing steps can be adopted to the images and data to increase the quality of input information.

C. In the study of vertical deflection, variation between photogrammetry-based data and the reference values offered by LVDTs could be relatively large, especially in two loading phases where larger displacement happens, up to 10 mm. In this case, DIC technology provides a more reliable estimation with acceptable error range within 15%.

D. In the consideration of strains, orthomosaic-based DIC can provide a reliable calculation with high precision. One the one hand, it can be used to describe the strain distribution along depth under pure bending; On the other hand, its outstanding ability to display shearing strain paves the way to predict the potential behavior of the whole element even through a small investigation area.

E. DEM is helpful to increase attention to the failure phenomenon in lateral direction, which contributes to the proper design and construction practice of structural elements, i.e., stirrups.

The proposed work provides some advantageous information in the assessment of efficacy of unique measurement techniques regarding different specific tasks. What's more, the method proposed is efficient and economic, and it's suitable for widespread use. Considering these strengths, the study will facilitate improved understanding, enhanced monitoring accuracy, and more effective management of civil infrastructure. Even more, it may pave the way for a groundbreaking hybrid structural monitoring system tailored for large-scale experimental tests, which provides unparalleled insights into the structural behavior, deformation patterns, and response to dynamic loading, all while delivering the visual context necessary for a deeper understanding.

However, there are still some aspects for improvement of this research:

A. Accuracy could be improved further by the adoption of cameras with higher resolution, and the selection of test environment with less external interference.

B. Formulating and implementing a complete and thoughtful experimental plan can minimize missing data and experimental errors, for example, the definition of flight planning and ground sample distance.
C. More controlled trials can make the experimental results more convincing and authoritative. For instance, more structural elements could be under investigation or more analysis platforms could be introduced for comparison.

Further development of this topic and research could involve the synchronization of several drones to facilitate systematic displacement monitoring of structures if possible and focus on more complex experimental tests like full-modal dynamic analysis. What's more, it could also be interesting in springing up a platform or system where DIC is integrated with UAV photogrammetry with the purpose of application in structural inspection.

Acknowledgement

We appreciate the esteemed members of the BRIDGE|50 research project for their collaborative efforts and contributions. Special gratitude is owed to the Management Committee, including S.C.R. Piemonte as President, Politecnico di Milano as Scientific Coordinator, Politecnico di Torino as Scientific Responsible of the Experimental Activities, Lombardi Engineering as Secretary, and the Piedmont Region, City of Turin, Metropolitan City of Turin, TNE Torino Nuova Economia, ATI Itinera & C.M.B., ATI Despe & Perino Piero, and the Quaranta Group for their invaluable support and dedication. We also acknowledge the BRIDGE|50 website as a valuable resource for further information on this groundbreaking project: http://www.bridge50.org.

Meanwhile we would like to express our sincere gratitude to the geomatics researchers of the DIATI department from Politecnico di Torino for their invaluable contribution in conducting diverse combined topographic and photogrammetric surveys. We sincerely acknowledge their diligent efforts and commitment to advancing the field of geomatics and contributing to the success of this project.

Finally, the authors express sincere gratitude for the guidance and suggestions provided by Professor Francesco Tondolo from the Department of DISEG and Professor Marco Piras from the Department of DIATI during the whole study.

Bibliography

[1] Navarro, I. J., Yepes, V., & Martí, J. V. (2018). Life cycle cost assessment of preventive strategies applied to prestressed concrete bridges exposed to chlorides. Sustainability, 10(3), 845.

[2] Singh, Y. K., & Ray, D. S. (2019). Evaluation of vehicle damage factor in overloading for different types of loading. International Journal of Engineering Science and Computing, 9(03), 20327-20330.

[3] Jang, B., & Mohammadi, J. (2019). Impact of fatigue damage from overloads on bridge life-cycle cost analysis. Bridge Structures, 15(4), 181-186.

[4] Abdulkarem, M., Samsudin, K., Rokhani, F. Z., & A Rasid, M. F. (2020). Wireless sensor network for structural health monitoring: A contemporary review of technologies, challenges, and future direction. Structural Health Monitoring, 19(3), 693-735.

[5] Jiao, P., Egbe, K. J. I., Xie, Y., Matin Nazar, A., & Alavi, A. H. (2020). Piezoelectric sensing techniques in structural health monitoring: A state-of-the-art review. Sensors, 20(13), 3730.

[6] Mishra, M., Lourenço, P. B., & Ramana, G. V. (2022). Structural health monitoring of civil engineering structures by using the internet of things: A review. Journal of Building Engineering, 48, 103954.

[7] Biondini, F., & Frangopol, D. M. (2018). Life-cycle performance of civil structure and infrastructure systems: Survey. Journal of Structural Engineering, 144(1), 06017008.

[8] Shenoy, C. V., & Frantz, G. C. (1991). Structural tests of 27-year-old prestressed concrete bridge beams. Pci Journal, 36(5).

[9] Miller, R., & Parekh, K. E. T. A. N. (1994). Destructive testing of deteriorated prestressed box bridge beam. Transportation Research Record, 1460, 37.

[10] Wang, J., Tang, S., Zheng, H., Zhou, C., & Zhu, M. (2020). Flexural behavior of a 30-meter full-scale simply supported prestressed concrete box girder. Applied Sciences, 10(9), 3076.

[11] Labia, Y., Saiidi, M. S., & Douglas, B. (1997). Full-scale testing and analysis of 20-year-old pretensioned concrete box girders. Structural Journal, 94(5), 471-482.

[12] Huffman, J. M. (2012). Destructive testing of a full-scale 43-year-old adjacent prestressed concrete box beam bridge: Middle and west spans (Doctoral dissertation, Ohio University).

[13] Su, J. Z., Ma, X. L., Chen, B. C., & Sennah, K. (2020). Full-scale bending test and parametric study on a 30-m span prestressed ultra-high performance concrete box girder. Advances in Structural Engineering, 23(7), 1276-1289.

[14] Shi, Z., Yang, S., Pu, Q., & Zhang, Y. (2019). Fatigue performance of orthotropic steel decks in long-span cable-stayed steel-box girder railway bridges. Journal of Bridge Engineering, 24(5), 04019035.

[15] Zhang, Y., Fang, Z., Jiang, R., Xiang, Y., Long, H., & Lu, J. (2020). Static performance of a long-span concrete cable-stayed bridge subjected to multiple-cable loss during construction. Journal of Bridge Engineering, 25(3), 04020002.

[16] Hou, R., & Xia, Y. (2021). Review of the new development of vibration-based damage identification for civil engineering structures: 2010–2019. Journal of Sound and Vibration, 491, 115741.

[17] Park, G., Sohn, H., Farrar, C. R., & Inman, D. J. (2003). Overview of piezoelectric impedance-based health monitoring and path forward. Shock and vibration digest, 35(6), 451-464.

[18] Kuang, K. S. C., Quek, S. T., Koh, C. G., Cantwell, W. J., & Scully, P. J. (2009). Plastic optical fiber sensors for structural health monitoring: A review of recent progress. Journal of sensors, 2009.

[19] Wu, L., & Casciati, F. (2014). Local positioning systems versus structural monitoring: a review. Structural Control and Health Monitoring, 21(9), 1209-1221.

[20] Liu, C., Park, J. W., Spencer, B. F., Moon, D. S., & Fan, J. (2017). Sensor fusion for structural tilt estimation using an acceleration-based tilt sensor and a gyroscope. Smart Materials and Structures, 26(10), 105005.

[21] Sony, S., Laventure, S., & Sadhu, A. (2019). A literature review of next-generation smart sensing technology in structural health monitoring. Structural Control and Health Monitoring, 26(3), e2321.

[22] Mucchi, L., Jayousi, S., Martinelli, A., Caputo, S., Intrieri, E., Gigli, G., ... & Nannipieri, L. (2018). A flexible wireless sensor network based on ultra-wide band technology for ground instability monitoring. Sensors, 18(9), 2948.

[23] Cefalo, R., Cociancich, A., Iansig, M., Montagner, G., DiBartolomeo, M., Ferro, F., & Manzoni, G. (2011). ʻPaleo-environmental Researches on Aquileia territory in the ancient timesʼ View project Integrated Topographic, GNSS, Remote Sensing and GIS/WebGIS Techniques Applied to the Study of Aquileia River Port Structures.

[24] Gordan, M., Ismail, Z., Ghaedi, K., Ibrahim, Z., Hashim, H., Ghayeb, H. H., & Talebkhah, M. (2021). A brief overview and future perspective of unmanned aerial

systems for in-service structural health monitoring. Eng. Adv, 1(1), 9-15.

[25] Lydon, D., Lydon, M., Taylor, S., Del Rincon, J. M., Hester, D., & Brownjohn, J. (2019). Development and field testing of a vision-based displacement system using a low-cost wireless action camera. Mechanical Systems and Signal Processing, 121, 343-358.

[26] Ekinci, A., Muturi, T., & Ferreira, P. M. V. (2021). Aerial close-range photogrammetry to quantify deformations of the pile retaining walls. Journal of the Indian Society of Remote Sensing, 49, 1051-1066.

[27] Zhao, S., Kang, F., Li, J., & Ma, C. (2021). Structural health monitoring and inspection of dams based on UAV photogrammetry with image 3D reconstruction. Automation in Construction, 130, 103832.

[28] Suhovilov, B., Sartasov, E., Gornykh, E., & Aliukov, S. (2017). Development of a photogrammetric system for measuring spatial coordinates of control points of large-size structures. In Proceedings of the World Congress on Engineering (Vol. 2).

[29] Blasone, G., Cavalli, M., Marchi, L., & Cazorzi, F. (2014). Monitoring sediment source areas in a debris-flow catchment using terrestrial laser scanning. Catena, 123, 23-36.

[30] Milan, D. J., Heritage, G. L., Large, A. R., & Fuller, I. C. (2011). Filtering spatial error from DEMs: Implications for morphological change estimation. Geomorphology, 125(1), 160-171.

[31] Taddia, Y., Corbau, C., Zambello, E., & Pellegrinelli, A. (2019). UAVs for structure-from-motion coastal monitoring: A case study to assess the evolution of embryo dunes over a two-year time frame in the po river delta, Italy. Sensors, 19(7), 1717.

[32] Strozzi, T., Delaloye, R., Kääb, A., Ambrosi, C., Perruchoud, E., & Wegmüller, U. (2010). Combined observations of rock mass movements using satellite SAR interferometry, differential GPS, airborne digital photogrammetry, and airborne photography interpretation. Journal of Geophysical Research: Earth Surface, 115(F1).

[33] Sutton, M. A., Matta, F., Rizos, D., Ghorbani, R., Rajan, S., Mollenhauer, D. H., & Lasprilla, A. O. (2017). Recent progress in digital image correlation: background and developments since the 2013 WM Murray Lecture. Experimental Mechanics, 57, 1-30.

[34] Sutton, M. A., Matta, F., Rizos, D., Ghorbani, R., Rajan, S., Mollenhauer, D. H., ... & Lasprilla, A. O. (2017). Recent progress in digital image correlation: background

and developments since the 2013 WM Murray Lecture. Experimental Mechanics, 57, 1-30.

[35] Lucieer, A., Jong, S. M. D., & Turner, D. (2014). Mapping landslide displacements using Structure from Motion (SfM) and image correlation of multi-temporal UAV photography. Progress in physical geography, 38(1), 97-116.

[36] Shi, B., & Liu, C. (2015, December). UAV for landslide mapping and deformation analysis. In International Conference on Intelligent Earth Observing and Applications 2015 (Vol. 9808, pp. 197-208). SPIE.

[37] Kalaitzakis, M., Kattil, S. R., Vitzilaios, N., Rizos, D., & Sutton, M. (2019, June). Dynamic structural health monitoring using a DIC-enabled drone. In 2019 International Conference on Unmanned Aircraft Systems (ICUAS) (pp. 321-327). IEEE.

[38] Puniach, E., Gruszczyński, W., Ćwiąkała, P., & Matwij, W. (2021). Application of UAV-based orthomosaics for determination of horizontal displacement caused by underground mining. ISPRS Journal of Photogrammetry and Remote Sensing, 174, 282-303.

[39] Savino, P., Tondolo, F., Sabia, D., Quattrone, A., Biondini, F., Rosati, G., ... & Chiaia, B. (2023). Large-Scale Experimental Static Testing on 50-Year-Old Prestressed Concrete Bridge Girders. Applied Sciences, 13(2), 834.

[40] Bridge 50 project | Applied research - SISCON. (2023, January 30). Centro InterdipartimentaleSISCON. https://siscon.polito.it/en/applied-research/bridge-50project/

[41] Savino, P., Anghileri, M., Chiara, M., Salza, B., & Quaranta, L. (2021). Corso Grosseto viaduct: Historical and technical overview. Bridge Maintenance, Safety, Management, Life-Cycle Sustainability and Innovations, 3345-3351.

[42] Savino, P., Quattrone, A., Sabia, D., Chiaia, B., Tondolo, F., Anghileri, M., ... & Rosati, G. (2023). Large-scale experimental testing of 50-year-old prestressed concrete bridge girder. In Lifecycle of Structures and Infrastructure Systems (pp. 2061-2068). CRC Press.

[43] McGlone, C., Mikhail, E., & Bethel, J. (2004). Manual of photogrammetry: American society for photogrammetry and remote sensing. Bethesda, MD.

[44] Lewis, Q., Konsoer, K., & Leitner, M. (2022). How sUAS has pushed forward on-demand low altitude remote sensing in Geography. In sUAS applications in Geography (pp. 1-12). Cham: Springer International Publishing.

[45] DIC Algorithms. (n.d.). https://www.ncorr.com/index.php/dic-algorithms

[46] Srl, E. P. (2019, November 22). Leica Nova MS50. EuroTec Pisa Strumentazione Al Top Della Gamma. https://www.eurotecpisa.eu/prodotti/prodotti-fuori-produzione/item/315-leica-nova-ms50.html

[47] Zenmuse P1 - UAV load gimbal camera - DJI Enterprise. (n.d.). DJI. https://enterprise.dji.com/zenmuse-p1

[48] Vizzaccaro, A., Givois, A., Longobardi, P., Shen, Y., Deü, J. F., Salles, L., ... & Thomas, O. (2020). Non-intrusive reduced order modelling for the dynamics of geometrically nonlinear flat structures using three-dimensional finite elements. Computational Mechanics, 66, 1293-1319.

[49] Altun, F., Haktanir, T., & Ari, K. (2006). Experimental investigation of steel fiber reinforced concrete box beams under bending. Materials and structures, 39, 491-499.

Appendix

1. Agisoft Metashape processing report for project “041”
2. Agisoft Metashape processing report for project “042”
3. Agisoft Metashape processing report for project “043”
4. Agisoft Metashape processing report for project “044”
5. Agisoft Metashape processing report for project “045”
6. Agisoft Metashape processing report for project “046”

Agisoft Metashape

Processing Report 1

21 September 2023

Survey Data

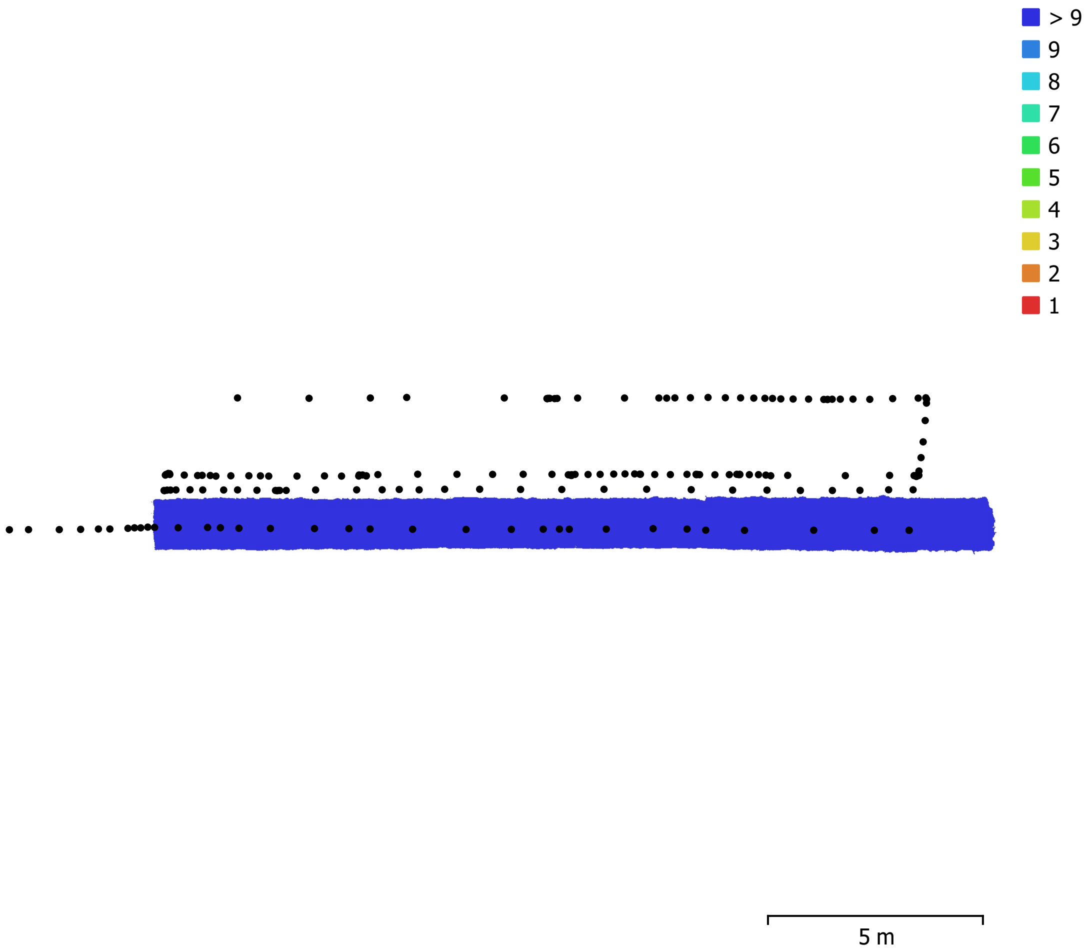

Fig. 1. Camera locations and image overlap.

Number of images:	187	Camera stations:	186
Flying altitude:	6.14 m	Tie points:	54,660
Ground resolution:	0.751 mm/pix	Projections:	611,725
Coverage area:	23.4 m²	Reprojection error:	1.04 pix

Camera Model	Resolution	Focal Length	Pixel Size	Precalibrated
ZenmuseP1 (35mm)	8192 x 5460	35 mm	4.39 x 4.39 µm	No

Table 1. Cameras.

Camera Calibration

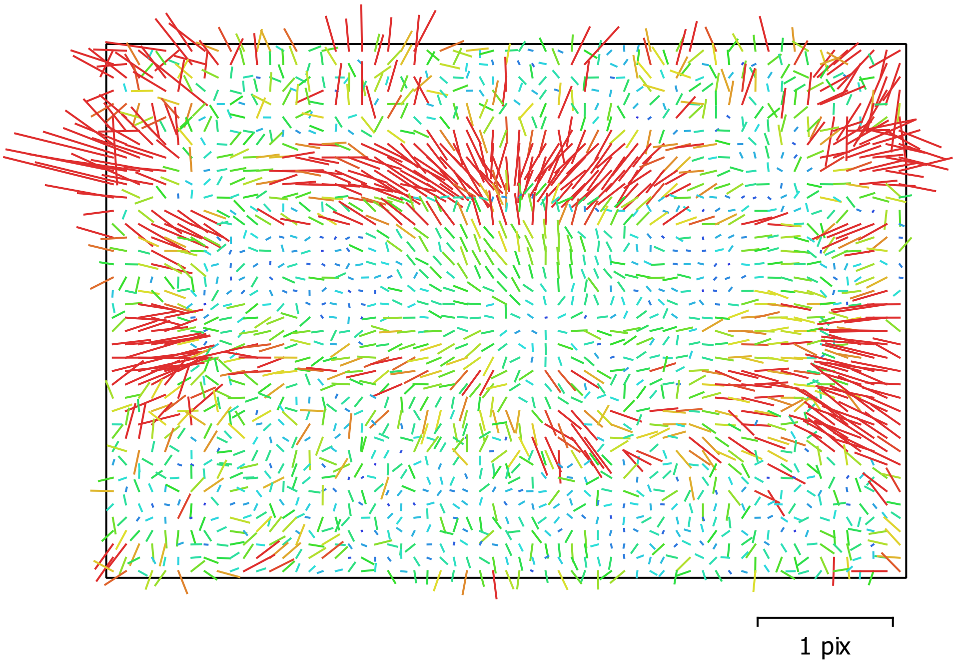

Fig. 2. Image residuals for ZenmuseP1 (35mm).

ZenmuseP1 (35mm)

187 images

Type	Resolution	Focal Length	Pixel Size
Frame	**8192 x 5460**	**35 mm**	**4.39 x 4.39 µm**

	Value	Error	F	Cx	Cy	K1	K2	K3	P1	P2
F	**8212.16**	0.15	1.00	-0.00	-0.13	-0.07	0.06	-0.05	0.03	0.03
Cx	**-25.6358**	0.25		1.00	-0.00	0.01	-0.00	-0.01	0.89	-0.00
Cy	**22.7724**	0.13			1.00	0.05	-0.02	0.02	-0.00	0.43
K1	**-0.042023**	4.4e-05				1.00	-0.96	0.90	0.01	0.07
K2	**0.0203189**	0.00029					1.00	-0.98	-0.01	-0.02
K3	**-0.100805**	0.00058						1.00	-0.00	0.01
P1	**-0.00109183**	5.8e-06							1.00	-0.00
P2	**0.000755412**	2.5e-06								1.00

Table 2. Calibration coefficients and correlation matrix.

Ground Control Points

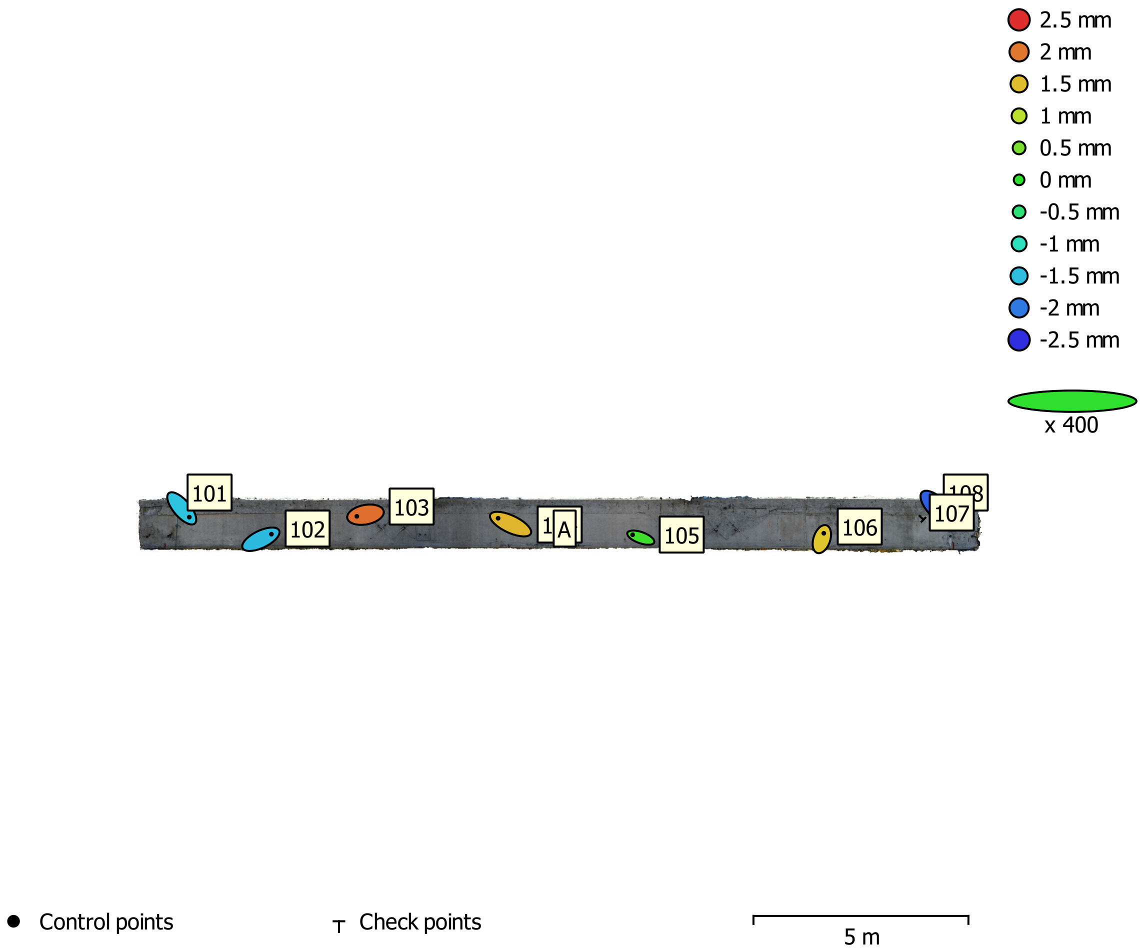

Fig. 3. GCP locations and error estimates.
Z error is represented by ellipse color. X,Y errors are represented by ellipse shape.
Estimated GCP locations are marked with a dot or crossing.

Count	X error (mm)	Y error (mm)	Z error (mm)	XY error (mm)	Total (mm)
7	1.03454	0.719513	1.60051	1.26015	2.03706

Table 3. Control points RMSE.

Label	**X error (mm)**	**Y error (mm)**	**Z error (mm)**	**Total (mm)**	**Image (pix)**
101	0.877185	-1.02113	-1.44579	1.97547	0.818 (16)
102	1.22584	0.591275	-1.52321	2.04266	1.277 (16)
103	-1.00782	-0.191083	2.05974	2.30103	0.974 (16)
104	-1.44774	0.678309	1.55338	2.22914	0.576 (16)
105	-0.949461	0.33617	0.116372	1.01392	0.400 (16)
106	0.227314	0.682011	1.43119	1.6016	0.826 (16)
108	1.07469	-1.07555	-2.1917	2.66745	0.368 (14)
Total	**1.03454**	**0.719513**	**1.60051**	**2.03706**	**0.813**

Table 4. Control points.

Label	**X error (mm)**	**Y error (mm)**	**Z error (mm)**	**Total (mm)**	**Image (pix)**
A					61.882 (14)
107					0.338 (16)
Total					

Table 5. Check points.

Digital Elevation Model

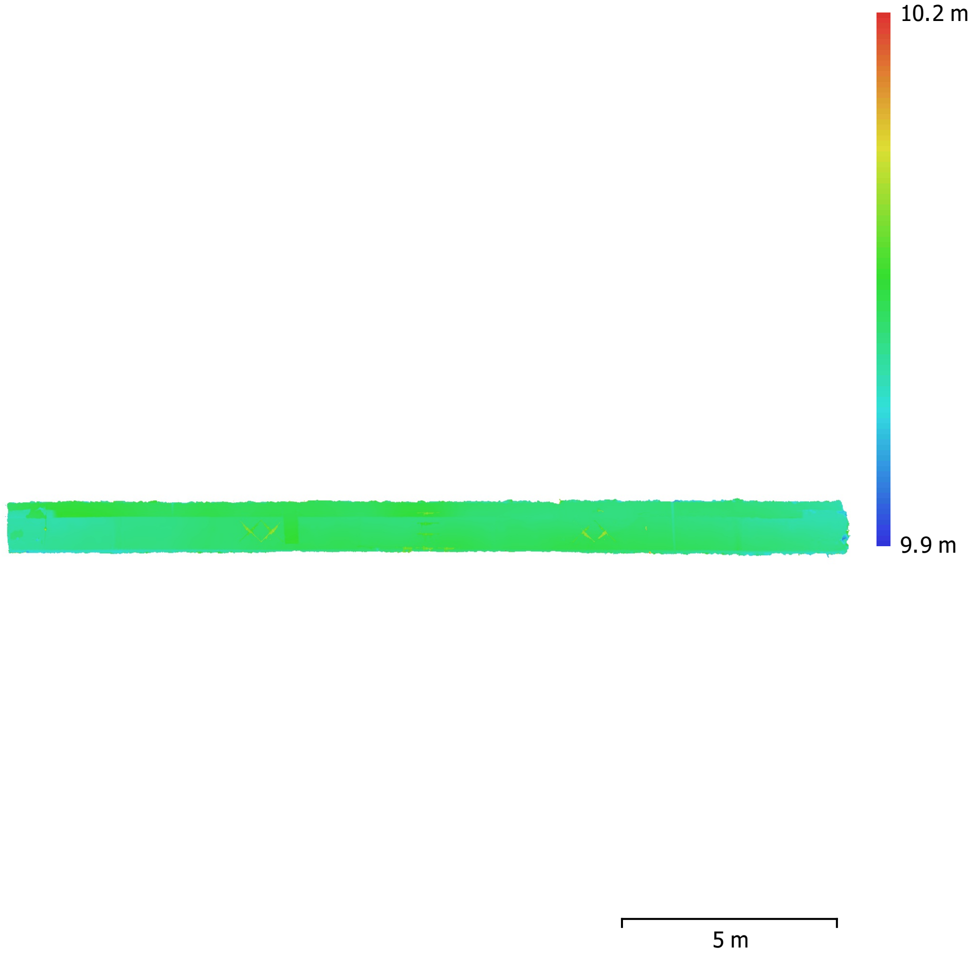

Fig. 4. Reconstructed digital elevation model.

Resolution:	1.5 mm/pix
Point density:	44.3 points/cm²

Processing Parameters

General	
Cameras	187
Aligned cameras	186
Markers	9
Shapes	
Polygon	7
Coordinate system	Local Coordinates (m)
Rotation angles	Yaw, Pitch, Roll
Point Cloud	
Points	54,660 of 268,295
RMS reprojection error	0.231828 (1.03876 pix)
Max reprojection error	0.753975 (48.0628 pix)
Mean key point size	3.89078 pix
Point colors	3 bands, uint8
Key points	2.71 GB
Average tie point multiplicity	7.7387
Alignment parameters	
Accuracy	High
Generic preselection	Yes
Reference preselection	Source
Key point limit	10,000
Key point limit per Mpx	40,000
Tie point limit	10,000
Exclude stationary tie points	Yes
Guided image matching	Yes
Adaptive camera model fitting	No
Matching time	28 minutes 14 seconds
Matching memory usage	9.74 GB
Alignment time	12 minutes 53 seconds
Alignment memory usage	357.98 MB
Date created	2023:03:14 09:47:25
Software version	1.8.4.14856
File size	41.65 MB
Depth Maps	
Count	186
Depth maps generation parameters	
Quality	High
Filtering mode	Mild
Max neighbors	16
Processing time	1 hours 48 minutes
Memory usage	4.80 GB
Date created	2023:03:28 12:56:11
Software version	1.8.4.14856
File size	881.68 MB
Dense Point Cloud	
Points	67,828,267
Point colors	3 bands, uint8
Depth maps generation parameters	
Quality	High
Filtering mode	Mild

Max neighbors	16
Processing time	1 hours 48 minutes
Memory usage	4.80 GB
Dense cloud generation parameters	
Processing time	1 hours 39 minutes
Memory usage	20.29 GB
Date created	2023:03:28 14:35:17
Software version	1.8.4.14856
File size	984.40 MB
Model	
Faces	912,943
Vertices	459,802
Vertex colors	3 bands, uint8
Depth maps generation parameters	
Quality	High
Filtering mode	Mild
Max neighbors	16
Processing time	1 hours 48 minutes
Memory usage	4.80 GB
Reconstruction parameters	
Surface type	Arbitrary
Source data	Dense cloud
Interpolation	Disabled
Strict volumetric masks	No
Processing time	3 minutes 45 seconds
Memory usage	3.12 GB
Date created	2023:03:29 07:52:32
Software version	1.8.4.14856
File size	20.95 MB
DEM	
Size	19,584 x 7,917
Coordinate system	Local Coordinates (m)
Reconstruction parameters	
Source data	Dense cloud
Interpolation	Disabled
Processing time	8 seconds
Memory usage	150.88 MB
Date created	2023:09:21 11:37:26
Software version	1.8.4.14856
File size	40.62 MB
Orthomosaic	
Size	19,698 x 1,389
Coordinate system	Local Coordinates (m)
Colors	3 bands, uint8
Reconstruction parameters	
Blending mode	Mosaic
Surface	DEM
Enable hole filling	Yes
Enable ghosting filter	No
Processing time	2 minutes 3 seconds
Memory usage	724.54 MB
Date created	2023:03:29 13:24:27
Software version	1.8.4.14856
File size	1.02 GB
System	
Software name	Agisoft Metashape Professional

Software version	1.8.4 build 14856
OS	Windows 64 bit
RAM	31.89 GB
CPU	Intel(R) Core(TM) i7-4770 CPU @ 3.40GHz
GPU(s)	GeForce GTX 760
	GeForce GTX 760

Agisoft Metashape

Processing Report 2

21 September 2023

Survey Data

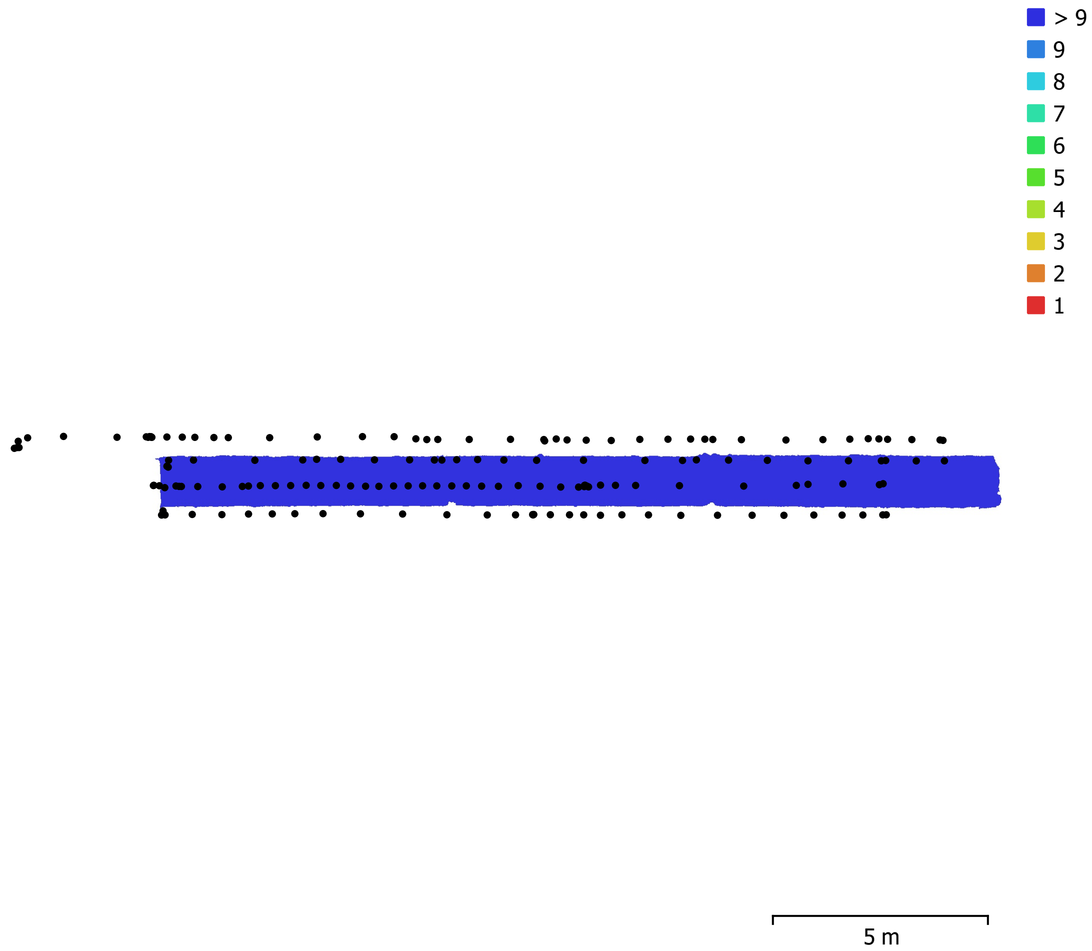

Fig. 1. Camera locations and image overlap.

Number of images:	156	Camera stations:	156
Flying altitude:	6.95 m	Tie points:	92,398
Ground resolution:	0.872 mm/pix	Projections:	830,364
Coverage area:	22.9 m²	Reprojection error:	0.833 pix

Camera Model	**Resolution**	**Focal Length**	**Pixel Size**	**Precalibrated**
ZenmuseP1 (35mm)	8192 x 5460	35 mm	4.39 x 4.39 μm	No

Table 1. Cameras.

Camera Calibration

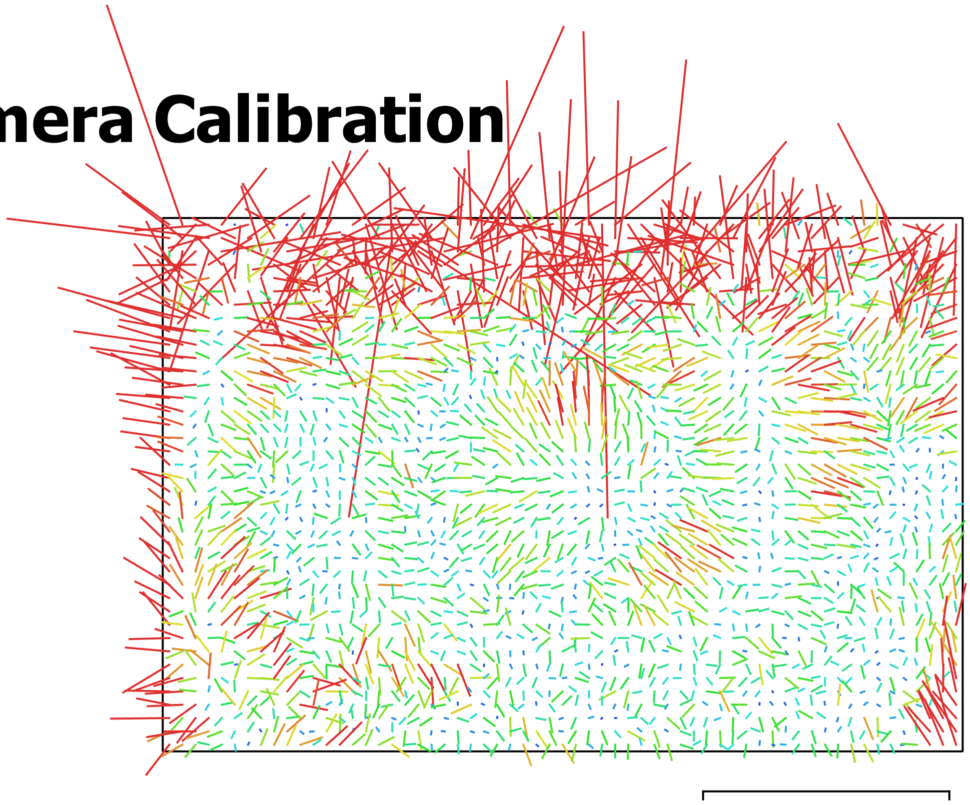

Fig. 2. Image residuals for ZenmuseP1 (35mm).

ZenmuseP1 (35mm)

156 images

Type	Resolution	Focal Length	Pixel Size
Frame	**8192 x 5460**	**35 mm**	**4.39 x 4.39 µm**

	Value	Error	F	Cx	Cy	K1	K2	K3	P1	P2
F	**8202.33**	0.11	1.00	-0.12	0.15	-0.05	0.08	-0.08	-0.02	-0.02
Cx	**-26.4933**	0.17		1.00	-0.05	-0.02	0.02	-0.04	0.75	0.02
Cy	**18.841**	0.13			1.00	-0.01	0.01	-0.01	0.02	-0.18
K1	**-0.0468106**	2.8e-05				1.00	-0.96	0.90	-0.04	-0.02
K2	**0.0171009**	0.00019					1.00	-0.98	0.05	0.04
K3	**-0.0922657**	0.00039						1.00	-0.07	-0.04
P1	**-0.000961466**	4.1e-06							1.00	-0.00
P2	**0.000660001**	1.5e-06								1.00

Table 2. Calibration coefficients and correlation matrix.

Ground Control Points

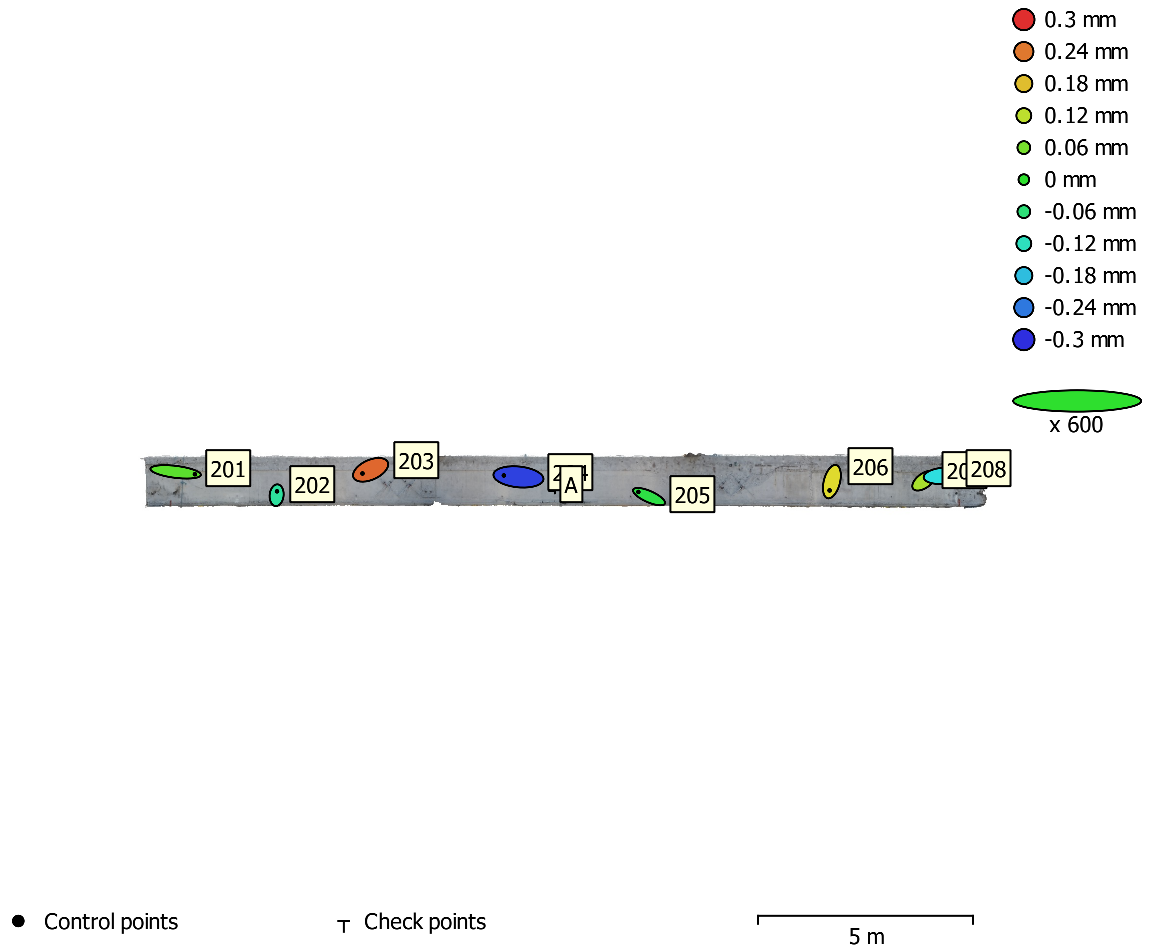

Fig. 3. GCP locations and error estimates.
Z error is represented by ellipse color. X,Y errors are represented by ellipse shape.
Estimated GCP locations are marked with a dot or crossing.

Count	X error (mm)	Y error (mm)	Z error (mm)	XY error (mm)	Total (mm)
8	0.82957	0.336718	0.163193	0.895302	0.910053

Table 3. Control points RMSE.

Label	X error (mm)	Y error (mm)	Z error (mm)	Total (mm)	Image (pix)
201	1.49413	-0.184437	0.0363205	1.50591	0.271 (12)
202	0.0304455	0.300984	-0.0927012	0.316404	0.349 (12)
203	-0.630186	-0.284638	0.253958	0.736647	0.216 (12)
204	-1.13458	0.112981	-0.285462	1.17538	0.268 (12)
205	-0.827739	0.363175	-0.0181247	0.904088	0.155 (12)
206	-0.178432	-0.680375	0.154203	0.720088	0.173 (12)
207	0.406339	0.296889	0.102179	0.513512	0.183 (12)
208	0.840022	0.0754223	-0.150373	0.856701	0.416 (12)
Total	**0.82957**	**0.336718**	**0.163193**	**0.910053**	**0.268**

Table 4. Control points.

Label	X error (mm)	Y error (mm)	Z error (mm)	Total (mm)	Image (pix)
A					0.295 (12)
Total					

Table 5. Check points.

Digital Elevation Model

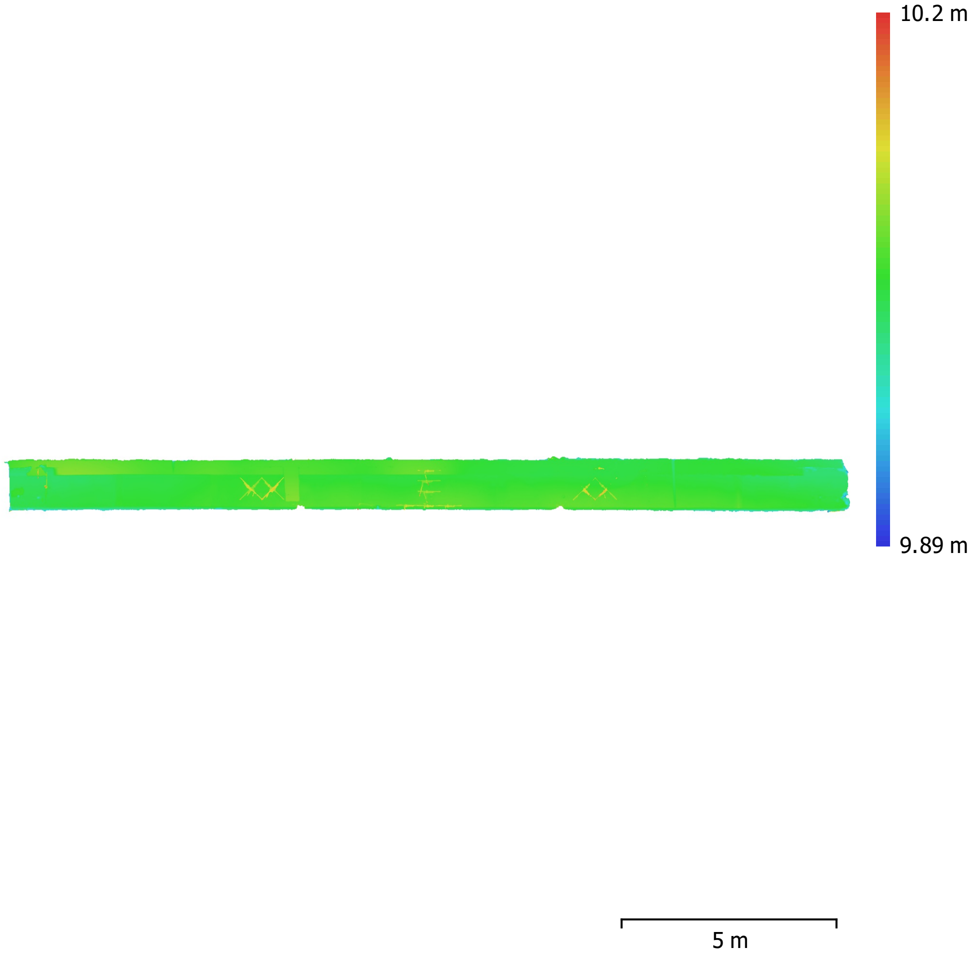

Fig. 4. Reconstructed digital elevation model.

Resolution:	1.74 mm/pix
Point density:	32.8 points/cm²

Processing Parameters

General	
Cameras	156
Aligned cameras	156
Markers	9
Shapes	
Polygon	6
Coordinate system	Local Coordinates (m)
Rotation angles	Yaw, Pitch, Roll
Point Cloud	
Points	92,398 of 229,351
RMS reprojection error	0.177787 (0.833254 pix)
Max reprojection error	0.564016 (46.7532 pix)
Mean key point size	3.67302 pix
Point colors	3 bands, uint8
Key points	1.85 GB
Average tie point multiplicity	7.36408
Alignment parameters	
Accuracy	High
Generic preselection	Yes
Reference preselection	Source
Key point limit	10,000
Key point limit per Mpx	40,000
Tie point limit	10,000
Exclude stationary tie points	Yes
Guided image matching	Yes
Adaptive camera model fitting	No
Matching time	24 minutes 14 seconds
Matching memory usage	2.64 GB
Alignment time	14 minutes 10 seconds
Alignment memory usage	464.66 MB
Date created	2023:03:14 17:08:23
Software version	1.8.4.14856
File size	35.01 MB
Depth Maps	
Count	156
Depth maps generation parameters	
Quality	High
Filtering mode	Mild
Max neighbors	16
Processing time	1 hours 18 minutes
Memory usage	10.76 GB
Date created	2023:03:15 14:50:57
Software version	1.8.4.14856
File size	890.27 MB
Dense Point Cloud	
Points	29,987,227
Point colors	3 bands, uint8
Depth maps generation parameters	
Quality	High
Filtering mode	Mild

Max neighbors	16
Processing time	1 hours 18 minutes
Memory usage	10.76 GB
Dense cloud generation parameters	
Processing time	1 hours 44 minutes
Memory usage	19.12 GB
Date created	2023:03:15 16:35:31
Software version	1.8.4.14856
File size	510.96 MB
Model	
Faces	647,973
Vertices	325,735
Vertex colors	3 bands, uint8
Depth maps generation parameters	
Quality	High
Filtering mode	Mild
Max neighbors	16
Processing time	1 hours 18 minutes
Memory usage	10.76 GB
Reconstruction parameters	
Surface type	Arbitrary
Source data	Dense cloud
Interpolation	Disabled
Strict volumetric masks	No
Processing time	4 minutes 13 seconds
Memory usage	2.17 GB
Date created	2023:03:24 09:21:44
Software version	1.8.4.14856
File size	14.86 MB
DEM	
Size	22,630 x 9,174
Coordinate system	Local Coordinates (m)
Reconstruction parameters	
Source data	Dense cloud
Interpolation	Disabled
Processing time	14 seconds
Memory usage	150.01 MB
Date created	2023:09:21 11:13:38
Software version	1.8.4.14856
File size	29.63 MB
Orthomosaic	
Size	19,671 x 1,359
Coordinate system	Local Coordinates (m)
Colors	3 bands, uint8
Reconstruction parameters	
Blending mode	Disabled
Surface	Mesh
Enable hole filling	Yes
Enable ghosting filter	No
Processing time	2 minutes 15 seconds
Memory usage	1.41 GB
Date created	2023:09:21 11:15:28
Software version	1.8.4.14856
File size	920.22 MB
System	
Software name	Agisoft Metashape Professional

Software version	1.8.4 build 14856
OS	Windows 64 bit
RAM	31.89 GB
CPU	Intel(R) Core(TM) i7-4770 CPU @ 3.40GHz
GPU(s)	GeForce GTX 760
	GeForce GTX 760

Agisoft Metashape

Processing Report 3

21 September 2023

Survey Data

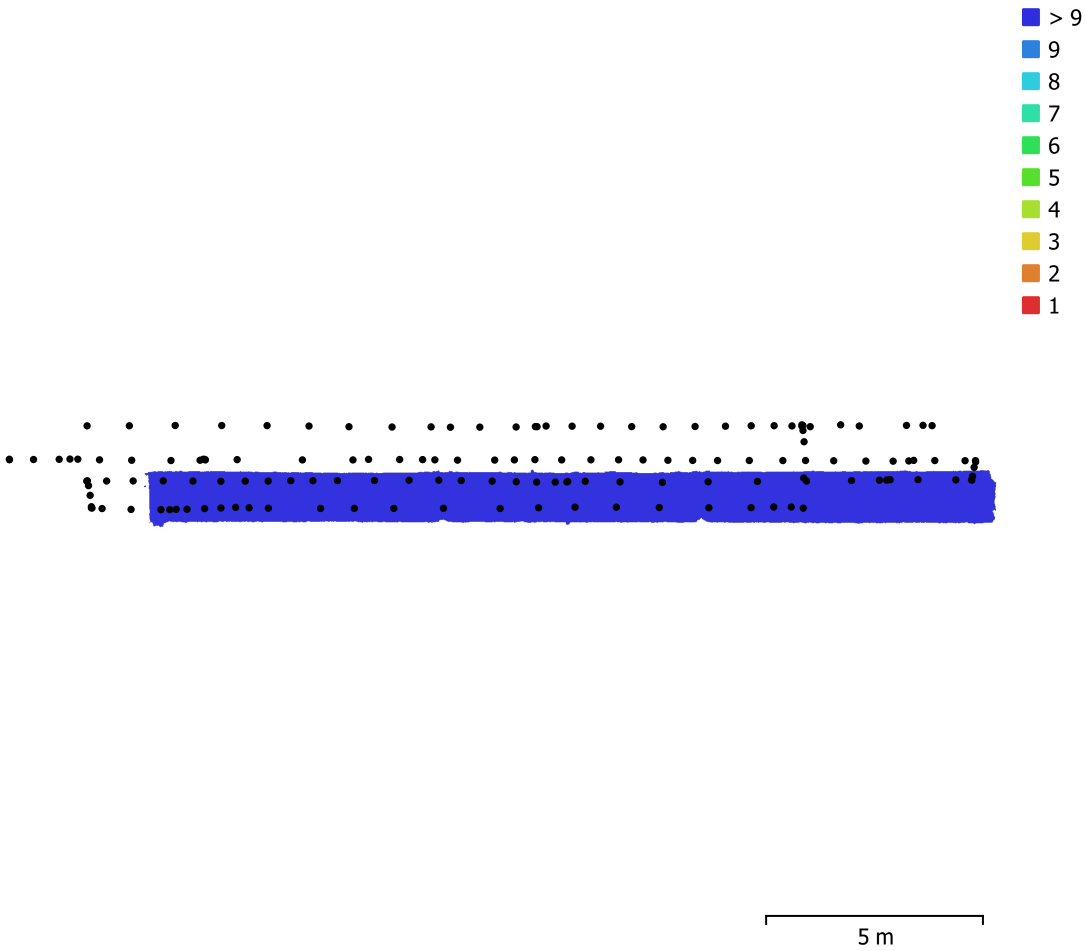

Fig. 1. Camera locations and image overlap.

Number of images:	150	Camera stations:	150
Flying altitude:	7.18 m	Tie points:	86,620
Ground resolution:	0.937 mm/pix	Projections:	803,341
Coverage area:	22.7 m²	Reprojection error:	0.885 pix

Camera Model	Resolution	Focal Length	Pixel Size	Precalibrated
ZenmuseP1 (35mm)	8192 x 5460	35 mm	4.39 x 4.39 μm	No

Table 1. Cameras.

Camera Calibration

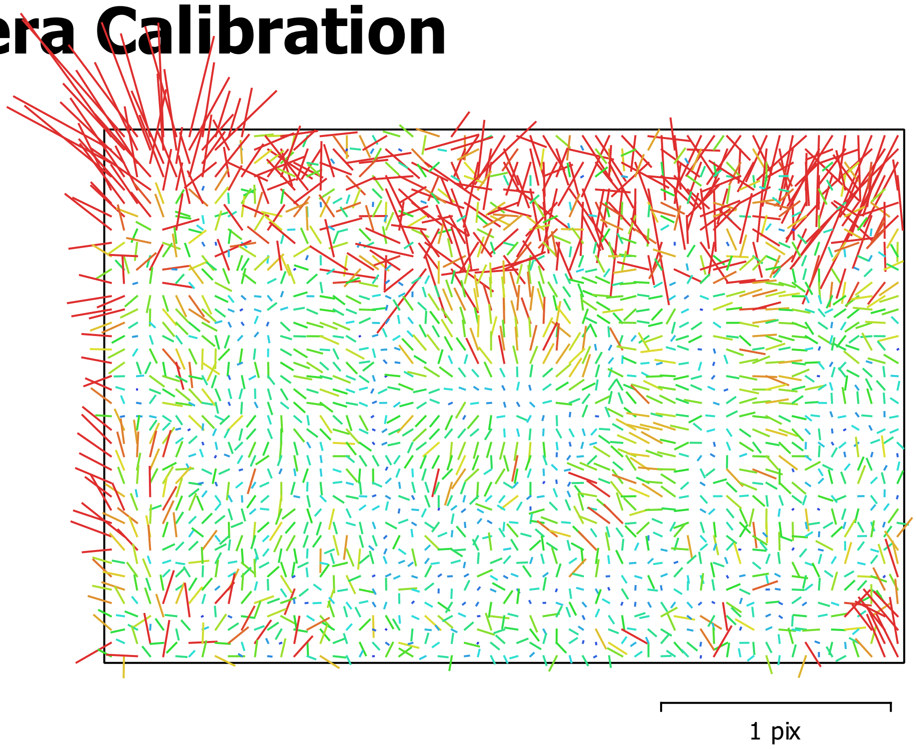

Fig. 2. Image residuals for ZenmuseP1 (35mm).

ZenmuseP1 (35mm)

150 images

Type	Resolution	Focal Length	Pixel Size
Frame	**8192 x 5460**	**35 mm**	**4.39 x 4.39 µm**

	Value	Error	F	Cx	Cy	K1	K2	K3	P1	P2
F	**8199.72**	0.14	1.00	-0.05	0.17	0.01	-0.04	0.06	-0.02	0.12
Cx	**-16.9991**	0.21		1.00	-0.03	0.01	0.00	-0.01	0.86	-0.05
Cy	**16.8959**	0.074			1.00	-0.05	0.07	-0.10	-0.01	0.25
K1	**-0.0473803**	3.1e-05				1.00	-0.96	0.90	0.00	-0.01
K2	**0.0139562**	0.00021					1.00	-0.98	0.00	0.04
K3	**-0.0922131**	0.00045						1.00	-0.02	-0.04
P1	**-0.000819273**	4.5e-06							1.00	-0.05
P2	**0.000610342**	1.4e-06								1.00

Table 2. Calibration coefficients and correlation matrix.

Ground Control Points

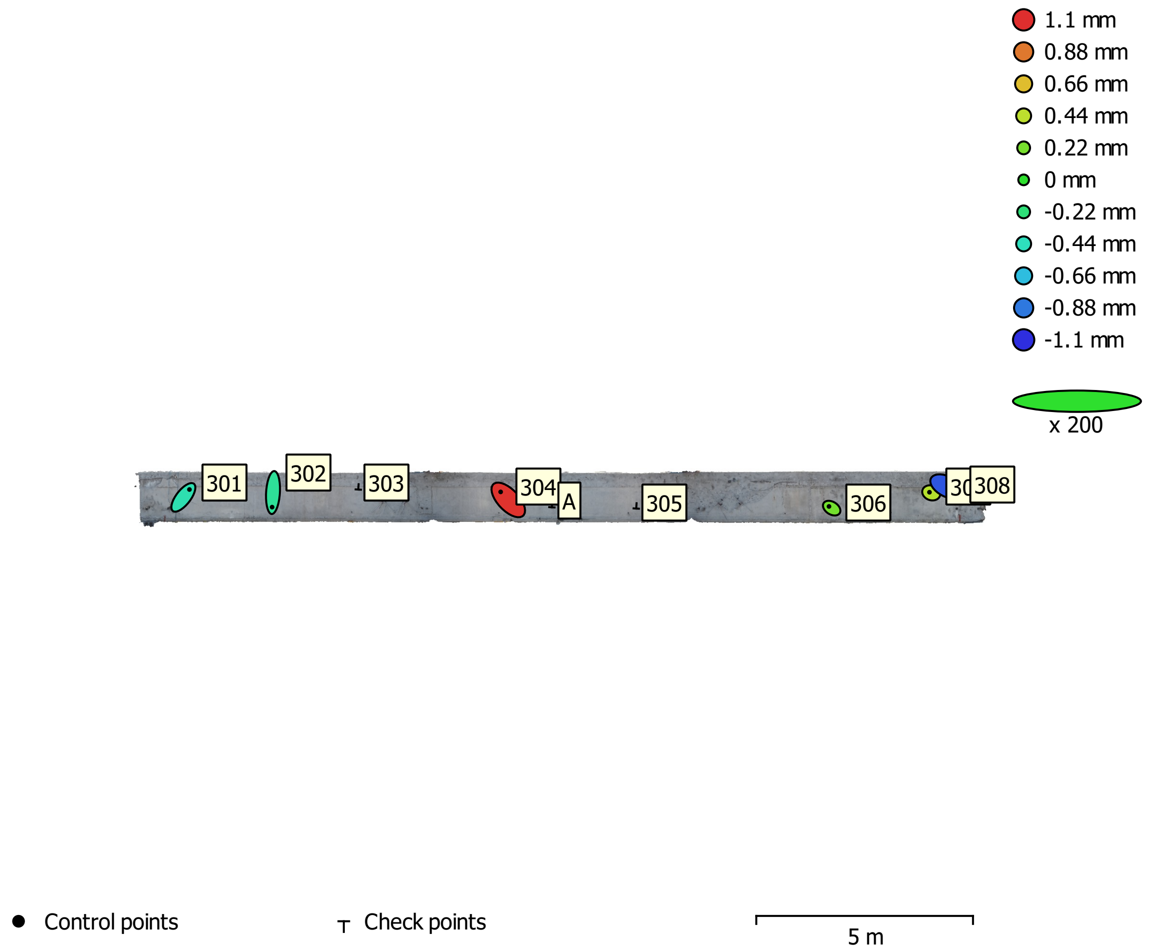

Fig. 3. GCP locations and error estimates.
Z error is represented by ellipse color. X,Y errors are represented by ellipse shape.
Estimated GCP locations are marked with a dot or crossing.

Count	X error (mm)	Y error (mm)	Z error (mm)	XY error (mm)	Total (mm)
6	1.16665	1.77352	0.660436	2.12284	2.2232

Table 3. Control points RMSE.

Label	X error (mm)	Y error (mm)	Z error (mm)	Total (mm)	Image (pix)
301	1.40306	1.81095	-0.398574	2.32529	0.442 (20)
304	-1.75575	1.85055	1.08391	2.77165	0.179 (17)
306	-0.621698	0.386652	0.20397	0.760008	0.254 (15)
307	-0.40719	0.142912	0.415679	0.599179	0.318 (13)
308	1.58758	-0.827495	-0.982229	2.04204	0.261 (16)
302	-0.206008	-3.36357	-0.322752	3.38529	0.369 (17)
Total	**1.16665**	**1.77352**	**0.660436**	**2.2232**	**0.322**

Table 4. Control points.

Label	X error (mm)	Y error (mm)	Z error (mm)	Total (mm)	Image (pix)
A					0.209 (14)
303					0.206 (17)
305					0.227 (16)
Total					

Table 5. Check points.

Digital Elevation Model

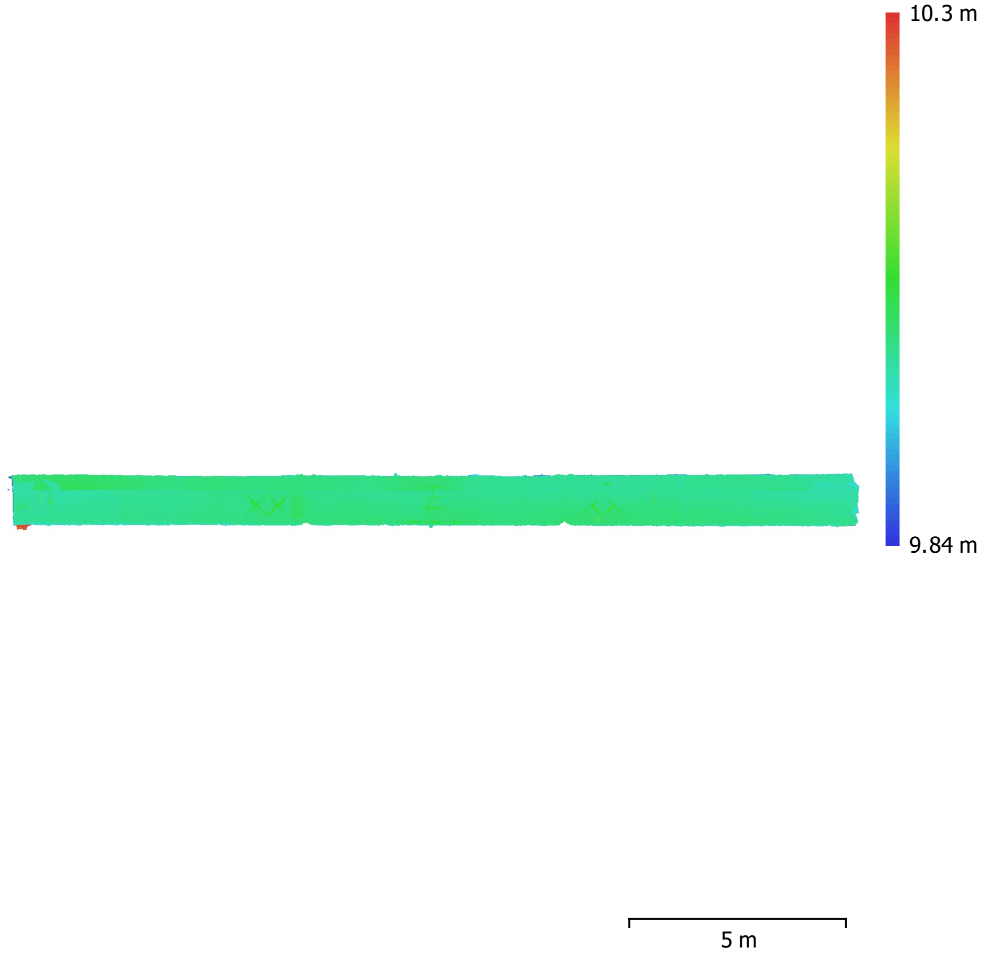

Fig. 4. Reconstructed digital elevation model.

Resolution:	1.87 mm/pix
Point density:	28.5 points/cm²

Processing Parameters

General	
Cameras	150
Aligned cameras	150
Markers	9
Shapes	
Polygon	6
Coordinate system	Local Coordinates (m)
Rotation angles	Yaw, Pitch, Roll
Point Cloud	
Points	86,620 of 195,243
RMS reprojection error	0.190393 (0.884632 pix)
Max reprojection error	0.5983 (49.209 pix)
Mean key point size	3.67351 pix
Point colors	3 bands, uint8
Key points	1.77 GB
Average tie point multiplicity	8.27483
Alignment parameters	
Accuracy	High
Generic preselection	Yes
Reference preselection	Source
Key point limit	10,000
Key point limit per Mpx	40,000
Tie point limit	10,000
Exclude stationary tie points	Yes
Guided image matching	Yes
Adaptive camera model fitting	No
Matching time	49 minutes 42 seconds
Matching memory usage	2.63 GB
Alignment time	22 minutes 16 seconds
Alignment memory usage	258.36 MB
Date created	2023:03:14 17:41:46
Software version	1.8.4.14856
File size	33.38 MB
Depth Maps	
Count	150
Depth maps generation parameters	
Quality	High
Filtering mode	Mild
Max neighbors	16
Processing time	1 hours 20 minutes
Memory usage	10.86 GB
Date created	2023:03:20 12:08:23
Software version	1.8.4.14856
File size	881.76 MB
Dense Point Cloud	
Points	28,012,644
Point colors	3 bands, uint8
Depth maps generation parameters	
Quality	High
Filtering mode	Mild

Max neighbors	16
Processing time	1 hours 20 minutes
Memory usage	10.86 GB
Dense cloud generation parameters	
Processing time	1 hours 17 minutes
Memory usage	18.91 GB
Date created	2023:03:20 13:25:40
Software version	1.8.4.14856
File size	583.95 MB
Model	
Faces	616,189
Vertices	309,983
Vertex colors	3 bands, uint8
Depth maps generation parameters	
Quality	High
Filtering mode	Mild
Max neighbors	16
Processing time	1 hours 20 minutes
Memory usage	10.86 GB
Reconstruction parameters	
Surface type	Arbitrary
Source data	Dense cloud
Interpolation	Disabled
Strict volumetric masks	No
Processing time	2 minutes 36 seconds
Memory usage	2.37 GB
Date created	2023:03:24 09:05:46
Software version	1.8.4.14856
File size	14.13 MB
DEM	
Size	26,422 x 9,460
Coordinate system	Local Coordinates (m)
Reconstruction parameters	
Source data	Dense cloud
Interpolation	Disabled
Processing time	19 seconds
Memory usage	150.75 MB
Date created	2023:09:21 09:28:24
Software version	1.8.4.14856
File size	24.41 MB
Orthomosaic	
Size	19,644 x 1,319
Coordinate system	Local Coordinates (m)
Colors	3 bands, uint8
Reconstruction parameters	
Blending mode	Disabled
Surface	Mesh
Enable hole filling	Yes
Enable ghosting filter	No
Processing time	1 minutes 46 seconds
Memory usage	1.39 GB
Date created	2023:09:21 11:03:12
Software version	1.8.4.14856
File size	829.21 MB
System	
Software name	Agisoft Metashape Professional

Software version	1.8.4 build 14856
OS	Windows 64 bit
RAM	31.89 GB
CPU	Intel(R) Core(TM) i7-4770 CPU @ 3.40GHz
GPU(s)	GeForce GTX 760
	GeForce GTX 760

Agisoft Metashape

Processing Report 4

21 September 2023

Survey Data

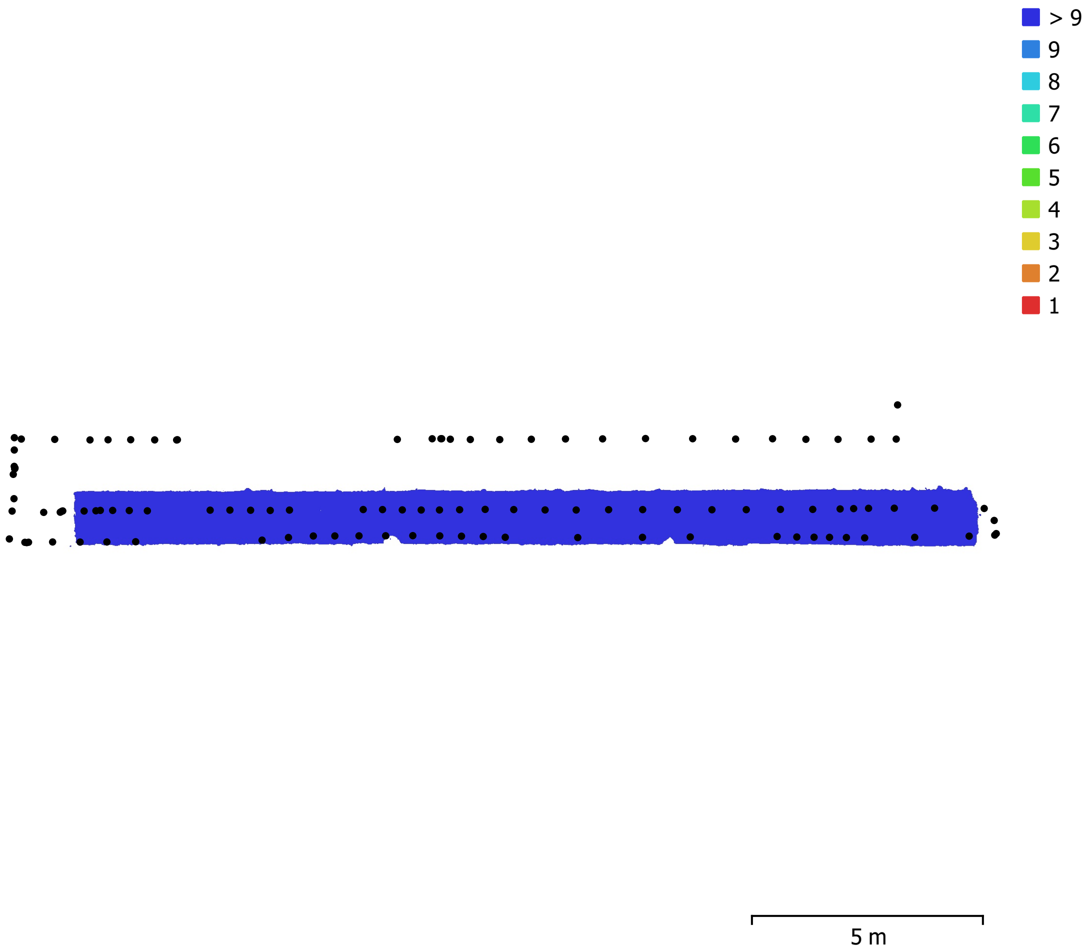

Fig. 1. Camera locations and image overlap.

Number of images:	108	Camera stations:	108
Flying altitude:	7.5 m	Tie points:	72,601
Ground resolution:	0.991 mm/pix	Projections:	485,990
Coverage area:	22.8 m²	Reprojection error:	0.968 pix

Camera Model	Resolution	Focal Length	Pixel Size	Precalibrated
ZenmuseP1 (35mm)	8192 x 5460	35 mm	4.39 x 4.39 μm	No

Table 1. Cameras.

Camera Calibration

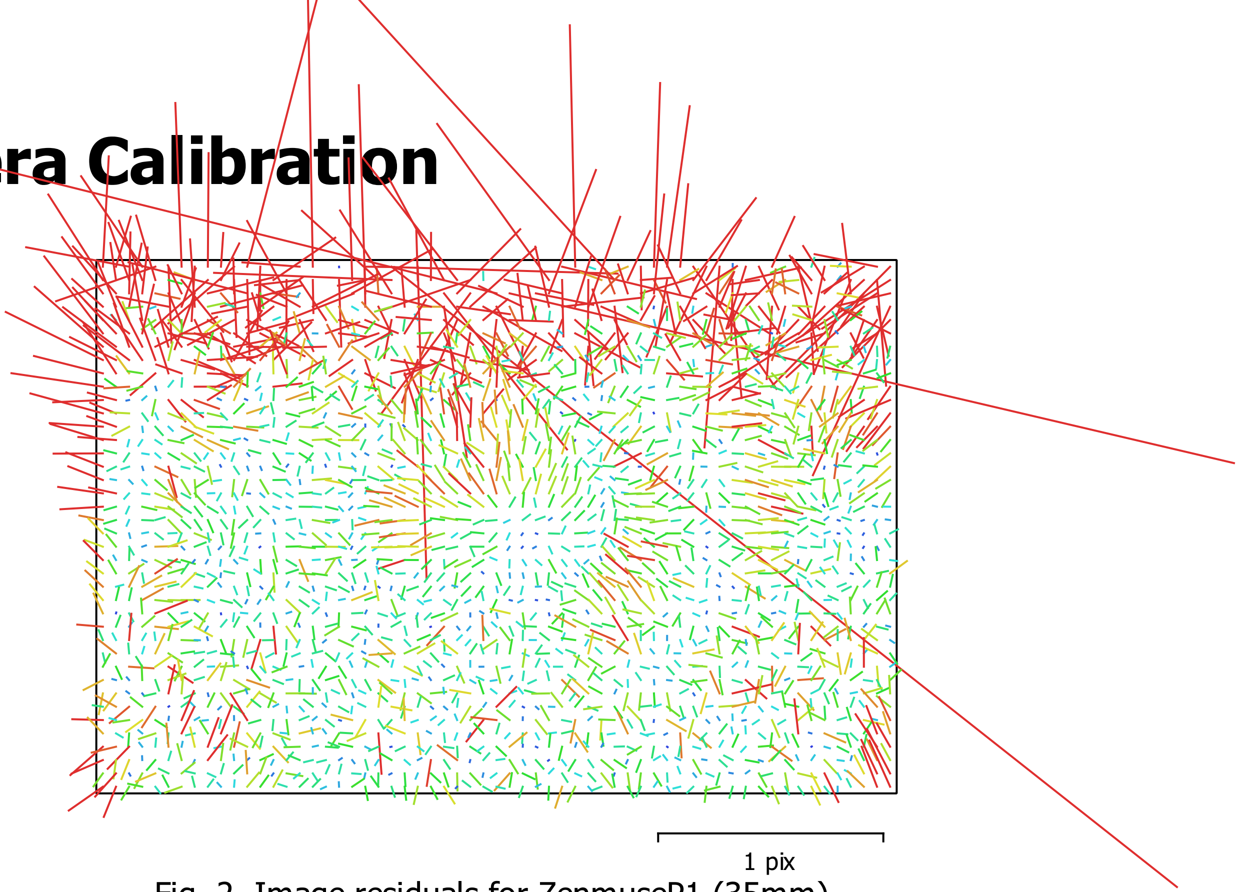

Fig. 2. Image residuals for ZenmuseP1 (35mm).

ZenmuseP1 (35mm)

108 images

Type	Resolution	Focal Length	Pixel Size
Frame	**8192 x 5460**	**35 mm**	**4.39 x 4.39 µm**

	Value	Error	F	Cx	Cy	K1	K2	K3	P1	P2
F	**8197.99**	0.078	1.00	-0.15	0.07	-0.03	0.06	-0.04	-0.13	0.12
Cx	**-28.5467**	0.1		1.00	0.01	-0.01	0.02	-0.02	0.90	-0.05
Cy	**19.3823**	0.05			1.00	-0.04	0.03	-0.04	-0.05	0.44
K1	**-0.0483598**	2.3e-05				1.00	-0.96	0.90	-0.02	-0.03
K2	**0.0174619**	0.00014					1.00	-0.98	0.02	0.02
K3	**-0.097522**	0.00027						1.00	-0.03	-0.03
P1	**-0.00101879**	2.6e-06							1.00	-0.06
P2	**0.000656727**	1.2e-06								1.00

Table 2. Calibration coefficients and correlation matrix.

Ground Control Points

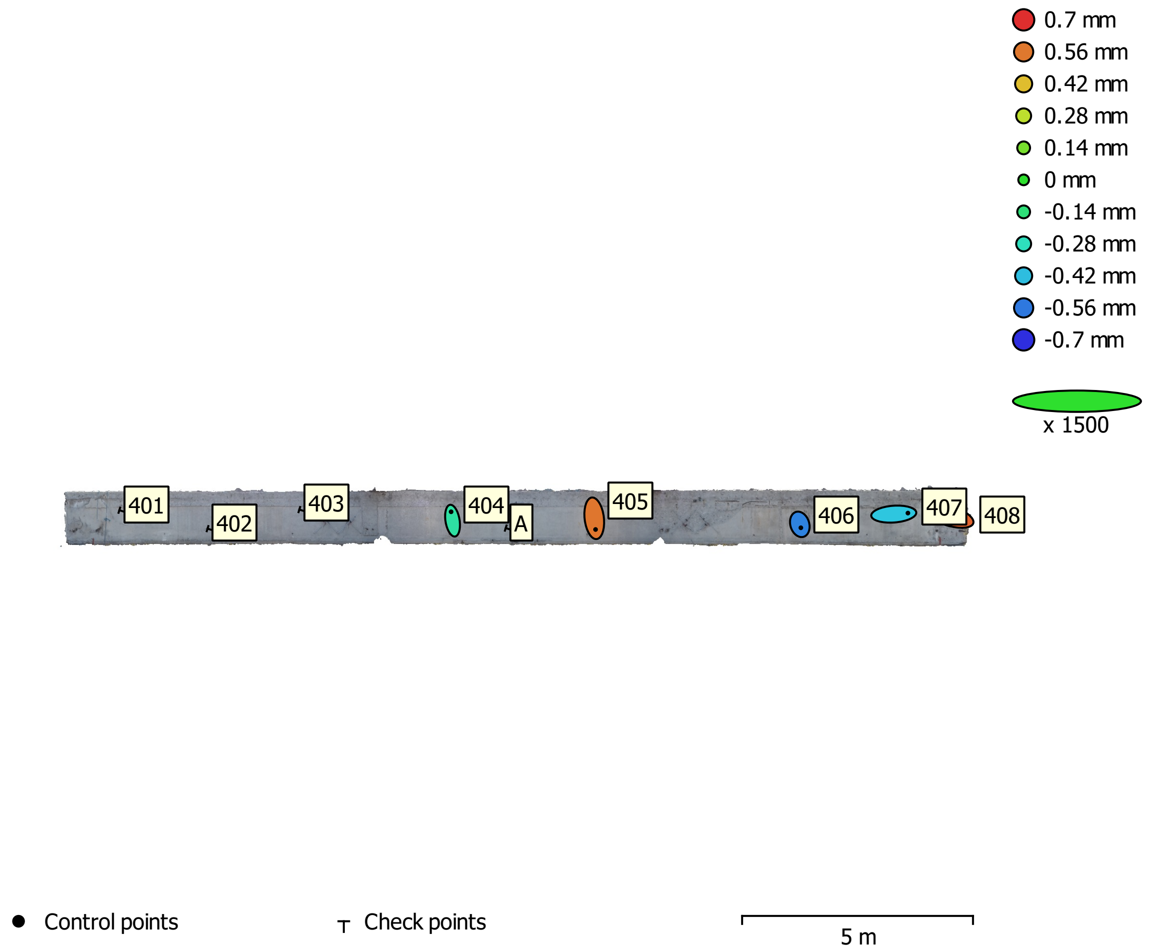

Fig. 3. GCP locations and error estimates.
Z error is represented by ellipse color. X,Y errors are represented by ellipse shape.
Estimated GCP locations are marked with a dot or crossing.

Count	X error (mm)	Y error (mm)	Z error (mm)	XY error (mm)	Total (mm)
5	0.268499	0.199449	0.486429	0.334472	0.590326

Table 3. Control points RMSE.

Label	X error (mm)	Y error (mm)	Z error (mm)	Total (mm)	Image (pix)
404	-0.0415819	0.256115	-0.225969	0.344073	0.472 (13)
405	0.0377634	-0.322988	0.564544	0.651504	0.336 (14)
406	0.0304882	-0.0984606	-0.538813	0.548583	0.355 (11)
407	0.408576	0.0296493	-0.401343	0.573489	0.245 (12)
408	-0.435246	0.135684	0.601581	0.754817	0.360 (12)
Total	**0.268499**	**0.199449**	**0.486429**	**0.590326**	**0.362**

Table 4. Control points.

Label	X error (mm)	Y error (mm)	Z error (mm)	Total (mm)	Image (pix)
A					0.318 (12)
401					0.179 (12)
402					0.224 (14)
403					0.198 (12)
Total					

Table 5. Check points.

Digital Elevation Model

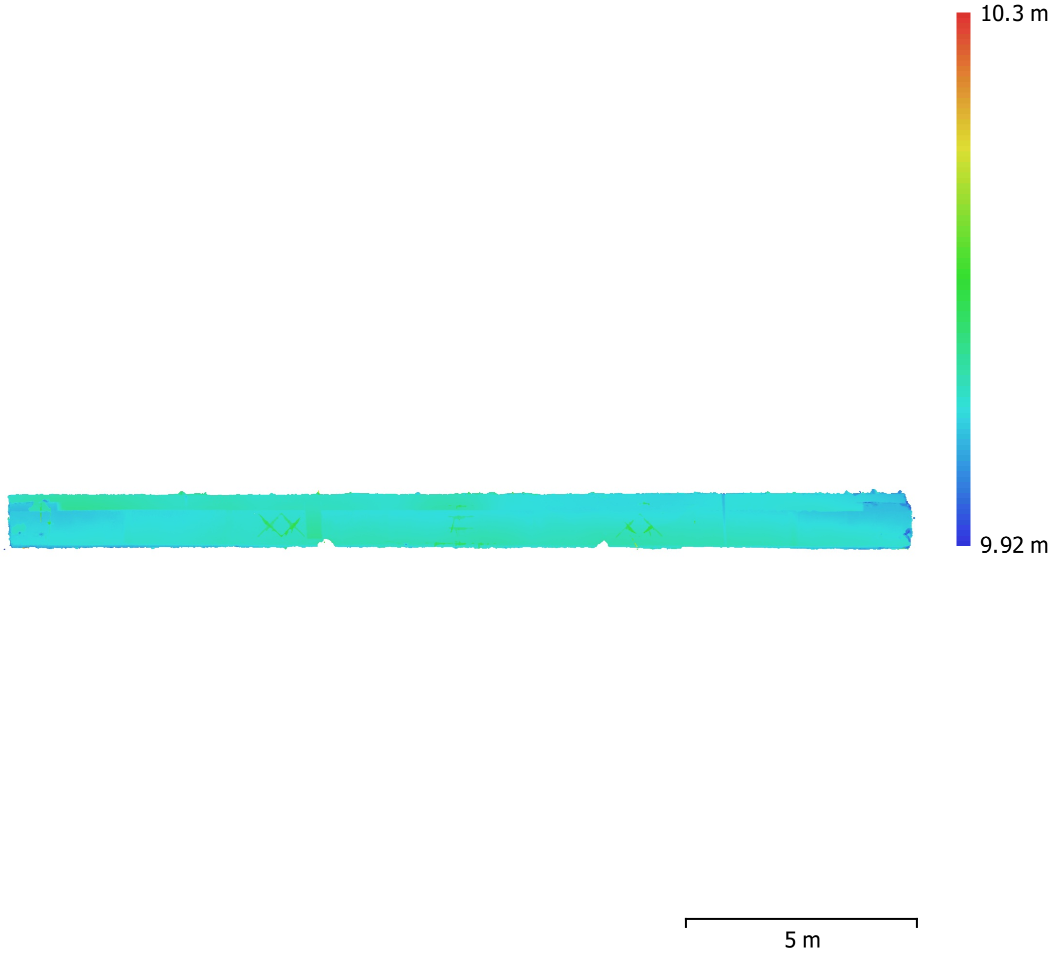

Fig. 4. Reconstructed digital elevation model.

Resolution:	1.98 mm/pix
Point density:	25.5 points/cm²

Processing Parameters

General	
Cameras	108
Aligned cameras	108
Markers	9
Shapes	
Polygon	6
Coordinate system	Local Coordinates (m)
Rotation angles	Yaw, Pitch, Roll
Point Cloud	
Points	72,601 of 182,572
RMS reprojection error	0.194014 (0.967643 pix)
Max reprojection error	0.594925 (66.6206 pix)
Mean key point size	3.73341 pix
Point colors	3 bands, uint8
Key points	2.89 GB
Average tie point multiplicity	6.24362
Alignment parameters	
Accuracy	High
Generic preselection	Yes
Reference preselection	Source
Key point limit	10,000
Key point limit per Mpx	40,000
Tie point limit	10,000
Exclude stationary tie points	Yes
Guided image matching	Yes
Adaptive camera model fitting	No
Matching time	45 minutes 37 seconds
Matching memory usage	3.13 GB
Alignment time	10 minutes 17 seconds
Alignment memory usage	407.81 MB
Date created	2023:03:14 17:56:36
Software version	1.8.4.14856
File size	23.94 MB
Depth Maps	
Count	19
Depth maps generation parameters	
Quality	High
Filtering mode	Mild
Max neighbors	16
Processing time	4 minutes 10 seconds
Memory usage	2.39 GB
Date created	2023:03:27 11:51:37
Software version	1.8.4.14856
File size	95.61 MB
Dense Point Cloud	
Points	26,268,053
Point colors	3 bands, uint8
Depth maps generation parameters	
Quality	High
Filtering mode	Mild

Max neighbors	16
Processing time	4 minutes 10 seconds
Memory usage	2.39 GB
Dense cloud generation parameters	
Processing time	2 minutes 24 seconds
Memory usage	2.82 GB
Date created	2023:03:27 11:54:02
Software version	1.8.4.14856
File size	530.03 MB
Model	
Faces	770,417
Vertices	387,208
Vertex colors	3 bands, uint8
Depth maps generation parameters	
Quality	High
Filtering mode	Mild
Max neighbors	16
Processing time	4 minutes 10 seconds
Memory usage	2.39 GB
Reconstruction parameters	
Surface type	Arbitrary
Source data	Dense cloud
Interpolation	Disabled
Strict volumetric masks	No
Processing time	1 minutes 54 seconds
Memory usage	1.75 GB
Date created	2023:03:27 12:06:43
Software version	1.8.4.14856
File size	17.66 MB
DEM	
Size	25,626 x 9,473
Coordinate system	Local Coordinates (m)
Reconstruction parameters	
Source data	Dense cloud
Interpolation	Disabled
Processing time	18 seconds
Memory usage	150.47 MB
Date created	2023:09:21 09:47:38
Software version	1.8.4.14856
File size	23.64 MB
Orthomosaic	
Size	19,720 x 1,329
Coordinate system	Local Coordinates (m)
Colors	3 bands, uint8
Reconstruction parameters	
Blending mode	Mosaic
Surface	Mesh
Enable hole filling	Yes
Enable ghosting filter	No
Processing time	1 minutes 28 seconds
Memory usage	1.43 GB
Date created	2023:09:21 10:39:26
Software version	1.8.4.14856
File size	579.82 MB
System	
Software name	Agisoft Metashape Professional

Software version	1.8.4 build 14856
OS	Windows 64 bit
RAM	31.89 GB
CPU	Intel(R) Core(TM) i7-4770 CPU @ 3.40GHz
GPU(s)	GeForce GTX 760
	GeForce GTX 760

Agisoft Metashape

Processing Report 5

21 September 2023

Survey Data

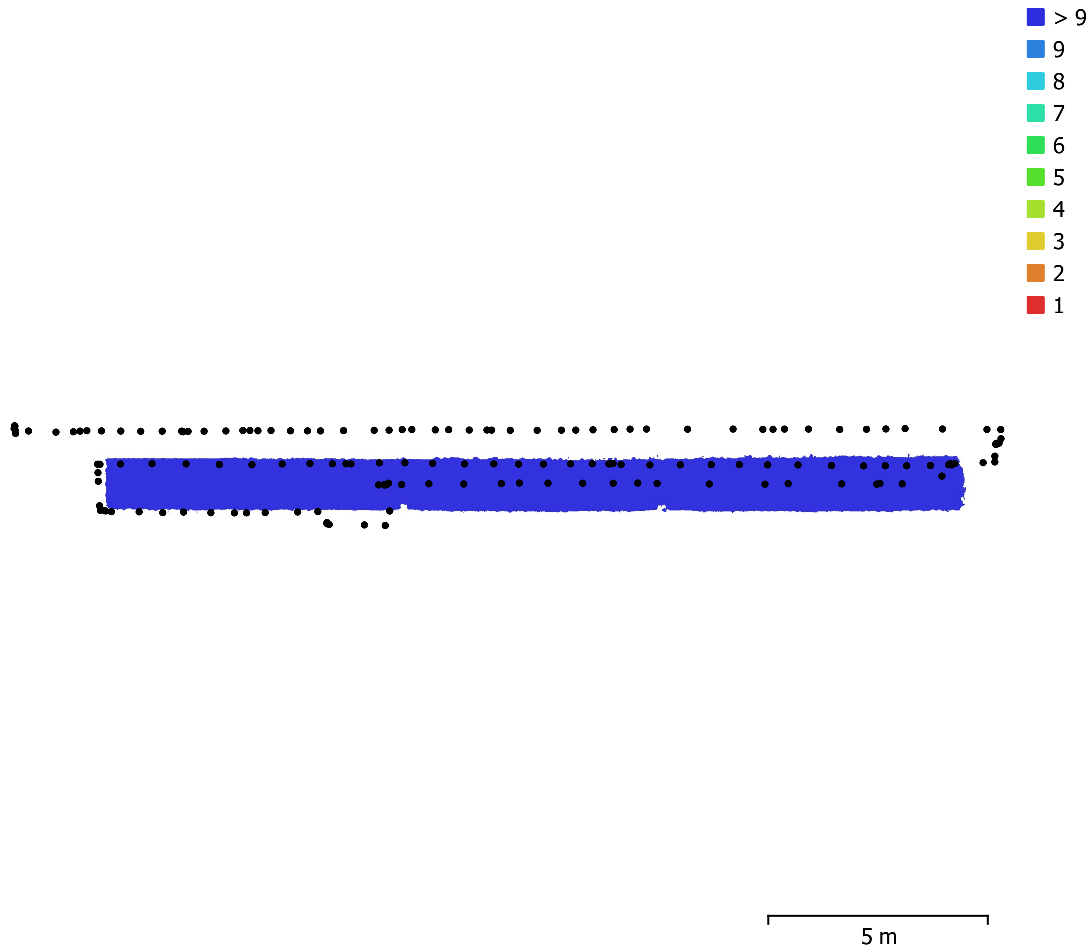

Fig. 1. Camera locations and image overlap.

Number of images:	155	Camera stations:	155
Flying altitude:	5.9 m	Tie points:	63,171
Ground resolution:	0.736 mm/pix	Projections:	655,828
Coverage area:	23.4 m²	Reprojection error:	0.984 pix

Camera Model	Resolution	Focal Length	Pixel Size	Precalibrated
ZenmuseP1 (35mm)	8192 x 5460	35 mm	4.39 x 4.39 μm	No

Table 1. Cameras.

Camera Calibration

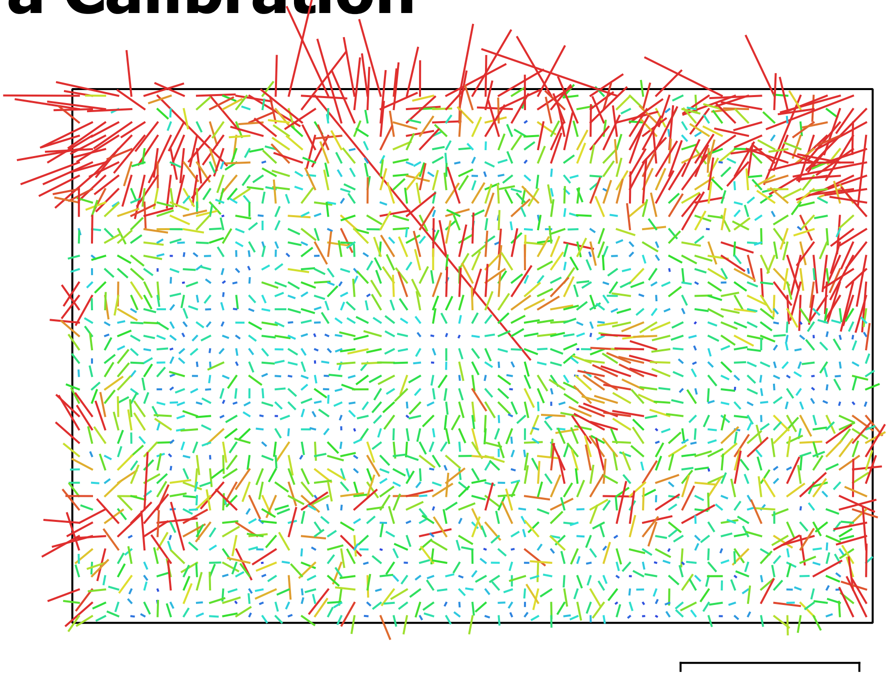

Fig. 2. Image residuals for ZenmuseP1 (35mm).

ZenmuseP1 (35mm)

155 images

Type	Resolution	Focal Length	Pixel Size
Frame	**8192 x 5460**	**35 mm**	**4.39 x 4.39 µm**

	Value	Error	F	Cx	Cy	K1	K2	K3	P1	P2
F	**8201.48**	0.12	1.00	-0.02	0.47	-0.05	0.02	-0.00	-0.03	0.01
Cx	**-19.925**	0.17		1.00	-0.04	-0.04	0.03	-0.04	0.73	-0.02
Cy	**19.8071**	0.078			1.00	0.00	0.00	-0.00	-0.03	0.31
K1	**-0.0480246**	2.7e-05				1.00	-0.96	0.90	-0.03	-0.01
K2	**0.0152438**	0.00017					1.00	-0.98	0.03	0.02
K3	**-0.0952236**	0.00033						1.00	-0.03	-0.02
P1	**-0.000918035**	3.6e-06							1.00	-0.02
P2	**0.000535109**	1.4e-06								1.00

Table 2. Calibration coefficients and correlation matrix.

Ground Control Points

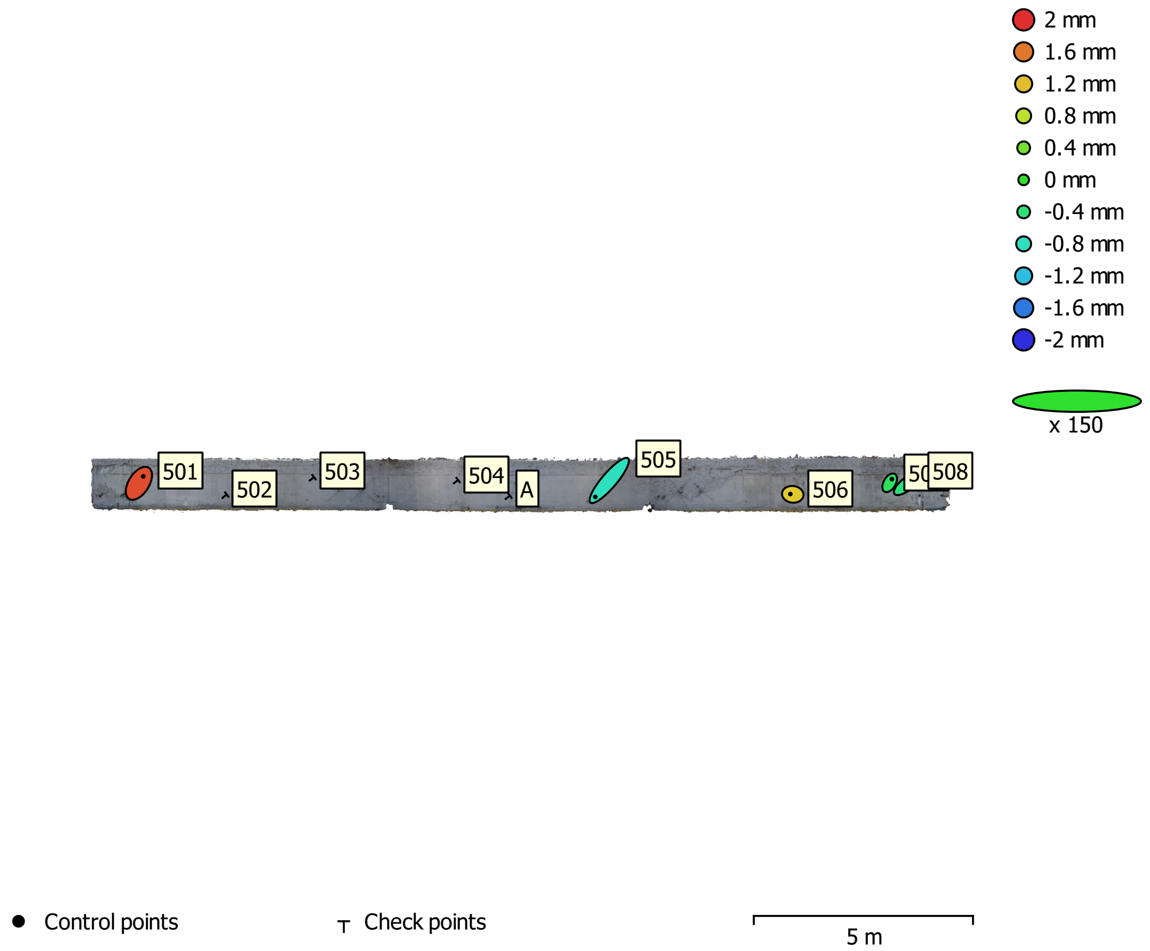

Fig. 3. GCP locations and error estimates.
Z error is represented by ellipse color. X,Y errors are represented by ellipse shape.
Estimated GCP locations are marked with a dot or crossing.

Count	X error (mm)	Y error (mm)	Z error (mm)	XY error (mm)	Total (mm)
5	2.34247	2.62749	1.05121	3.52007	3.67368

Table 3. Control points RMSE.

Label	**X error (mm)**	**Y error (mm)**	**Z error (mm)**	**Total (mm)**	**Image (pix)**
501	1.33616	2.10833	1.83686	3.0991	0.372 (18)
505	-4.25638	-4.9893	-0.803811	6.60727	0.683 (17)
506	-0.739375	0.0912814	1.12734	1.35126	0.334 (16)
507	0.663097	1.10833	-0.257024	1.31687	0.775 (17)
508	2.55878	1.98584	-0.409916	3.2648	0.508 (19)
Total	**2.34247**	**2.62749**	**1.05121**	**3.67368**	**0.560**

Table 4. Control points.

Label	**X error (mm)**	**Y error (mm)**	**Z error (mm)**	**Total (mm)**	**Image (pix)**
A					0.693 (13)
502					0.384 (13)
503					0.309 (15)
504					0.320 (15)
Total					

Table 5. Check points.

Digital Elevation Model

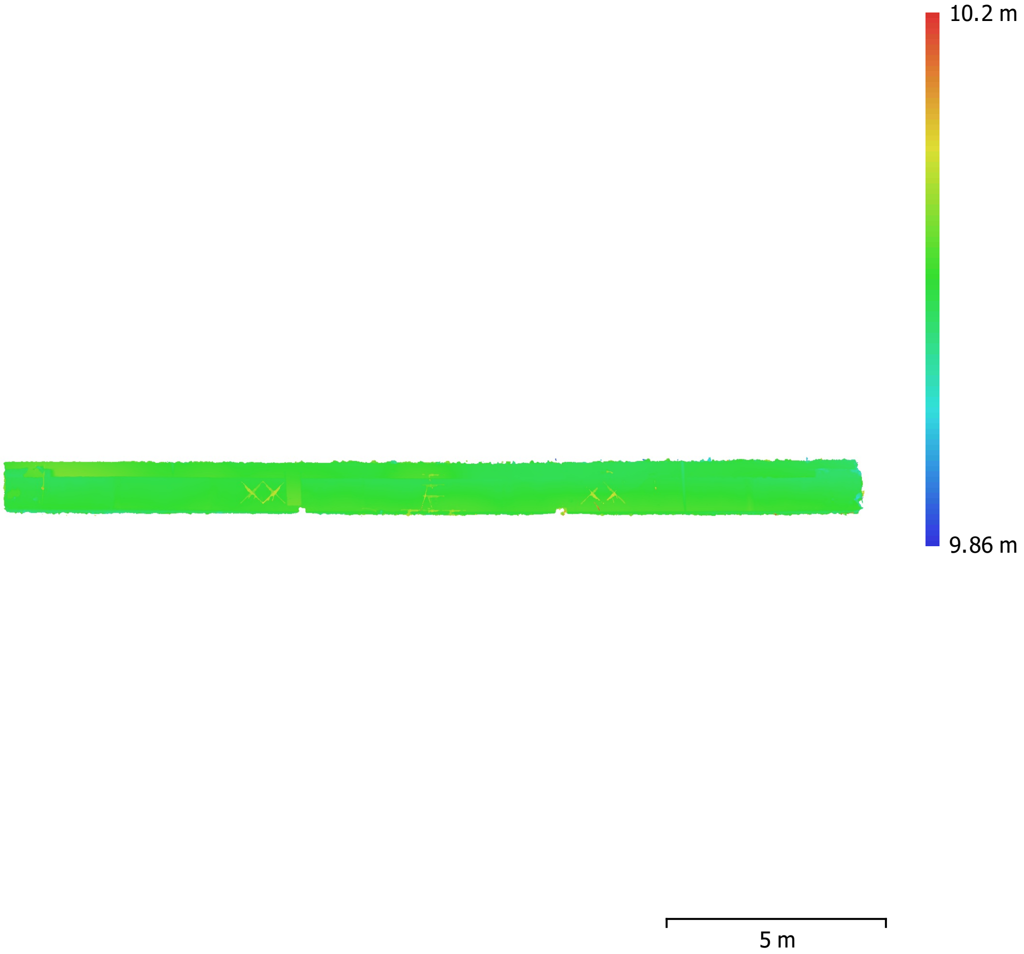

Fig. 4. Reconstructed digital elevation model.

Resolution:	1.47 mm/pix
Point density:	46.1 points/cm²

Processing Parameters

General	
Cameras	155
Aligned cameras	155
Markers	9
Shapes	
Polygon	10
Coordinate system	Local Coordinates (m)
Rotation angles	Yaw, Pitch, Roll
Point Cloud	
Points	63,171 of 205,018
RMS reprojection error	0.208073 (0.984345 pix)
Max reprojection error	0.634711 (54.8703 pix)
Mean key point size	4.0934 pix
Point colors	3 bands, uint8
Key points	2.96 GB
Average tie point multiplicity	8.11402
Alignment parameters	
Accuracy	High
Generic preselection	Yes
Reference preselection	Source
Key point limit	10,000
Key point limit per Mpx	40,000
Tie point limit	10,000
Exclude stationary tie points	Yes
Guided image matching	Yes
Adaptive camera model fitting	No
Matching time	52 minutes 2 seconds
Matching memory usage	2.53 GB
Alignment time	7 minutes 54 seconds
Alignment memory usage	474.97 MB
Date created	2023:03:15 10:08:56
Software version	1.8.4.14856
File size	33.79 MB
Depth Maps	
Count	155
Depth maps generation parameters	
Quality	High
Filtering mode	Mild
Max neighbors	16
Processing time	59 minutes 59 seconds
Memory usage	4.55 GB
Date created	2023:03:30 09:07:48
Software version	1.8.4.14856
File size	616.14 MB
Dense Point Cloud	
Points	23,329,225
Point colors	3 bands, uint8
Depth maps generation parameters	
Quality	High
Filtering mode	Mild

Max neighbors	16
Processing time	59 minutes 59 seconds
Memory usage	4.55 GB
Dense cloud generation parameters	
Processing time	54 minutes 43 seconds
Memory usage	18.23 GB
Date created	2023:03:30 10:02:32
Software version	1.8.4.14856
File size	890.54 MB
Model	
Faces	999,616
Vertices	503,105
Vertex colors	3 bands, uint8
Depth maps generation parameters	
Quality	High
Filtering mode	Mild
Max neighbors	16
Processing time	59 minutes 59 seconds
Memory usage	4.55 GB
Reconstruction parameters	
Surface type	Arbitrary
Source data	Dense cloud
Interpolation	Disabled
Strict volumetric masks	No
Processing time	6 minutes 39 seconds
Memory usage	3.37 GB
Date created	2023:03:30 13:22:51
Software version	1.8.4.14856
File size	22.93 MB
DEM	
Size	31,619 x 13,528
Coordinate system	Local Coordinates (m)
Reconstruction parameters	
Source data	Dense cloud
Interpolation	Disabled
Processing time	19 seconds
Memory usage	151.12 MB
Date created	2023:09:21 11:04:39
Software version	1.8.4.14856
File size	37.61 MB
Orthomosaic	
Size	19,626 x 1,349
Coordinate system	Local Coordinates (m)
Colors	3 bands, uint8
Reconstruction parameters	
Blending mode	Disabled
Surface	Mesh
Enable hole filling	Yes
Enable ghosting filter	No
Processing time	2 minutes 7 seconds
Memory usage	1.39 GB
Date created	2023:09:21 11:12:39
Software version	1.8.4.14856
File size	718.92 MB
System	
Software name	Agisoft Metashape Professional

Software version	1.8.4 build 14856
OS	Windows 64 bit
RAM	31.89 GB
CPU	Intel(R) Core(TM) i7-4770 CPU @ 3.40GHz
GPU(s)	GeForce GTX 760
	GeForce GTX 760

Agisoft Metashape

Processing Report 6

21 September 2023

Survey Data

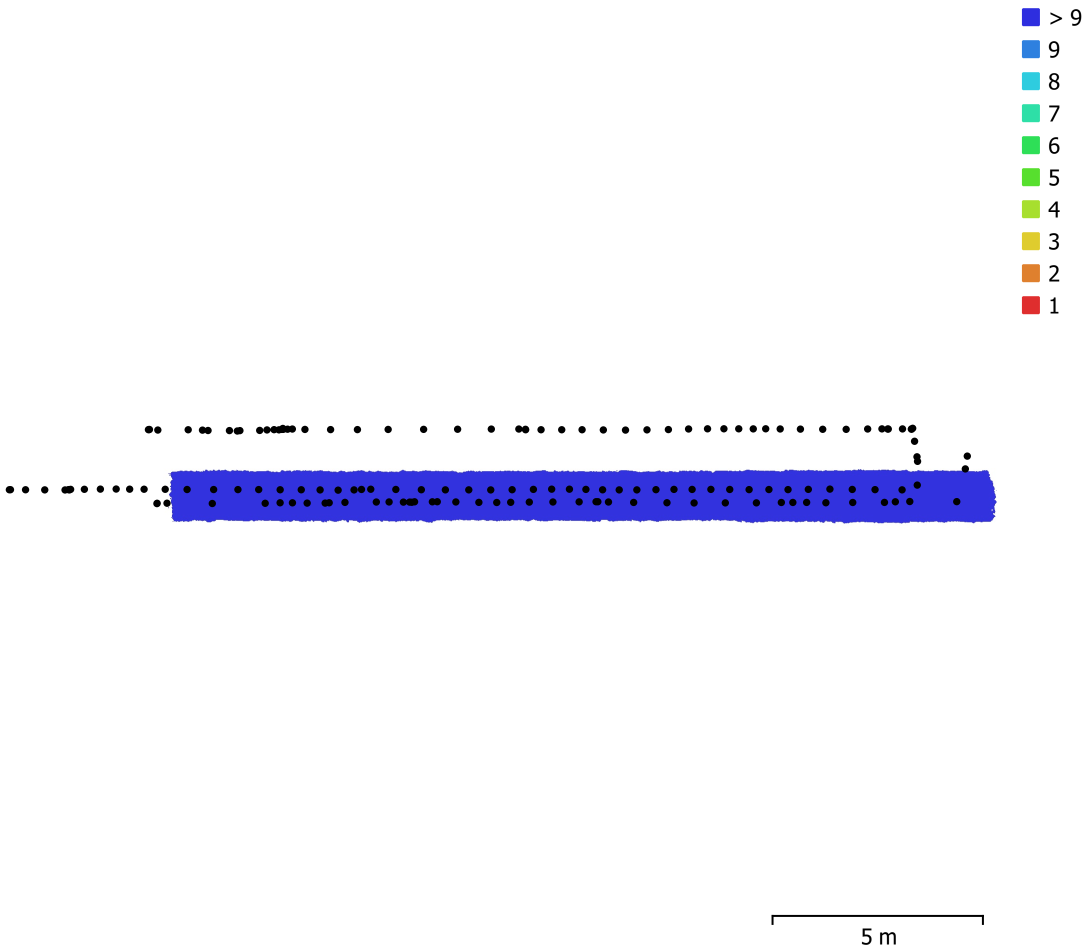

Fig. 1. Camera locations and image overlap.

Number of images:	156	Camera stations:	156
Flying altitude:	6.05 m	Tie points:	84,338
Ground resolution:	0.758 mm/pix	Projections:	698,892
Coverage area:	23.3 m²	Reprojection error:	1.06 pix

Camera Model	Resolution	Focal Length	Pixel Size	Precalibrated
ZenmuseP1 (35mm)	8192 x 5460	35 mm	4.39 x 4.39 μm	No

Table 1. Cameras.

Camera Calibration

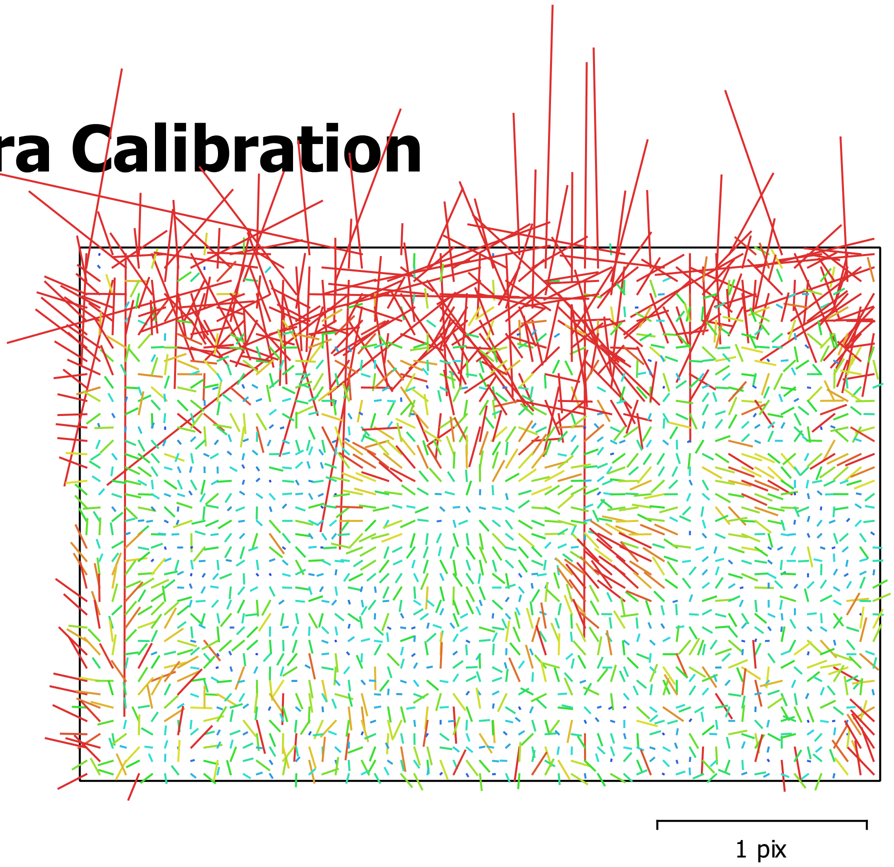

Fig. 2. Image residuals for ZenmuseP1 (35mm).

ZenmuseP1 (35mm)

156 images

Type	Resolution	Focal Length	Pixel Size
Frame	**8192 x 5460**	**35 mm**	**4.39 x 4.39 µm**

	Value	Error	F	Cx	Cy	K1	K2	K3	P1	P2
F	**8195.97**	0.1	1.00	0.00	0.19	-0.03	0.03	-0.02	0.04	0.07
Cx	**-29.6934**	0.16		1.00	-0.04	-0.04	0.02	-0.01	0.84	0.01
Cy	**17.8622**	0.078			1.00	-0.02	0.02	-0.02	0.03	0.41
K1	**-0.0479015**	2.9e-05				1.00	-0.96	0.90	-0.03	-0.01
K2	**0.014307**	0.00018					1.00	-0.98	0.02	0.01
K3	**-0.0938101**	0.00035						1.00	-0.02	-0.01
P1	**-0.00116876**	3.8e-06							1.00	0.01
P2	**0.000627223**	1.5e-06								1.00

Table 2. Calibration coefficients and correlation matrix.

Ground Control Points

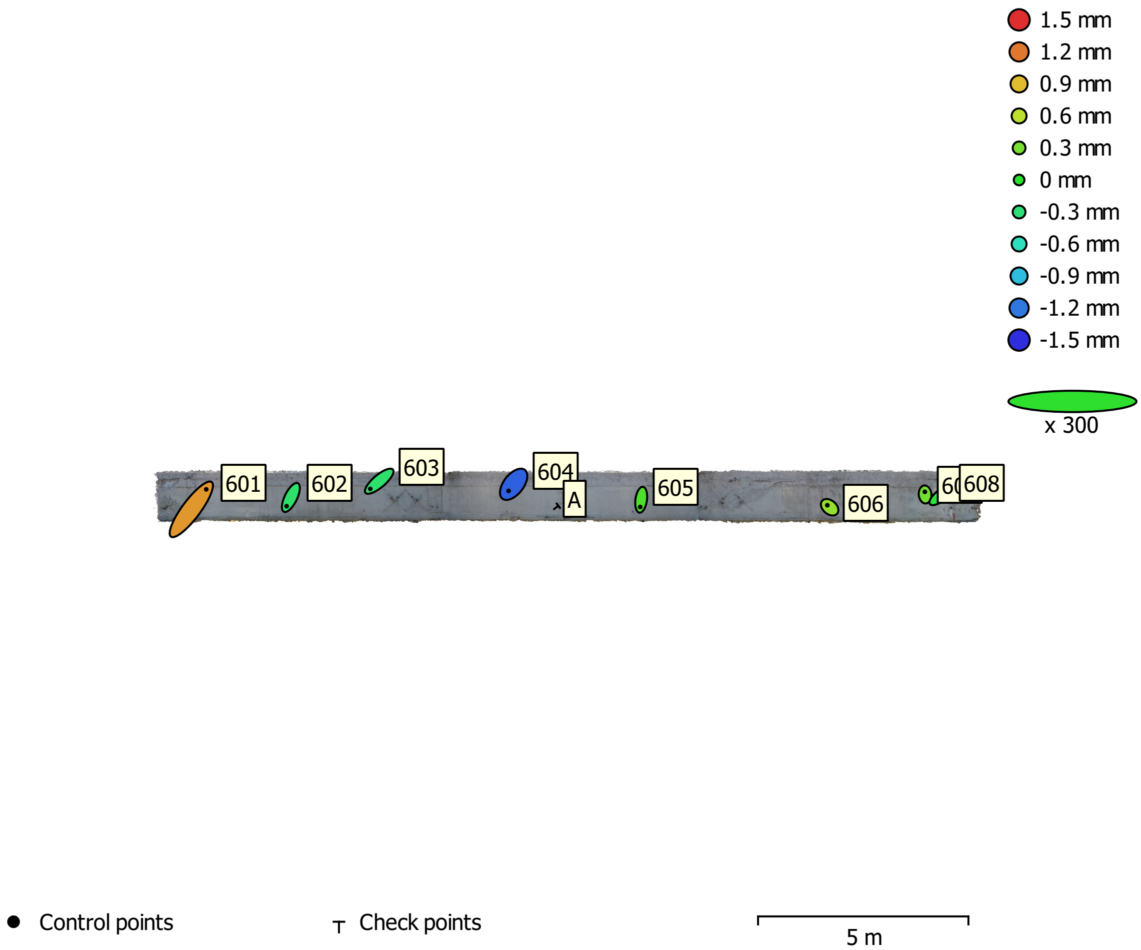

Fig. 3. GCP locations and error estimates.
Z error is represented by ellipse color. X,Y errors are represented by ellipse shape.
Estimated GCP locations are marked with a dot or crossing.

Count	X error (mm)	Y error (mm)	Z error (mm)	XY error (mm)	Total (mm)
8	1.12388	1.44706	0.635058	1.83223	1.93917

Table 3. Control points RMSE.

Label	X error (mm)	Y error (mm)	Z error (mm)	Total (mm)	Image (pix)
601	2.36562	3.16332	1.06281	4.09051	0.353 (12)
602	-0.67959	-1.37701	-0.248668	1.55558	0.598 (12)
603	-1.42002	-1.20553	-0.249486	1.87936	0.626 (13)
604	-0.804887	-1.03554	-1.30188	1.84799	0.770 (10)
605	-0.156008	-1.14328	0.12301	1.16042	0.412 (12)
606	-0.370354	0.315815	0.4191	0.642298	0.530 (12)
607	-0.0390867	0.423734	0.282034	0.510511	0.315 (12)
608	1.10432	0.8585	-0.0869201	1.40146	0.464 (12)
Total	**1.12388**	**1.44706**	**0.635058**	**1.93917**	**0.523**

Table 4. Control points.

Label	X error (mm)	Y error (mm)	Z error (mm)	Total (mm)	Image (pix)
A					0.466 (13)
Total					

Table 5. Check points.

Digital Elevation Model

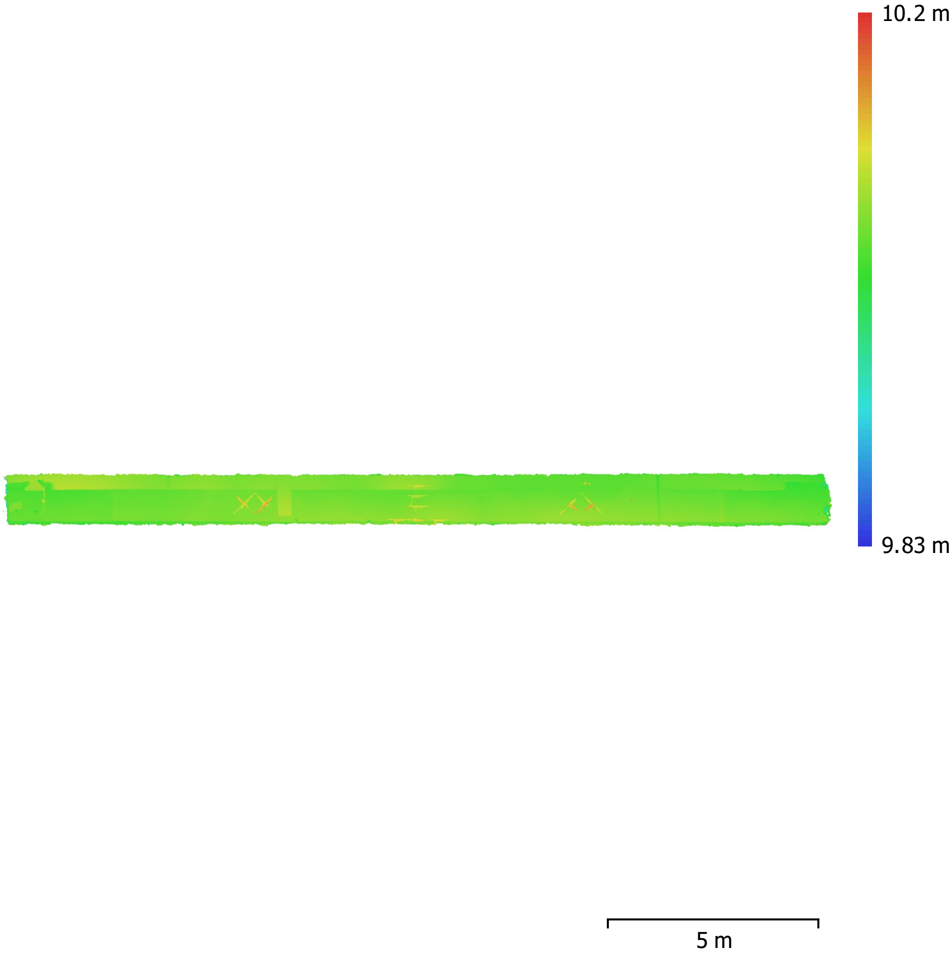

Fig. 4. Reconstructed digital elevation model.

Resolution:	1.52 mm/pix
Point density:	43.6 points/cm²

Processing Parameters

General	
Cameras	156
Aligned cameras	156
Markers	9
Shapes	
Polygon	6
Coordinate system	Local Coordinates (m)
Rotation angles	Yaw, Pitch, Roll
Point Cloud	
Points	84,338 of 246,502
RMS reprojection error	0.21111 (1.06342 pix)
Max reprojection error	0.648232 (50.7798 pix)
Mean key point size	4.11504 pix
Point colors	3 bands, uint8
Key points	2.62 GB
Average tie point multiplicity	6.78627
Alignment parameters	
Accuracy	High
Generic preselection	Yes
Reference preselection	Source
Key point limit	10,000
Key point limit per Mpx	40,000
Tie point limit	10,000
Exclude stationary tie points	Yes
Guided image matching	Yes
Adaptive camera model fitting	No
Matching time	35 minutes 25 seconds
Matching memory usage	2.61 GB
Alignment time	17 minutes 53 seconds
Alignment memory usage	287.94 MB
Date created	2023:03:15 12:14:53
Software version	1.8.4.14856
File size	34.57 MB
Depth Maps	
Count	156
Depth maps generation parameters	
Quality	High
Filtering mode	Mild
Max neighbors	16
Processing time	2 hours 22 minutes
Memory usage	3.88 GB
Date created	2023:03:24 19:16:20
Software version	1.8.4.14856
File size	563.61 MB
Dense Point Cloud	
Points	33,688,270
Point colors	3 bands, uint8
Depth maps generation parameters	
Quality	High
Filtering mode	Mild

Max neighbors	16
Processing time	2 hours 22 minutes
Memory usage	3.88 GB
Dense cloud generation parameters	
Processing time	1 hours 38 minutes
Memory usage	18.33 GB
Date created	2023:03:24 20:54:48
Software version	1.8.4.14856
File size	1008.89 MB
Model	
Faces	871,871
Vertices	438,669
Vertex colors	3 bands, uint8
Depth maps generation parameters	
Quality	High
Filtering mode	Mild
Max neighbors	16
Processing time	2 hours 22 minutes
Memory usage	3.88 GB
Reconstruction parameters	
Surface type	Arbitrary
Source data	Dense cloud
Interpolation	Disabled
Strict volumetric masks	No
Processing time	3 minutes 59 seconds
Memory usage	3.23 GB
Date created	2023:03:27 10:02:16
Software version	1.8.4.14856
File size	20.00 MB
DEM	
Size	32,785 x 11,318
Coordinate system	Local Coordinates (m)
Reconstruction parameters	
Source data	Dense cloud
Interpolation	Disabled
Processing time	17 seconds
Memory usage	151.17 MB
Date created	2023:03:30 13:45:05
Software version	1.8.4.14856
File size	33.49 MB
Orthomosaic	
Size	19,677 x 1,288
Coordinate system	Local Coordinates (m)
Colors	3 bands, uint8
Reconstruction parameters	
Blending mode	Disabled
Surface	Mesh
Enable hole filling	Yes
Enable ghosting filter	No
Processing time	2 minutes 0 seconds
Memory usage	1.38 GB
Date created	2023:03:30 13:46:53
Software version	1.8.4.14856
File size	742.78 MB
System	
Software name	Agisoft Metashape Professional

Software version	1.8.4 build 14856
OS	Windows 64 bit
RAM	31.89 GB
CPU	Intel(R) Core(TM) i7-4770 CPU @ 3.40GHz
GPU(s)	GeForce GTX 760
	GeForce GTX 760